

ERCOFTAC

*Bulletin*

September 2016

108

# European Research Community on Flow, Turbulence and Combustion

ERCOFTAC is a leading European association of research, education and industry groups in the technology of flow, turbulence and combustion. The main objectives of ERCOFTAC are: To promote joint efforts of European research institutes and industries with the aim of **exchanging technical and scientific information**; to promote **Pilot Centres** for collaboration, stimulation and application of

research across Europe; to stimulate, through the creation of **Special Interest Groups**, wellcoordinated European-wide research efforts on specific topics; to stimulate the creation of advanced training activities; and to be influential on funding agencies, governments, the European Commission and the European Parliament.

[www.ercoftac.org](http://www.ercoftac.org)

## Honorary Presidents

Mathieu, J. Spalding, D.B.

## Executive Committee

### Chairman

Tomboulides, A.  
Aristotle University of  
Thessaloniki, Greece  
Tel: +30 2310 996068  
ananiast@auth.gr

### First Deputy Chairman

Von Terzi, D.

### Second Deputy Chairman

\_\_\_\_\_

### Treasurer

Hirsch, C.

### SPC Chairman

Hickel, S.

### SPC Deputy Chairman

Geurts, B.

### KNC Chairman

Standingford, D.

### KNC Deputy Chairman

Von Terzi, D.

### Industrial Eng. Officer

Seoud, R.E.

### Knowledge Base Editor

Rodi, W.

### Bulletin Editor

Elsner, W.

## ERCOFTAC Seat of the Organisation

### Director

Hirsch, C.  
Chaussée de la Hulpe 189  
Terhulpesteenweg  
B-1170 Brussels, Belgium  
Tel: +32 2 643 3572  
Fax: +32 2 647 9398  
ado@ercoftac.be

## Scientific Programme Committee

### Chairman

Hickel, S.  
Delft University of Technology  
Faculty of Aerospace Engineering  
Kluyverweg 1  
2629 HS Delft  
The Netherlands  
Tel: +31 152 789 570  
S.Hickel@tudelft.nl

### Deputy Chairman

Geurts, B.

## Knowledge Network Committee

### Chairman

Standingford, D.  
Zenotech Ltd.  
1 Laarkfield Grove  
Chepstow, NP16 5UF  
United Kingdom  
Tel: +44 7870 628 916  
david.standingford@zenotech.com

### Deputy Chairman

Von Terzi, D.

### Industrial Eng. Officer

Seoud, R.E.  
richard.seoud-ieo@ercoftac.org

## ERCOFTAC Central Administration and Development Office (CADO)

### Admin. Manager

Jakubczak, M.  
PO Box 53877  
London, SE27 7BR  
United Kingdom  
Tel: +44 203 602 8984  
admin@cado-ercoftac.org  
Skype: Ercoftaccado

**TABLE OF CONTENTS**

<b>Introduction Fluid Science and Engineering at ETMM11</b>	<b>3</b>
<b>Tripping Effects in Low-Reynolds Number Turbulent Boundary Layers</b> <i>R. Örlü, C. Sanmiguel Vila, R. Vinuesa, S. Discetti, A. Ianiro and P. Schlatter</i>	<b>5</b>
<b>Influence of a Large-Eddy-Breakup-Device on the Turbulent Interface of Boundary Layers</b> <i>C. Chin, N. Hutchins, A. Ooi, R. Örlü, P. Schlatter and J. P. Monty</i>	<b>10</b>
<b>History Effects and Near-Equilibrium in Turbulent Boundary Layers with Pressure Gradient</b> <i>P. Schlatter, R. Vinuesa, A. Bobke and R. Örlü</i>	<b>14</b>
<b>Investigation of Turbulent Boundary Layers Approaching Separation</b> <i>A. Drózdź and W. Elsner</i>	<b>20</b>
<b>Assessment of Turbulent Boundary Layers on a NACA4412 Wing Section at Moderate Re</b> <i>R. Vinuesa, S. M. Hosseini, A. Hanifi, D. S. Henningson and P. Schlatter</i>	<b>25</b>
<b>Revisiting Hot-Wire Anemometry Close to Solid Walls</b> <i>Y. Ikeya, R. Örlü, K. Fukagata and P. H. Alfredsson</i>	<b>30</b>
<b>Further Assessment of the Grey-Area Enhanced -DES Approach for Complex Flows</b> <i>M. Fuchs, C. Mockett, J. Sesterhenn and F. Thiele</i>	<b>36</b>
<b>An Investigation of Transition Prediction Using Improved KDO RANS Model</b> <i>J.L. Xu, D. Xu, Y. Zhang and J.Q. Bai</i>	<b>42</b>
<b>Prediction of Bypass and Separation-Induced Transition With an Algebraic Intermittency Model</b> <i>S. Kubacki, T. Borzecki, E. Dick</i>	<b>48</b>
<b>Skin Friction Reduction in Fully Developed Turbulent Channel Flow Based on DNS and Adjoint Shape Optimization</b> <i>T. Köthe and C. Wagner</i>	<b>54</b>
<b>A Comparative Study of DES Type Methods for Mild Flow Separation Prediction on a NACA0015 Airfoil</b> <i>L. Wang, L. Li and S. Fu</i>	<b>59</b>

**EDITOR** Marek, M.  
**TECHNICAL EDITOR** Kuban, Ł.  
**CHAIRMAN** Elsner, W.  
**EDITORIAL BOARD** Armenio, V.  
 Dick, E.  
 Geurts, B.J.  
**DESIGN & LAYOUT** Borhani, N.  
 Nichita, B.A.  
**COVER DESIGN** Aniszewski, W.

**SUBMISSIONS**

ERCOFTAC Bulletin  
 Institute of Thermal Machinery  
 Częstochowa University of Technology  
 Al. Armii Krajowej 21  
 42-201 Częstochowa  
 Poland  
 Tel: +48 343 250 507  
 Fax: +48 343 250 507  
 Email: [ercoftac@imc.pcz.czest.pl](mailto:ercoftac@imc.pcz.czest.pl)

**HOSTED, PRINTED & DISTRIBUTED BY**



**CZĘSTOCHOWA UNIVERSITY OF TECHNOLOGY**

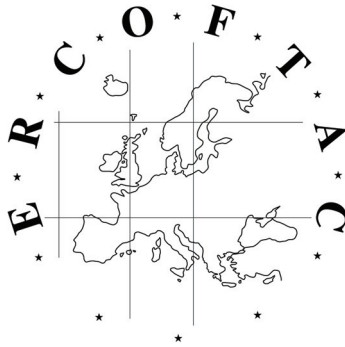
ISSN: 2518-0991

The reader should note that the Editorial Board cannot accept responsibility for the accuracy of statements made by any contributing authors

**NEXT ERCOFTAC EVENTS**

*ERCOFTAC Spring Festival*  
 6<sup>th</sup> April, 2017  
 Vienna, Austria

*ERCOFTAC Committee Meetings*  
 6<sup>th</sup> April, 2017, 2016  
 Vienna, Austria



# The ERCOFTAC Best Practice Guidelines for Industrial Computational Fluid Dynamics

The Best Practice Guidelines (BPG) were commissioned by ERCOFTAC following an extensive consultation with European industry which revealed an urgent demand for such a document. The first edition was completed in January 2000 and constitutes generic advice on how to carry out quality CFD calculations. The BPG therefore address mesh design; construction of numerical boundary conditions where problem data is uncertain; mesh and model sensitivity checks; distinction between numerical and turbulence model inadequacy; preliminary information regarding the limitations of turbulence models etc. The aim is to encourage a common best practice by virtue of which separate analyses of the same problem, using the same model physics, should produce consistent results. Input and advice was sought from a wide cross-section of CFD specialists, eminent academics, end-users and, (particularly important) the leading commercial code vendors established in Europe. Thus, the final document can be considered to represent the consensus view of the European CFD community.

Inevitably, the Guidelines cannot cover every aspect of CFD in detail. They are intended to offer roughly those 20% of the most important general rules of advice that cover roughly 80% of the problems likely to be encountered. As such, they constitute essential information for the novice user and provide a basis for quality management and regulation of safety submissions which rely on CFD. Experience has also shown that they can often provide useful advice for the more experienced user. The technical content is limited to single-phase, compressible and incompressible, steady and unsteady, turbulent and laminar flow with and without heat transfer. Versions which are customised to other aspects of CFD (the remaining 20% of problems) are planned for the future.

The seven principle chapters of the document address numerical, convergence and round-off errors; turbulence modelling; application uncertainties; user errors; code errors; validation and sensitivity tests for CFD models and finally examples of the BPG applied in practice. In the first six of these, each of the different sources of error and uncertainty are examined and discussed, including references to important books, articles and reviews. Following the discussion sections, short simple bullet-point statements of advice are listed which provide clear guidance and are easily understandable without elaborate mathematics. As an illustrative example, an extract dealing with the use of turbulent wall functions is given below:

- Check that the correct form of the wall function is being used to take into account the wall roughness. An equivalent roughness height and a modified multiplier in the law of the wall must be used.
- Check the upper limit on  $y^+$ . In the case of moderate Reynolds number, where the boundary layer only extends to  $y^+$  of 300 to 500, there is no chance of accurately resolving the boundary layer if the first integration point is placed at a location with the value of  $y^+$  of 100.

- Check the lower limit of  $y^+$ . In the commonly used applications of wall functions, the meshing should be arranged so that the values of  $y^+$  at all the wall-adjacent integration points is only slightly above the recommended lower limit given by the code developers, typically between 20 and 30 (the form usually assumed for the wall functions is not valid much below these values). This procedure offers the best chances to resolve the turbulent portion of the boundary layer. It should be noted that this criterion is impossible to satisfy close to separation or reattachment zones unless  $y^+$  is based upon  $y^*$ .
- Exercise care when calculating the flow using different schemes or different codes with wall functions on the same mesh. Cell centred schemes have their integration points at different locations in a mesh cell than cell vertex schemes. Thus the  $y^+$  value associated with a wall-adjacent cell differs according to which scheme is being used on the mesh.
- Check the resolution of the boundary layer. If boundary layer effects are important, it is recommended that the resolution of the boundary layer is checked after the computation. This can be achieved by a plot of the ratio between the turbulent to the molecular viscosity, which is high inside the boundary layer. Adequate boundary layer resolution requires at least 8-10 points in the layer.

All such statements of advice are gathered together at the end of the document to provide a 'Best Practice Checklist'. The examples chapter provides detailed expositions of eight test cases each one calculated by a code vendor (viz FLUENT, AEA Technology, Computational Dynamics, NUMECA) or code developer (viz Electricité de France, CEA, British Energy) and each of which highlights one or more specific points of advice arising in the BPG. These test cases range from natural convection in a cavity through to flow in a low speed centrifugal compressor and in an internal combustion engine valve.

Copies of the Best Practice Guidelines can be acquired from:

ERCOFTAC (CADO)  
PO Box 53877  
London, SE27 7BR  
United Kingdom  
Tel: +44 203 602 8984  
Email: [magdalena.jakubczak@ercoftac.org](mailto:magdalena.jakubczak@ercoftac.org)

The price per copy (not including postage) is:

ERCOFTAC members		
First copy		<i>Free</i>
Subsequent copies		75 Euros
Students		75 Euros
Non-ERCOFTAC academics		
Non-ERCOFTAC industrial		140 Euros
EU/Non EU postage fee		230 Euros
		10/17 Euros

# INTRODUCTION

## FLUID SCIENCE AND ENGINEERING AT ETMM11

Palermo, 2016

September 21-23, 2016 the 11<sup>th</sup> ERCOFTAC Symposium on Engineering Turbulence Modeling and Measurement (ETMM11) took place in Palermo, hosted by the University of Palermo. ETMM11 brought together over 200 participants, providing a platform for the discussion of recent developments in Fluid Science and Engineering. Strong classical ETMM11 themes included

- Combustion and Flames,
- Wall-bounded flows,
- Experimental methods and studies, and

Recent developments in high-fidelity computational methods, ranging from extreme DNS through novel LES models and RaNS applications were discussed at length. In addition, challenges in multiphase turbulence and heat transfer were given a podium.

The ETMM series of conferences underlines the vitality of ERCOFTAC, giving prominence to research on scientific and application-oriented aspects of turbulence and its computational and experimental characterization. This directly helps to promote turbulence investigations and the exploitation of models, codes and knowledge. ETMM as a flagship conference closely expresses ERCOFTAC's ambitions as a research community promoting Science, Engineering and their mutual cross-fertilization.

### Keynote lectures setting the stage

The background of the program was provided by six keynote lectures by prominent colleagues in the field. In these presentations leading-edge research activities were reviewed as well as recent breakthroughs discussed. Issues dealing with turbulent flow over synthetic and naturally rough walls were discussed from an engineering perspective by Karen Flack (United States Naval Academy) and from a hydraulics perspective by Vladimir Nikora (University of Aberdeen). The use of systematic experiments was highlighted to relate details of the surface topography to frictional drag as well as to implications for sediment transport and consequences for vegetation. A subject at the heart of ETMM and of ERCOFTAC, that of combustion, was reviewed by Simone Hochgreb (Cambridge) based on a rich array of selective experiments aimed at understanding the structure and dynamics of turbulent reacting flows. These days, numerical simulations take a strong position as methods for understanding and predicting turbulent flows. An inspiring example of the use of carefully designed DNS was presented by Alfredo Pinelli (City University of London), focusing on flow manipulation based on the dynamic interaction

with localized fluid-structure interactions involving slender and deformable filaments. The use of numerical simulation and stylized geometrical modeling to understand the role of turbulence in ocean dynamics was presented by Sutanu Sarkar (UCSD), establishing basic nonlinear wave interactions near under-water ridges and slopes to provide a fluid-mechanical interpretation of deep ocean flows over realistic bottom topography. Finally, an impressive overview of turbulent Rayleigh-Benard flow, and the analogy with Taylor-Couette flow, were presented by Detlef Lohse (University of Twente) - a combination of extreme DNS on the one hand and unique experimental investigations on the other hand were instrumental to validate the unifying Grossmann-Lohse theory, translating deep fluid-mechanical understanding in a directly applicable framework for heat-transfer engineering predictions.

### Challenges of turbulent flow near a wall

In order to share some of the results presented at ETMM11, this special issue of the ERCOFTAC Bulletin brings together a selection of papers concentrating on wall-bounded flows, the modeling of their transition to turbulence as well as relating to the understanding and reduction of friction and drag. It is hoped that it transfers a flavor of the work also to interested readers that could not take part in ETMM11. Issues that were addressed during ETMM11 range from mastering the difficulties faced when simulating wall-bounded turbulence, to attempts at manipulating the flow via passive control such as tripping, and via direct actuation via blowing and suction, pressure gradients, and the application of jets.

### ETMM history

The ETMM series of Symposia was initiated in 1990, with the first conference being held in Dubrovnik. The goal was to create a highly focused forum at which academic and industrial researchers would be given the opportunity to present and discuss new developments in modelling and measurement of turbulent flows, of immediate relevance to practical applications in fluid-flow engineering and related areas.

The mission of ETMM is to foster the translation of fundamental discoveries into practically relevant models and experimental systems that serve the design process in mechanical, aeronautical and civil engineering, and the prediction of physically and geometrically complex processes in the natural environment. Until now ten

ETMM conferences were held over the past 26 years, all around the Mediterranean area:

- ETMM-1 in Dubrovnik (1990)
- ETMM-2 in Florence (1993)
- ETMM-3 in Crete (1996)
- ETMM-4 in Corsica (1999)
- ETMM-5 in Mallorca (2002)
- ETMM-6 in Sardinia (2005)
- ETMM-7 in Cyprus (2008)
- ETMM-8 in Marseille (2010)
- ETMM-9 in Thessaloniki (2012)
- ETMM-10 in Marbella (2014)

The selection of Palermo as the location for the 2016 Symposium continues ETMM's Mediterranean tradition. ETMM11 proved to be a valuable branch on the continuously growing tree of engineering knowledge and skills, helped by the friendly and collaborative atmosphere that

was brought about by the undeniable charm of Palermo and the expert organizational support by EASY Conferences. A talented community of researchers was engaged anew in the challenges of turbulence modeling, simulation and measurements of relevance to society as a whole. Contributions are most direct to the optimization of energy generation and transport processes. ETMM11 will find a natural continuation in ETMM12, to be hosted by the University of Montpellier in 2018.

Finally, a special issue of Flow Turbulence and Combustion, the ERCOFTAC Journal, will be dedicated to a selection of high quality papers whose contents will be representative of the themes presented at ETMM11.

On behalf of the ETMM11 organizing committee:

Bernard Geurts  
Vincenzo Armenio  
Domenico Borello  
Mauro De Marchis  
Enrico Napoli  
Ugo Piomelli  
Donatella Termini  
Ananias Tomboulides  
Tullio Tucciarelli

# TRIPPING EFFECTS IN LOW-REYNOLDS NUMBER TURBULENT BOUNDARY LAYERS

R. Örlü<sup>1</sup>, C. Sanmiguel Vila<sup>2</sup>, R. Vinuesa<sup>1</sup>, S. Discetti<sup>2</sup>, A. Ianiro<sup>2</sup> and P. Schlatter<sup>1</sup>

<sup>1</sup>*Linné FLOW Centre, KTH Mechanics, SE-100 44 Stockholm, Sweden.*

<sup>2</sup>*Aerospace Engineering Group, Universidad Carlos III de Madrid, Leganés, Spain.*

ramis@mech.kth.se

## Abstract

This paper presents a study focused on the development of zero-pressure-gradient turbulent boundary layers (ZPG TBL) towards canonical conditions in the low Reynolds-number range. Six different tripping configurations are employed including weak, late and strong overtripping covering a Reynolds-number range (based on momentum thickness) of  $500 < Re_\theta < 4,000$ . Evolution of the mean streamwise and variance profiles of the different TBLs is studied. Convergence towards a canonical state of the different tripping devices is determined using a new method based on the diagnostic-plot concept (Alfredsson *et al.*, 2011), which only requires mean and turbulence intensity measurements within the outer layer. Existing methods in the literature which rely on empirical skin-friction and shape-factor curves are used to validate the proposed diagnostic-plot method. Contrary to these methods, the present one does not require knowledge of the skin-friction coefficient, shape factor or wake parameter, which would need accurate measurements of friction velocity, wall position and full profile measurements in order to compute integral quantities.

## 1 Introduction

The assessment of effects such as inflow conditions, tripping devices and development length on the characteristics of zero pressure gradient (ZPG) turbulent boundary layers (TBLs) has started to receive some attention in recent years (see *e.g.* Hutchins, 2012; Schlatter and Örlü, 2012; Marusic *et al.*, 2015).

The problem is extremely relevant since, as stated by Chauhan *et al.* (2009), such effects may lead to local non-equilibrium conditions, producing flows which are no longer representative of the canonical ZPG TBL. Chauhan *et al.* (2009) analysed a vast number of experimental databases, and assessed the streamwise evolution of the wake parameter  $\Pi$  (Coles, 1962) and the shape factor  $H = \delta^*/\theta$  (where  $\delta^*$  and  $\theta$  are the displacement and momentum thicknesses, respectively), obtained from fits to a composite profile formulation. Comparison of the  $\Pi$  and  $H$  trends with the numerical integration of the composite profile allowed them to obtain a criterion to identify well-behaved profiles, *i.e.*, not affected by such non-equilibrium effects.

Interestingly, Schlatter and Örlü (2010) showed that numerical databases are also affected by inflow conditions and tripping method, which explained the observed differences up to 5% in  $H$  and up to 20% in the skin friction coefficient  $C_f$ , when comparing a wide number of direct numerical numerical simulation (DNS) databases of ZPG TBLs. In a follow-up study, Schlatter and Örlü (2012) also reported that if transition is

initiated at Reynolds numbers  $Re$  based on momentum thickness  $Re_\theta < 300$ , then comparisons between different numerical and experimental databases can be made for  $Re_\theta > 2,000$  if the flow is not severely over or undertripped (see also Örlü and Schlatter, 2013). Thus, under these conditions the ZPG TBL can be considered as *canonical*, and does not exhibit features reminiscent of its particular inflow condition.

A comparison of the evolution from three ZPG TBLs, tripped with three different tripping devices, was carried out by Marusic *et al.* (2015). In this study a standard sand paper trip was considered, together with two threaded rods designed to overstimulate the boundary layer, and it was found that the effects of the trip remained up to streamwise distances on the order of 2,000 trip heights (conclusion valid for their particular setup and trip method). Such effects were manifested on the large-scale motions in the flow.

Rodriguez-Lopez *et al.* (2016) studied the effect of different tripping configurations with the aim of generating canonical high- $Re$  TBLs. A sawtooth serrated fence and different spanwise arrays of cylinders were employed to obtain a uniform wall-normal blockage distribution case and a non-uniform one. It was shown that tripping configurations with a uniform blockage ratio can be used to obtain canonical high- $Re$  TBLs with an increase of up to 150% in momentum thickness with respect to a standard sandpaper trip.

A numerical equivalent of the aforementioned studies can be found in the work by Sillero *et al.* (2013), who reported that in one of their preliminary simulations the computational box was not long enough to allow full development of the ZPG TBL, the most prominent effect being observed in the larger scales of the flow. In their case, the inflow condition was generated through a rescaling method, different from the volume force tripping employed by Schlatter and Örlü (2010, 2012) in their simulations.

The present investigation revisits the early experimental studies on the history effects of tripping devices on turbulence characteristics at low  $Re$  (see *e.g.* Erm & Joubert, 1991) in light of the recent numerical as well as high  $Re$  experimental studies with the aim to a) assess the various criteria proposed in the literature to discern a canonical ZPG TBL and b) propose a practical method that can be employed prior to extensive measurements and/or DNS as required by present methods. For this purpose new wind tunnel experiments with six different tripping configurations have been performed, which are described in Sec. 2, and discussed and summarised in Sec. 3 and 4, respectively.

Tripping characteristics & location	Symbol code	Identification
DYMO ‘V’ @ 75 mm	Red	weak tripping
DYMO ‘V’ @ 230 mm	Green	late tripping
DYMO ‘V’ @ 75, 90, 110 mm & 5 mm square bar @ 85 mm	Blue	strong overtripping
DYMO ‘V’ @ 90, 110 mm & 2.4 mm height turbulator	Black	optimal 1
DYMO ‘V’ @ 90, 110 mm & 1.6 mm height turbulator	Magenta	optimal 2
DYMO ‘V’ @ 90 mm	Cyan	weak/late tripping

Table 1: Specifications of the tripping configurations including location and respective colour coding for symbols. The embossed (DYMO) letter ‘V’ points into the flow direction and has a nominal height of 0.3 mm

## 2 Experimental setup

The experimental data was obtained in the Minimum Turbulence Level (MTL) closed-loop wind tunnel located at the Royal Institute of Technology (KTH) in Stockholm, which has a 7 m long test section with a cross-sectional area of  $0.8 \times 1.2 \text{ m}^2$  with a streamwise velocity disturbance level less than 0.025% of the free-stream velocity. The boundary layer developed on a flat plate suspended 25 cm above the tunnel floor under a zero pressure gradient condition that was established through adjustment of the ceiling.

A variation of DYMO tape (with the embossed letter ‘V’ and a width of 9 mm with a maximum thickness of 0.5 mm) arrangements in various combinations with and w/o turbulators has been used to establish 5 different evolutions of TBLs (listed in Table 1) similar to those studied numerically in Schlatter and Örlü (2012), *i.e.*, a combination of weak, late, and strong trippings. Additionally, a square bar of length 5 mm was used to mimic a strongly overtripped case. All the tripping configurations were placed spanning the full spanwise length of the plate and at a streamwise location in the range  $75 < x/\text{mm} < 230$  from the leading edge, corresponding to the range  $130 < Re_\theta < 260$ .

Single-point streamwise velocity measurements were performed by means of a single in-house hot-wire probe with a Platinum wire of 560  $\mu\text{m}$  length and nominal diameter of 2.5  $\mu\text{m}$ . These dimensions provided sufficient spatial resolution (the wire length being smaller than 20 viscous units for all considered cases) to ensure meaningful comparisons of the higher-order turbulence statistics.

A set of 4 streamwise locations was selected for each tripping configuration with few additional stations to match  $Re_\theta$ , covering a range of  $500 < Re_\theta < 4,000$ . Care was taken to acquire sufficient measurement points within the viscous sublayer and the buffer region in order to correct for the absolute wall position and determine the friction velocity (Örlü *et al.*, 2010; Alfredsson, *et al.*, 2011b) without the need to rely on log-law constants for the mean velocity profile (*i.e.* Clauser chart method). A sampling frequency and time of 20 kHz and 30 s, respectively, were employed in all the velocity measurements, and a low-pass filter of 10 kHz cut-off frequency was used prior to the data acquisition in order to avoid aliasing.

To compute boundary-layer quantities in a consistent manner, the procedure outlined in Schlatter and Örlü (2010) was followed: The composite profile by Nickels (2004) was used to obtain the freestream velocity  $U_\infty$  and the 99% boundary-layer thickness  $\delta_{99}$ . Reynolds numbers and integral quantities were then computed using the fitted composite profile. In the present study the superscript ‘+’ denotes scaling with the friction velocity  $u_\tau$  or the viscous length  $\ell^* = \nu/u_\tau$  (where  $u_\tau = \sqrt{\tau_w/\rho}$ ,  $\tau_w$  being the mean wall-shear stress,  $\rho$  is the fluid density and  $\nu$  is the kinematic viscosity).

## 3 Results and discussion

A compilation of the streamwise mean and variance profiles for the various trippings is shown in Figure 1a-b) and depicts a clear collapse of the mean velocity profile within the inner layer. This is in accordance with Schlatter and Örlü (2012), which showed that the near-wall region (*e.g.* in terms of the skin friction or the root mean square (rms) of the fluctuating wall shear stress) quickly adapts to that of a canonical TBL. The outer layer instead, exhibiting strong variations in the mean and variance profiles, requires as expected a much longer development length to forget about its specific tripping history. In particular, the strong overtripping case shows an outer peak which is a particular feature due to the square bar used as a disturbance.

The differences in the boundary-layer evolution can be better appreciated when considering the ratios of the various boundary-layer thicknesses as shown in Figure 1c), where clearly the late and strong overtripping cases exhibit the largest discrepancies from all other cases thereby indicating that even their most downstream station has not adapted to the canonical state.

In order to determine when a TBL profile has reached a canonical state various criteria have been proposed in the literature. Among those are *e.g.* the evolution of the shape factor  $H$ , the skin-friction coefficient  $C_f$ , and the wake parameter  $\Pi$ , common reference quantities (Chauhan *et al.*, 2009). These quantities are assumed to provide a measure of when the boundary layers recover from the different boundary and inflow conditions employed. The problem with these quantities is the need to estimate with enough accuracy variables such as the wall position  $y_w$  and the friction velocity  $u_\tau$ . These parameters are typically difficult to measure directly and accurately and highly sensitive to experimental errors. Furthermore, in the low Reynolds-number range the evolution of the reference quantities  $H$  or  $\Pi$  can be defined in terms of several empirical curves, thus inheriting further uncertainties.

For these reasons, here an alternative scaling is employed, the so-called diagnostic plot (Alfredsson *et al.*, 2011a, 2012), where the root mean square of the streamwise velocity fluctuation scaled by its mean  $\sqrt{\langle uu \rangle}/U$  is plotted against the mean velocity  $U$  normalised by the free-stream velocity  $U_\infty$  rather than the wall distance, as shown in Figure 2a). This scaling has shown promising results to scale (among others) canonical ZPG TBL data covering a wide  $Re_\theta$  range throughout the logarithmic and wake layers (Örlü *et al.*, 2016). One of the key points of this scaling is the fact that, according to Alfredsson *et al.* (2011a), the data of canonical ZPG TBL collapse in the outer region for  $U/U_\infty \leq 0.9$ , following a linear relation,

$$\frac{\sqrt{\langle uu \rangle}}{U} = \alpha - \beta \frac{U}{U_\infty}, \quad (1)$$

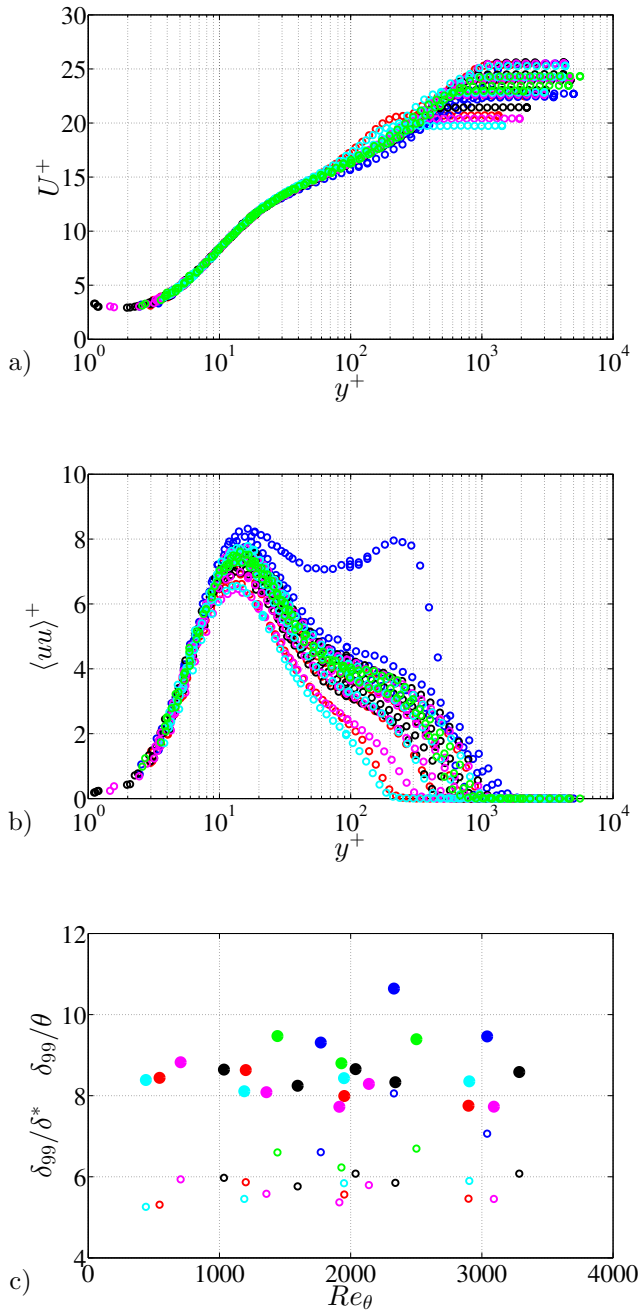


Figure 1: Inner-scaled a) mean and b) variance profile as well as the corresponding c) ratio of boundary layer thickness ( $\delta_{99}$ ) to displacement thickness ( $\delta^*$ , open symbols) and momentum-loss thickness ( $\theta$ , filled symbols) for the entire data set (see Table 1 for colour code).

where  $\alpha$  and  $\beta$  are positive fitting constants, which have an asymptotic value of  $\alpha \simeq 0.278$  and  $\beta \simeq 0.242$  for  $Re_\theta > 2,000$  in the present study.

In light of the success to scale canonical wall-bounded turbulence data (Örlü *et al.*, 2016), the profiles which follow equation (1) can be considered as canonical cases. Using this new criterion the only information required to use this method are  $U$  and  $\sqrt{\langle uu \rangle}$  in the outer region, and  $U_\infty$ . As a consequence, there is no need to obtain parameters such as  $y_w$  or  $u_\tau$ , nor to measure entire velocity profiles.

In Figure 2a) all velocity profiles are presented in the diagnostic plot, while in Figure 2b) only those that adhere to the established linear trend given through equation (1) are reported. By omitting the profiles that do not adhere to the linear scaling in the outer region, clear  $Re_\theta$ -trends in both the mean and variance profiles are revealed (Figure 3a–b), and the differences among  $Re$ -evolutions of the boundary layer thicknesses diminish as apparent from Figure 3c). The diagnostic-plot scaling is also applied in Figure 4 to the DNS of Schlatter and Örlü (2012), which consider the same  $Re_\theta$  range and similar trip configurations with the idea of extending the diagnostic-plot method to DNS data.

In order to validate the results from the diagnostic-plot scaling, the shape factor  $H$  and the skin-friction coefficient  $C_f$  evolution with  $Re_\theta$  proposed by Monkewitz *et al.* (2007) and Chauhan *et al.* (2009), respectively, are evaluated in Figure 5. It can be observed that the profiles that follow the diagnostic-plot criterion, *i.e.*, the ones shown in Figure 3 and 4, both comply with the reference  $C_f$  curve and also the  $H$  curve within  $\pm 3\%$  and  $2\%$ , respectively, as shown in Figure 5. This is an argument for the fact that the diagnostic-plot criterion provides a robust criterion to discern whether a particular boundary layer exhibits canonical ZPG TBL conditions. All profiles which do not follow the diagnostic-plot criterion either fail according to the  $C_f$  or the  $H$  based criteria.

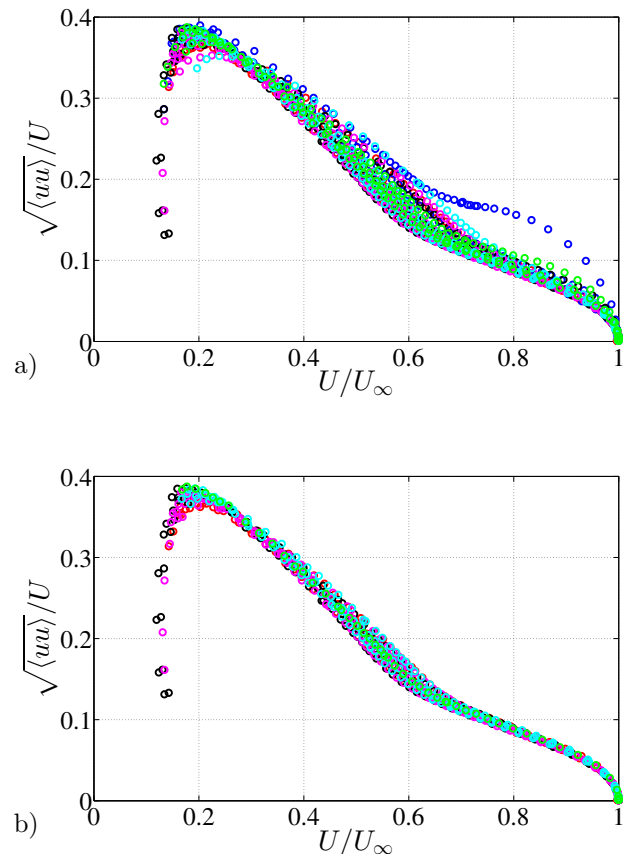


Figure 2: Extended diagnostic plot for a) the entire data set and b) the data that complies with the diagnostic-plot scaling. Note that the region  $U/U_\infty < 0.2$  corresponds to the viscous sublayer, as apparent from the misreadings of the hot-wire anemometer in the vicinity of the wall (Alfredsson and Örlü, 2010)

For example, from Figure 5 it can be observed that the cases which fulfil the  $H$  criterion (such as the lowest  $Re$  profile from the strong overtripping case) but not the  $C_f$  criterion are clearly discarded by the diagnostic-plot approach.

The previous discussion shows that the diagnostic-plot method is consistent with the reference methods employed in the literature with the advantage that it only requires measurements of the streamwise mean velocity and its turbulence intensity relatively far from the wall, where measurements are most accurate and straightforward. This method appears suitable to be employed prior to extensive measurements and/or DNS to discern when a TBL can be considered canonical or not. Since

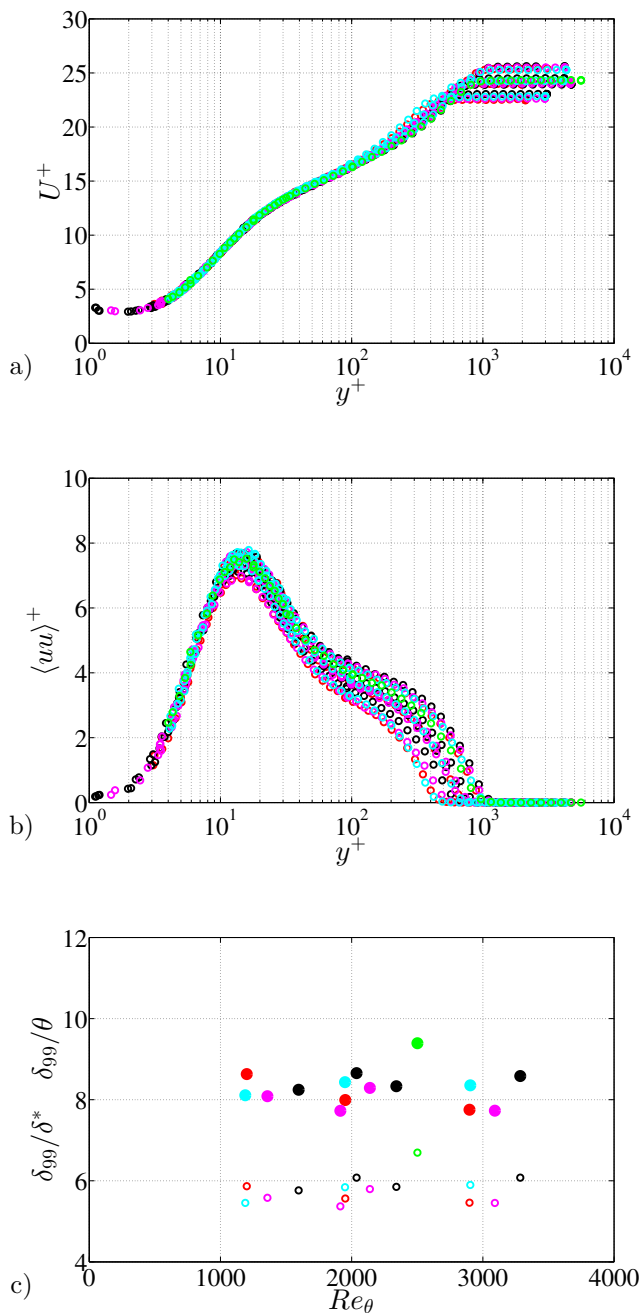


Figure 3: Same quantities as in figure 1 for experimental profiles that fulfil the diagnostic scaling in the outer layer (see Figure 2)

the outer layer in the diagnostic scaling (besides being linear) is  $Re$ -invariant when  $Re_\theta > 2,000$ , a streamwise scan through the outer layer of the TBL (which practically can easily be determined) would immediately reveal from which streamwise location on the boundary layer would adhere to that of a canonical ZPG TBL, without the necessity to measure full profiles.

## 4 Conclusions

The transition to a canonical state of zero-pressure-gradient TBLs is assessed in the present paper through the study of the evolution of six differently tripped ZPG TBLs. Streamwise velocity profiles are measured over the Reynolds number range  $500 < Re_\theta < 4,000$ , and their evolutions from the various inflow conditions are compared at several streamwise locations downstream of the flat-plate leading edge. The determination of the canonical development of the different profiles is assessed by means of the diagnostic-plot method proposed by Alfredsson *et al.* (2011a). The diagnostic-plot methodology proposed in the present study for the study of tripping effects is therefore a reliable and straightforward technique to evaluate the development of ZPG TBLs towards canonical conditions, which only requires measurements of the mean streamwise velocity and its turbulence intensity in the outer region of the boundary layer. This is a great advantage in comparison to methods based on the skin-friction coefficient, shape factor or wake parameter, which require more involved measurements of friction velocity, accurate wall position and full profile measurements in order to compute integral quantities.

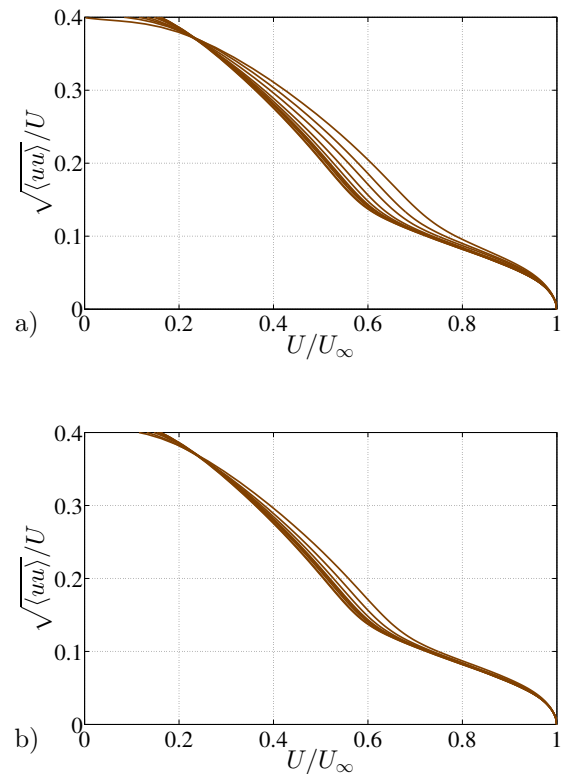


Figure 4: Extended diagnostic plot for the DNS data (Schlatter and Örlü, 2012): a) all the DNS data and b) the data that complies with the diagnostic-plot scaling

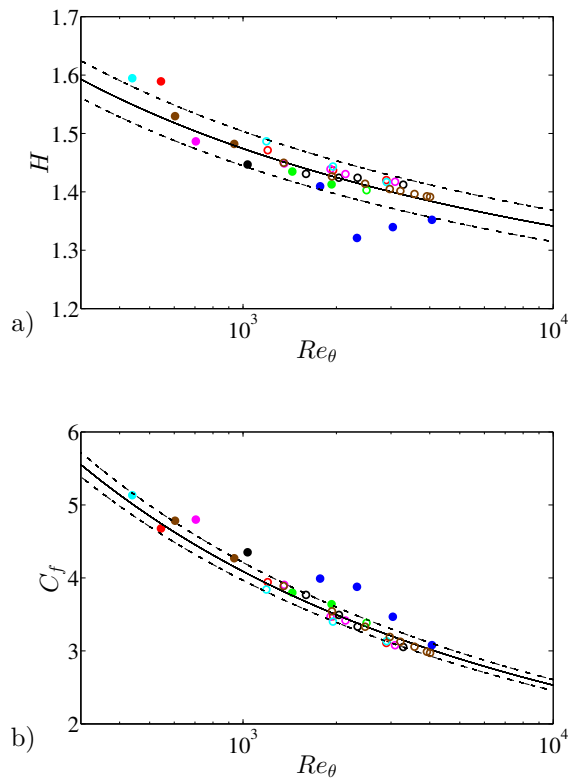


Figure 5: a) Shape factor  $H$  and b) skin-friction coefficient  $C_f \times 10^3$  evolution with  $Re_\theta$  for the entire trip data set and the DNS from Schlatter and Örlü (2012). Filled symbols are the profiles that do not follow the diagnostic-plot scaling given by equation (1). Solid lines are the references for  $H$  and  $C_f$  proposed by Monkewitz *et al.* (2007) and Chauhan *et al.* (2009) and the dashed lines show  $\pm 2\%$  and  $\pm 3\%$  tolerances, respectively

## Acknowledgments

RÖ, RV and PS acknowledge the financial support from the Swedish Research Council (VR), the Knut and Alice Wallenberg Foundation, and the Lundqvist foundation. CSV acknowledges the financial support from Universidad Carlos III de Madrid within the program “Ayudas para la Movilidad del Programa Propio de Investigación”. CSV, SD and AI were partially supported by the COTURB project (Coherent Structures in Wall-bounded Turbulence), funded by the European Research Council Coturb Grant No. ERC-2014.AdG-669505.

## References

- Alfredsson, P. H. and Örlü, R. (2010) The diagnostic plot—a litmus test for wall bounded turbulence data. *Eur. J. Fluid Mech. B/Fluids*, Vol. 42, pp. 403–406.
- Alfredsson, P. H., Segalini, A. and Örlü, R. (2011a) A new scaling for the streamwise turbulence intensity in wall-bounded turbulent flows and what it tells us about the “outer” peak. *Phys. Fluids*, Vol. 23, pp. 041702.
- Alfredsson, P. H., Örlü, R. and Segalini, A. (2012) A new formulation for the streamwise turbulence intensity

distribution in wall-bounded turbulent flows. *Eur. J. Fluid Mech. B/Fluids*, Vol. 36, pp. 167–175.

Alfredsson, P. H., Örlü, R. and Schlatter, P. (2011b) The viscous sublayer revisited—exploiting self-similarity to determine the wall position and friction velocity. *Exp. Fluids*, Vol. 51, pp. 271–280.

Chauhan, K. A., Monkewitz, P. A. and Nagib, H. M. (2009), Criteria for assessing experiments in zero pressure gradient boundary layers, *Fluid Dyn. Res.*, Vol. 41, pp. 021404.

D. E. Coles, The turbulent boundary layer in a compressible fluid (1962), *Rand. Rep. R-403-PR*.

Erm, L. P. and Joubert, P. N. (1991) Low-Reynolds-number turbulent boundary layers, *J. Fluid Mech.*, Vol. 230, pp 1–44.

Hutchins, N. (2012) Caution: Tripping hazards, *J. Fluid Mech.*, Vol. 710, pp. 1–4.

Marusic, I., Chauhan, K. A., Kulandaivelu, V. and Hutchins, N. (2015), Evolution of zero-pressure-gradient boundary layers from different tripping conditions, *J. Fluid Mech.*, Vol. 783, pp. 379–411.

Monkewitz, P. A., Chauhan, K. A. and Nagib, H. M. (2007), Self-consistent high-Reynolds-number asymptotics for zero-pressure-gradient turbulent boundary layers, *Phys. Fluids*, Vol. 19, pp. 115101.

Nickels, T. B. (2004), Inner scaling for wall-bounded flows subject to large pressure gradients, *J. Fluid Mech.*, Vol. 521, pp. 217–239.

Örlü, R., Fransson, J. H. M. and Alfredsson, P. H. (2010), On near wall measurements of wall bounded flows—the necessity of an accurate determination of the wall position, *Prog. Aerosp. Sci.*, Vol. 46, pp. 353–387.

Örlü, R. and Schlatter, P. (2013) Comparison of experiments and simulations for zero-pressure gradient turbulent boundary layers at moderate Reynolds numbers. *Exp. Fluids*, Vol. 54, pp. 1547.

Örlü, R., Segalini, A., Klewicki, J. and Alfredsson, P. H. (2016) High-order generalisation of the diagnostic plot to turbulent boundary layers. *J. Turbul.* Vol. 17, pp. 664–677.

Rodríguez-López, E., Bruce, P. J. K. and Buxton, O. R. H. (2016), On the formation mechanisms of artificially generated high Reynolds number turbulent boundary layers, *Boundary-Layer Meteor.*, Vol. 160, pp. 201–224.

Schlatter, P. and Örlü, R. (2010), Assessment of direct numerical simulation data of turbulent boundary layers, *J. Fluid Mech.*, Vol. 659, pp. 116–126.

Schlatter, P. and Örlü, R. (2012), Turbulent boundary layers at moderate Reynolds numbers: inflow length and tripping effects, *J. Fluid Mech.*, Vol. 710, pp. 5–34.

Sillero, J. A., Jiménez, J. and Moser, R. D. (2013), One-point statistics for turbulent wall-bounded flows at Reynolds numbers up to  $\delta^+ \simeq 2000$ , *Phys. Fluids*, Vol. 25, pp. 105102.

# INFLUENCE OF A LARGE-EDDY-BREAKUP-DEVICE ON THE TURBULENT INTERFACE OF BOUNDARY LAYERS

C. Chin<sup>1</sup>, N. Hutchins<sup>1</sup>, A. Ooi<sup>1</sup>, R. Örlü<sup>2</sup>, P. Schlatter<sup>2</sup> and J. P. Monty<sup>1</sup>

<sup>1</sup>Dept of Mechanical Engineering, University of Melbourne, Victoria 3010, Australia

<sup>2</sup>Linné FLOW Centre, KTH Mechanics, SE-100 44 Stockholm, Sweden

chincc@unimelb.edu.au

## Abstract

This paper investigates the effects of implementing a large-eddy break-up device (LEBU) on the growth of the boundary layer. The LEBU is placed at a wall-normal distance of  $0.8\delta$  (local boundary layer thickness) from the wall. A detail analysis of the interaction between the LEBU and the turbulent/non-turbulent interface (TNTI) is performed and the LEBU is found to delay the growth of the turbulent boundary layer. At the near-wall, the LEBU acts to reduce global skin friction drag. It is found that the structures along the TNTI is different between that of the LEBU and a normal developing turbulent boundary layer, where the structures appear smaller in length and width in the LEBU case. In addition, the LEBU disrupts the entrainment of the freestream high momentum flow into the boundary layer.

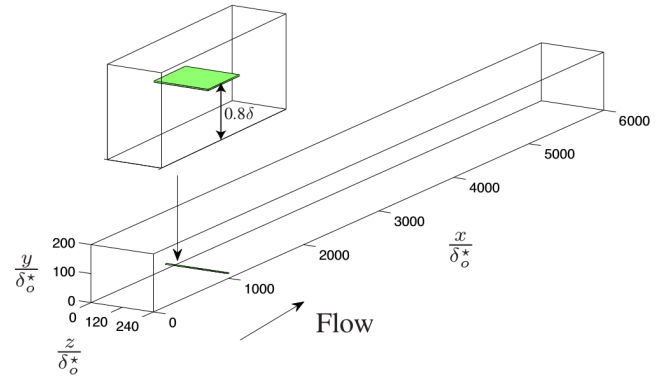


Figure 1: Computational domain of the turbulent boundary layer LES. The LEBU is imposed after a complete washthrough and performed as a separate simulation

## 1 Introduction

Coherent structures have been found to play a major role in the growth and evolution of turbulent boundary layers (TBLs) Townsend(1956), thereby opening doors for the beneficial manipulation and control Corke(1981). These lead to the birth of large-eddy break-up devices (LEBUs), which consist of one or more thin plates or airfoils placed parallel to the wall emerged in the outer part of turbulent boundary layers, and act to ‘break up’ the ‘large-eddies’. These devices were found to be capable of reducing the local skin friction by tens of percentage, however, no clear physical explanation of the mechanism has been presented. With the renewed interest in the very large-scale motions (VLSMs) as reported by Hutchins and Marusic (2007) and their influence that extends to the wall (Mathis et al 2009), re-examination of LEBUs (and other OLDs) seems pertinent, especially given recent advances in our ability to simulate developing turbulent boundary layers. One area of interest is in the turbulent/non-turbulent interface (TNTI), where it is defined as a line or surface that separates the turbulent region from the non-turbulent region. The TNTI is an important parameter in the study of boundary layers as it characterises the growth of the boundary layer and the entrainment process of high momentum flow from the free stream into the turbulent region of the boundary layer. Since the primary purpose of the LEBU is to break up large eddies, this work investigates the influence of the LEBU on the largest-scales located at the turbulent/non-turbulent interface (TNTI).

## 2 Methodology

The TBL and LEBU numerical datasets are taken from Chin et al (2015). The dataset is a well-resolved large eddy simulation (LES) of a large-eddy break-up (LEBU) device in a spatially evolving turbulent boundary layer up to  $Re_\theta \approx 4300$  is performed. Here the streamwise, wall-normal and spanwise directions are denoted as  $x, y$  and  $z$  with corresponding velocities represented as  $U + u, V + v$  and  $W + w$ . The inlet boundary condition is set to be a laminar Blasius boundary layer profile with  $Re_{\delta_o^*} = 450$ , where  $\delta_o^*$  is the displacement thickness at the inlet of the computational domain. A low amplitude forcing is imposed close to the inlet to *trip* the flow in order to achieve turbulent transition earlier. The LEBU is a flat plate that is implemented via an immersed boundary method as shown in figure 1. The LEBU is placed at a wall-normal location of  $0.8\delta$ , where  $\delta$  is the local boundary layer thickness and at a streamwise location of  $x/\delta \approx 45$  downstream from the inlet. The computational domain is  $L_x \times L_y \times L_z = 6000\delta_o^* \times 200\delta_o^* \times 240\delta_o^*$  in the streamwise, wall-normal and spanwise directions respectively (or  $L_x/\delta \times L_y/\delta \times L_z/\delta \approx 272 \times 9 \times 11$ ). The associated number of spectral collocated points is  $6144 \times 513 \times 512$ .

## 3 Results

It was previously reported by Chin et al (2015) that the maximum skin friction ( $c_f$ ) reduction for the LEBU is approximate 12% at  $x/\delta \approx 25$  downstream of the LEBU shown in figure 2. The red line denotes the TBL and the blue line is for the LEBU  $c_f$  profiles. There are

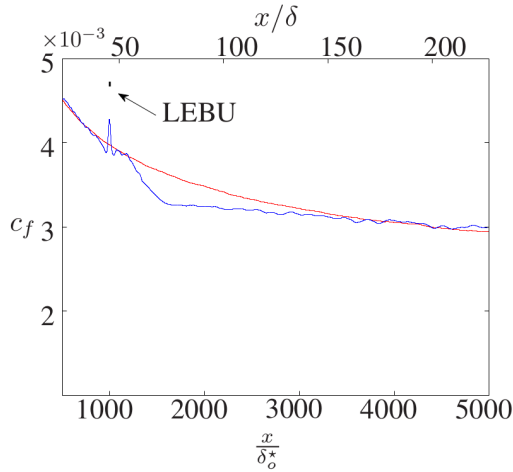


Figure 2: Comparison of the (a) skin friction coefficient  $c_f$  and (b) Reynolds number  $Re_\theta$  based on free-stream velocity and momentum thickness between LEBU and TBL. Red line denotes TBL and the blue line is LEBU

three regions of interest to investigate for the LEBU case, namely (i)  $x/\delta$  around the vicinity of the LEBU; (ii)  $x/\delta \approx 25$ , which is the location of maximum  $c_f$  reduction and (iii)  $x/\delta \approx 160$ , where the  $c_f$  appears to collapse back to the TBL profile. Since the LEBU is located at close to the edge of the boundary layer, the effects of the interaction of the LEBU and the boundary layer are further investigated.

The TNTI is detected using the instantaneous height of the boundary layer at  $U = 0.99U_\infty$ . The TNTI obtained using this method has been compared to the detection method using kinetic energy by Chauhan et al (2014) and found to be similar. Hence we adopted the identification of the TNTI to be  $U = 0.99U_\infty$ . Figure 3 shows an illustration of the method employed. The white contour denotes the instantaneous height  $H$  (the fluctuation is defined as  $h$ ) of the TNTI at various streamwise location for a given timestep and the black line indicates the mean boundary layer thickness. Figure 4 compares the fluctuation of the TNTI height  $h$  normalised by the local boundary layer thickness  $\delta_L$  of the TBL (top figure) and the LEBU (bottom figure). In the TBL case, the  $h/\delta_L$  profile exhibits consistent fluctuation values across the entire  $x/\delta$ . It is observed that these fluctuations steadily increase in size (length and width) as  $x/\delta$  increases. This increase in size is consistent with increasing Reynolds number as the boundary layer develops from left to right. In the LEBU case, the black solid line denoted the streamwise location of the LEBU, prior to the LEBU, the  $h/\delta_L$  profile is similar to the TBL. However, immediately behind the LEBU, the fluctuation is severely attenuated. This effect persists for a streamwise distance of  $x/\delta \approx 25$  downstream of the LEBU (indicated by the black dash-line in the LEBU case). Subsequently, the  $h/\delta_L$  profile appears to revert back to that of the TBL, one might notice the length-scales of these  $h/\delta_L$  fluctuations are slightly weaker and shorter than that of the TBL.

Figure 5 displays the rms profile of  $h$  for both TBL and LEBU as a function of streamwise distance. Here it is immediately clear that after the LEBU, there is severe attenuation of the fluctuation intensity  $h$ . The effect of this attenuation persists for a streamwise distance  $x/\delta \approx 100$  downstream of the LEBU before collapsing back to the TBL profile. It is interesting to note that this distance of  $x/\delta \approx 100$  corresponds to the distance we notice

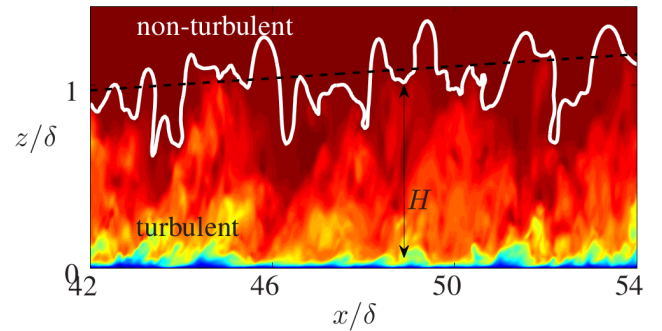


Figure 3: Detection method for the turbulent/non-turbulent interface. The interface wall-normal height ( $H$ ) is defined as  $0.99U_\infty$ . The white contour is at  $U = 0.99U_\infty$ , black contour is the mean boundary layer thickness

drag reduction in the  $c_f$  (see figure 2). The results suggest that apparently the generation of vortices from the trailing edge of the LEBU does not add to the fluctuation of the TNTI. The LEBU seems to create a shear layer (due to the wake) that stabilises the TNTI by preventing entrainment of the non-turbulent region containing large amount of energy and momentum into the turbulent boundary layer. This might be the mechanism that causes skin friction drag reduction seen in figure 2.

Next, the two point correlation will be utilised to investigate the difference in structure size in the TNTI. Two point correlation have been used to understand average structure characteristics and help identify coherent structures (see Brown and Thomas 1977). the correlation equation is given in (1).

$$R_{IJ} = \frac{\overline{I(x, y, z)J(x + \Delta x, y + \Delta y, z + \Delta z)}}{\sigma_I \sigma_J}, \quad (1)$$

where  $I$  and  $J$  correspond to the signals of interest. If  $I = J$  it is a two-point correlation, and when  $I \neq J$  it is a cross correlation. Here  $\sigma$  refers to the standard deviation, and  $\Delta x$ ,  $\Delta y$  and  $\Delta z$  are the spatial distances in the streamwise and wall-normal and spanwise directions respectively. The overbar denotes the spatial and temporal average. Figure 6 presents the cross correlation contours of  $h$  for TBL and LEBU at various locations  $x/\delta \approx 25$ , 100 and 160 downstream of the LEBU. The left column presents the results for the LEBU and the right column is for the TBL. Note that the  $x$  and  $y$  axes are normalised by the local boundary layer thickness at its corresponding streamwise location.

Figure 6(a,b) is at  $x/\delta \approx 25$ , which is where the maximum  $c_f$  reduction occurs. It is clear that the average structure at the TNTI for the LEBU is narrower and shorter. This is most likely due to the wake of the LEBU that is interacting with the boundary layer. Further downstream at  $x/\delta \approx 100$  (figure 6 c,d), it appears that the structures are similar between TBL and LEBU. However, upon closer inspection near the peak correlation contours, the LEBU is slightly narrower in width as compared to the TBL. At distance  $x/\delta \approx 160$  downstream of the LEBU, where the  $c_f$  profile of the LEBU collapses back to the TBL, the structures remain different. The structure in the TBL still is longer and wider when compared to the LEBU. Across the different streamwise locations, there is evidence to suggest that the LEBU acts to permanently alter the TNTI.

To further investigate the effects of the LEBU on the

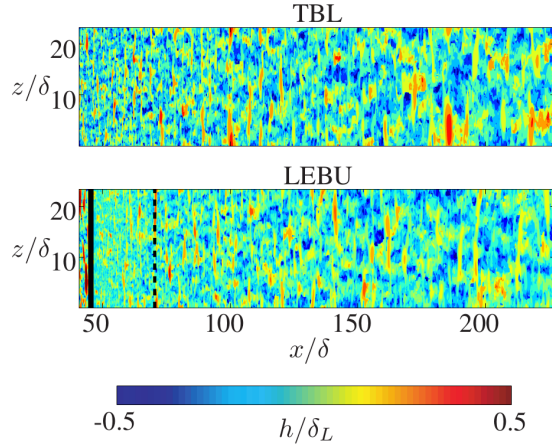


Figure 4: Contour plots of the TNTI fluctuating height  $h$  for TBL (top) and LEBU (bottom). The black solid line denotes the streamwise location of the LEBU. The black dash-line is at  $x/\delta \approx 25$  downstream of the LEBU

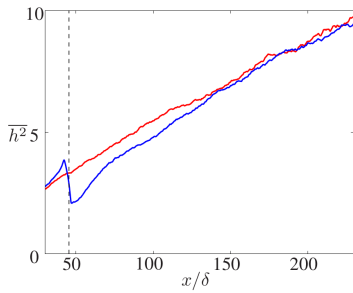


Figure 5: Comparison of the rms of  $h$  between TBL and LEBU. The red line denotes TBL and the blue line is LEBU. The black dash-line denotes the location of the LEBU

entrainment process, correlation between  $h$  and  $u$  is computed for various wall-normal distances of  $u$ . This allows the study of the direct relationship and influence of the TNTI on the velocity at a given wall-normal height. Here we have chosen the wall-normal locations of  $y/\delta_L \approx 0.1$ ,  $0.5$  and  $0.8$ , represented by red, blue and black lines respectively in figure 7. Figure 7(a) shows the results for the TBL and (b) for the LEBU, the LEBU location is denoted by the solid grey line. The results from the TBL show that there is consistently strong influence (constant correlation coefficient,  $R_{hu} \approx 0.4$ ) of the TNTI on the velocity profile at wall-normal location of  $y/\delta_L \approx 0.8$  as the boundary layer develops. The influence of the TNTI on the velocity field at  $y/\delta_L \approx 0.5$  appears relatively weak with  $R_{hu} \approx 0.1$ , which displays a somewhat linear increase in  $R_{hu}$  with  $x/\delta$ . This is expected as the fluctuation of the TNTI will increase in strength as Reynolds number increases with  $x/\delta$ . Within the logarithmic region  $y/\delta_L \approx 0.1$ , there seems to be negligible influence of the TNTI on the velocity field. In the LEBU case presented in figure 7(b), a similar trend to the TBL is noticed for  $R_{hu}$  at wall-normal distance of  $y/\delta_L \approx 0.1$ . The result for  $y/\delta_L \approx 0.5$  appears similar to that of the TBL except at the streamwise location where the LEBU is located. At this location, there is a sudden mild spike in the correlation coefficient (blue line). As the TNTI fluctuates in the wall-normal direction. This is probably due to the presence of the LEBU that increases the intermittency at  $y/\delta_L \approx 0.5$  leading to the increase in  $R_{hu}$ . The most interesting result is at  $y/\delta_L \approx 0.8$ . The cor-

relation  $R_{hu}$  is similar to that of the TBL preceding the LEBU, however, at the LEBU, there is sudden decrease in correlation. This can again be explained by the wall-normal location of the LEBU (at  $y/\delta_L \approx 0.8$ ), which has essentially zero velocity. Immediately after the LEBU, the TNTI clearly does not correlate with the shedding of vortices at the trailing edge of the LEBU, hence the low  $R_{hu}$ . The wake seems to dissipate relatively quickly and the  $R_{hu}$  collapses back to match the TBL profile at  $x/\delta \approx 100$ . This agrees with the earlier discussion that the wake disrupts the entrainment process. This is further evidence that the entrainment process is critical to understanding the drag reduction seen in  $c_f$ .

## 4 Conclusions

A detail investigation on the effects of the LEBU on the turbulent boundary layer is performed using high fidelity numerical simulation dataset. The results are compared to a spatially evolving turbulent boundary layer. The LEBU acts to permanently change the characteristics of the TNTI resulting in a shorter and narrower dominant structure at the interface and attenuates the fluctuation intensity of the TNTI. Further correlation results show that the LEBU clearly disrupts the entrainment of the high momentum flow in the freestream into the turbulent boundary layer. There is evidence to support that the mechanism for skin friction drag reduction is due to the disruption of the entrainment process. Future work will be focused on the near-wall statistics to investigate how the turbulent structures are alter in the presence of the LEBU.

## Acknowledgments

This research was undertaken with the assistance of resources provided at the NCI NF through the National Computational Merit Allocation Scheme supported by the Australian Government. Computer time was also provided by SNIC (Swedish National Infrastructure for Computing). The simulations were run at the Centre for Parallel Computers (PDC) at the Royal Institute of Technology (KTH). The authors also acknowledge the financial support of the Australian Research Council.

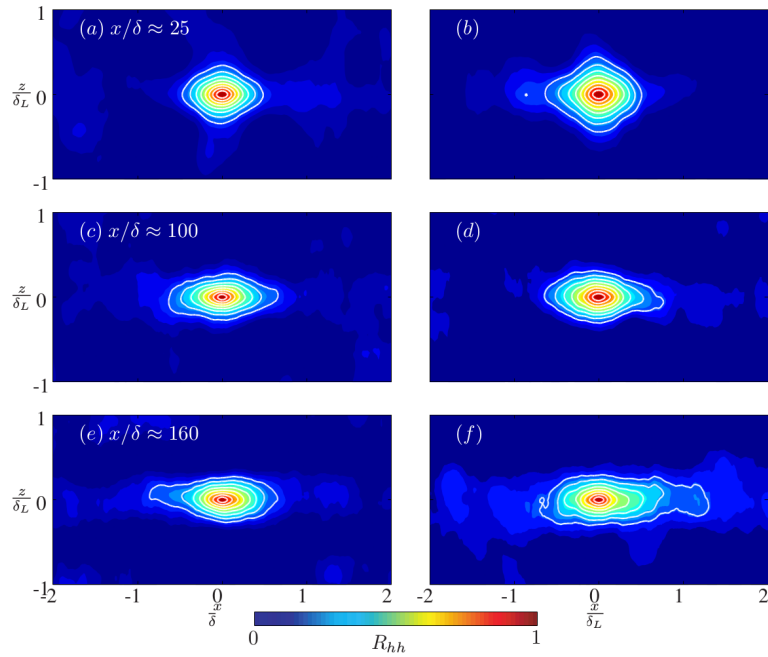


Figure 6: Cross correlation ( $R_{hh}$ ) contour map of the TNTI fluctuation height ( $h$ ) at a streamwise location of  $x/\delta \approx 25$  (a,b);  $x/\delta \approx 100$  (c,d) and  $x/\delta \approx 160$  (e,f) downstream of the LEBU. Left: TBL; Right: LEBU. The x-y axes are normalised by the local boundary layer thickness  $\delta_L$  ( $\approx 30\delta_o^*$ ,  $53\delta_o^*$  &  $69\delta_o^*$  respectively). Contour levels begin at  $R_{hh} = 0.1$  with increments of 0.1

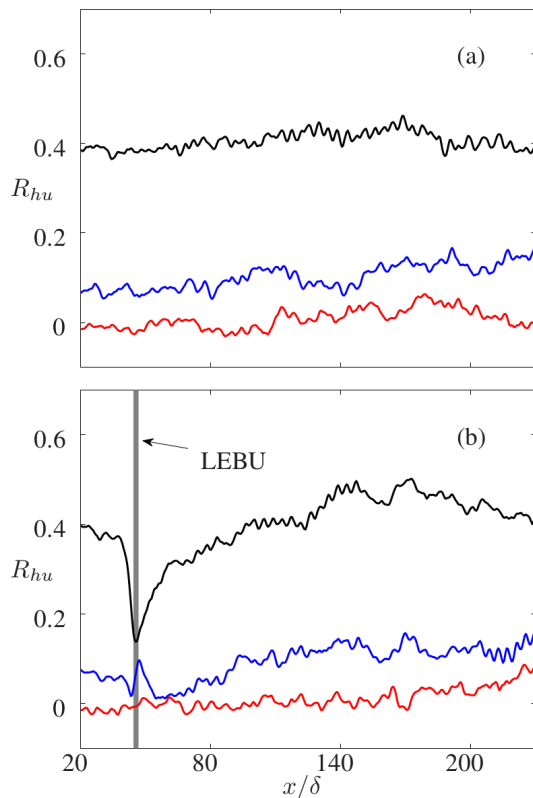


Figure 7: Cross correlation ( $R_{hu}$ ) of  $h$  and  $u$  for (a) TBL and (b) LEBU. Red line denotes correlation of  $h$  with  $u$  at  $y/\delta_L \approx 0.1$ ; blue line is for correlation of  $h$  with  $u$  at  $y/\delta_L \approx 0.5$  and black line is for correlation of  $h$  with  $u$  at  $y/\delta_L \approx 0.8$ . The grey solid line denotes the streamwise location of the LEBU

## References

- Townsend, A. A. (1976) The structure of turbulent shear flow. Cambridge University Press, 2nd ed.
- Corke, T. C., Guezennec, Y. and Nagib, H.M. (1981) Modification in drag of turbulent boundary layers resulting from manipulation of large-scale structures. NASA CR 3444.
- Hutchins, N. and Marusic, I. (2007) Evidence of very long meandering features in the logarithmic region of turbulent boundary layers. *J. Fluid Mech.* 579, 1-28.
- Mathis, R., Hutchins, N. and Marusic, I. (2009) Large-scale amplitude modulation of the small-scale structures in turbulent boundary layers. *J. Fluid Mech.* 628, 311-337.
- Chin, C., Monty, J., Hutchins, N. Ooi, A., Örlü, R. and Schlatter, P. (2015) Simulation of a large-eddy-break-up device (LEBU) in a moderate Reynolds number turbulent boundary layer, TSFP 9, Paper 1A-3.
- Chauhan, K., Philip, J. and Marusic, I. (2014) Scaling of the turbulent/non-turbulent interface in boundary layers. *J. Fluid Mech.* 751, 298-328.
- Brown, G. L. and Thomas, A. S. W. (1977) Large structure in a turbulent boundary layer. *Physics of Fluids* 20,10, S243 - S252.

# HISTORY EFFECTS AND NEAR-EQUILIBRIUM IN TURBULENT BOUNDARY LAYERS WITH PRESSURE GRADIENT

P. Schlatter<sup>1,2</sup>, R. Vinuesa<sup>1,2</sup>, A. Bobke<sup>1,2</sup> and R. Örlü<sup>1</sup>

<sup>1</sup>*Linné FLOW Centre, KTH Mechanics, SE-100 44 Stockholm, Sweden*

<sup>2</sup>*Swedish e-Science Research Centre (SeRC), Stockholm, Sweden*

pschlatt@mech.kth.se

## Abstract

Turbulent boundary layers under adverse pressure gradients are studied using well-resolved large-eddy simulations (LES) with the goal of assessing the influence of the streamwise pressure development. Near-equilibrium boundary layers were identified with the Clauser parameter  $\beta = \delta^*/\tau_w dP_\infty/dx$ . The pressure gradient is imposed by prescribing the free-stream velocity. In order to fulfill the near-equilibrium conditions, the free-stream velocity has to follow a power-law distribution. The turbulence statistics pertaining to cases with a constant Clauser pressure-gradient parameter  $\beta$  were compared with cases with a non-constant pressure distribution at matched  $\beta$  and friction Reynolds number  $Re_\tau$ . It was noticed that the non-constant cases appear to approach far downstream a certain state of the boundary layer, which is uniquely characterised by  $\beta$  and  $Re_\tau$ . The investigations on the flat plate were extended to the flow around a wing section. Comparisons with the flat-plate cases at matched  $Re_\tau$  and  $\beta$  revealed some interesting features: In turbulent boundary layers with strong pressure gradients in the development history the energy-carrying structures in the outer region are strongly enhanced, which can be detected by the pronounced wake in the mean velocity as well as the large second peak in the Reynolds stresses. Furthermore, a scaling law suggested by Kitsios *et al.* (2015), proposing the edge velocity and displacement thickness as scaling parameters, was tested on a constant pressure gradient case. The mean velocity and Reynolds stress profiles were found to be dependent on the downstream development, indicating that their conclusion might be the result of a too short constant pressure gradient region.

## 1 Introduction

Turbulent boundary layers (TBLs) subjected to streamwise pressure gradients (PGs) are of great importance in a wide range of industrial applications, including the flow around a wing or inside a diffuser. Despite their relevance, the effects of PGs on the characteristics of wall-bounded turbulence are still elusive. Since the effect of the pressure gradient on the TBL is closely related to its streamwise development, it is important to define the concept of an *equilibrium* boundary layer: according to the strict definition by Townsend (1956), this condition requires the mean flow and Reynolds-stress tensor profiles to be independent of the streamwise position  $x$ , when scaled with appropriate local velocity and length scales. As also shown by Townsend (1956) this condition is only satisfied by the sink flow, although it is possible to define a less restrictive *near-equilibrium* condition when the mean velocity defect  $U_\infty - U$  is self-

similar in the outer region, which in any case dominates at high Reynolds numbers (Marusic *et al.*, 2010). Townsend (1956) and Mellor and Gibson (1966) showed that these near-equilibrium conditions can be obtained when the free-stream velocity is defined by a power law as  $U_\infty = C(x - x_0)^m$ , where  $C$  is a constant,  $x_0$  is a virtual origin and  $m$  the power-law exponent. An additional interesting conclusion is the fact that the widely studied zero pressure gradient (ZPG) TBL, see *e.g.* Schlatter *et al.* (2009) or Bailey *et al.* (2013), driven by a constant freestream velocity, is a particular case of the general near-equilibrium TBLs proposed by Townsend (1956) and Mellor and Gibson (1966) where  $m = 0$ . Note that it is relatively common in the literature to refer to “self-similar” boundary layers, where as discussed above the only case in which complete self-similarity is observed is the sink flow.

The focus of this study is on near-equilibrium APG TBLs, and more precisely on the assessment of history effects on the boundary-layer development. To that end, we consider the Clauser pressure-gradient parameter  $\beta = \delta^*/\tau_w dP_\infty/dx$ , where  $\delta^*$  is the displacement thickness,  $\tau_w$  is the wall-shear stress and  $P_\infty$  is the free-stream pressure, to quantify the pressure-gradient magnitude and evaluate the evolution of flat-plate TBLs under various  $\beta(x)$  distributions. For this purpose, well-resolved large-eddy simulations (LES) of turbulent boundary layers with various APG conditions were carried out, and their results were compared with other available databases as described below.

## 2 Numerical method and databases

The downstream evolution of TBLs subjected to adverse pressure gradients was studied by means of well-resolved large-eddy simulations (LESs). The pressure gradient was imposed through the variation of the free-stream velocity at the top of the domain, which was defined following the near-equilibrium definition by Townsend (1956), *i.e.*,  $U_\infty(x) = C(x - x_0)^m$ . We used the code SIMSON (Chevalier *et al.*, 2007), which is based on a fully-spectral method with Fourier discretisation in streamwise and spanwise directions and on the Chebyshev-tau method in the wall-normal direction. Using the approximate deconvolution relaxation-term model as a sub-grid scale model as in Eitel-Amor *et al.* (2014), the resolution was chosen as  $\Delta x^+ = 21.5$ ,  $y_{\max}^+ = 13.9$  and  $\Delta z^+ = 9.2$  (where  $x$ ,  $y$  and  $z$  denote streamwise, wall-normal and spanwise coordinates, respectively), with 12 points below  $y^+ = 10$ . At the wall a no-slip condition was imposed, while at the upper boundary a Neumann condition was applied.

Case	Reynolds number range	$\beta$	Color code
<i>m13</i>	$700 < Re_\theta < 3515$	[0.86; 1.49]	—
<i>m16</i>	$710 < Re_\theta < 4000$	[1.55; 2.55]	—
<i>m18</i>	$710 < Re_\theta < 4320$	[2.15; 4.07]	—
<i>b1</i>	$670 < Re_\theta < 3360$	1	—
<i>b2</i>	$685 < Re_\theta < 4000$	2	—
Wing	$260 < Re_\theta < 2800$	[0; 85]	—
ZPG	$670 < Re_\theta < 2500$	0	—

Table 1: List of datasets used in the present paper, including their momentum-loss Reynolds number range, power-law exponent, Clauser pressure-gradient parameter and color code used throughout the remainder of the paper. The setup of cases *m13*, *m16* and *m18* is reported in detail by Bobke *et al.* (2016); the Wing case is described by Hosseini *et al.* (2016), and the ZPG database is reported by Schlatter *et al.* (2009)

Different near-equilibrium boundary layers were investigated by varying the virtual origin  $x_0$  and the power-law exponent  $m$  as listed in Table 1. The pressure gradients in those TBLs are of a different magnitude, and exhibit various streamwise developments. The resulting pressure gradient parameter  $\beta$  decreases over the streamwise direction in the cases *m13*, *m16* and *m18*, whereas  $\beta$  remains constant over streamwise distances of  $37\bar{\delta}_{99}$  and  $28\bar{\delta}_{99}$  in the cases *b1* and *b2*, respectively. Note that  $\bar{\delta}_{99}$  is the 99% boundary-layer thickness averaged over the region where  $\beta$  is observed to remain constant, and  $\delta_{99}$  was determined by means of the method developed by Vinuesa *et al.* (2016). Further details regarding the numerical setup of cases *m13*, *m16* and *m18* are given by Bobke *et al.* (2016). In addition to the five flat-plate APG cases discussed above, in the present study we also consider the TBL developing over the suction side of a NACA4412 wing section at  $Re_c = 400,000$  (where  $Re_c$  is the Reynolds number based on freestream velocity  $U_\infty$  and chord length  $c$ ) by Hosseini *et al.* (2016), and the ZPG TBL data by Schlatter *et al.* (2009), as shown in Table 1. The idea is that the TBL developing on the suction side of the wing is subjected to a progressively stronger APG (contrary to the flat-plate APG TBLs, in which case they are either constant or mildly relaxing), and therefore exhibits a very interesting  $\beta(x)$  distribution, which will be compared with the near-equilibrium cases developing over the flat plate. Direct numerical simulation (DNS) was considered for the wing case, and the spectral-element code Nek5000 (Fischer *et al.*, 2008) was employed, as discussed in detail in Hosseini *et al.* (2016). The DNS of ZPG TBL by Schlatter *et al.* (2009) is considered to provide a baseline case, with respect to which pressure-gradient effects can be assessed.

### 3 Effect of history on turbulence statistics

We first report the results of five near-equilibrium APG TBLs on flat plates, defined by different power-law exponents and virtual origins. As stated in §1, the state of the boundary layer will not depend on the particular value of  $\beta$  at a certain position, but on its development history, *i.e.*, on  $\beta(x)$ . While  $\beta$  decreases over the streamwise direction in the cases denoted with  $m$  (*m13*, *m16*, *m18*),  $\beta$  remains constant for the two cases denoted with  $b$  (*b1*, *b2*). Let us recall that although  $\beta$  is not constant with  $x$  in the  $m$  cases, these TBLs are in near-equilibrium

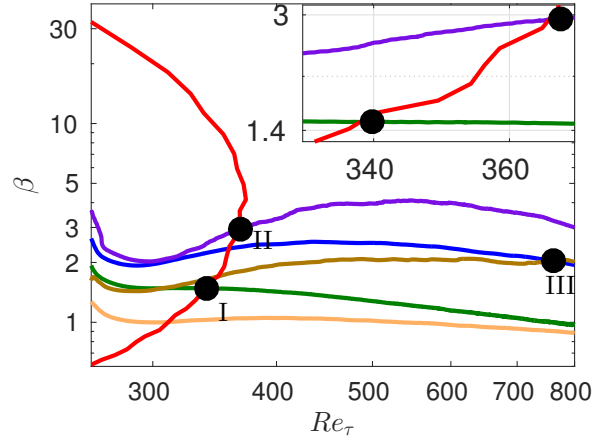


Figure 1: Clauser pressure-gradient parameter  $\beta$  as function of  $Re_\tau$  for the following cases: boundary layer developing on the suction side of a wing (Hosseini *et al.*, 2016): red, and over a flat plate for non-constant  $\beta$ -cases ( $m = -0.13$ : green,  $m = -0.16$ : blue,  $m = -0.18$ : purple) and constant  $\beta$ -cases ( $\beta = 1$ : orange,  $\beta = 2$ : brown). Inset and black dots indicate the matched  $\beta - Re_\tau$  values that will be considered in the remainder of the paper

due to the fact that the  $U_\infty$  distribution is prescribed by a power law as defined by Townsend (1956) and Mellor and Gibson (1966). Regarding the cases with constant  $\beta$ , not only are they in near-equilibrium, but they also allow a better characterization of Reynolds-number effects in a certain pressure-gradient configuration. Note that the ZPG TBL flow essentially corresponds to a constant  $\beta = 0$  configuration. In Figure 1 we show the streamwise evolution of  $\beta$ , as a function of the friction Reynolds number  $Re_\tau$  and the streamwise component  $x$ , for the various flat-plate cases as well as for the TBL on the suction side of a wing described in §2. For the flat-plate cases the inflow laminar displacement thickness  $\delta_0^*$  is used to nondimensionalise  $x$ , whereas for the case of the wing the displacement thickness at  $x/c = 0.15$ , where the flow is post-transitional, is considered. In order to evaluate the impact of different  $\beta(x)$  distributions on the local state of the APG TBL, we select three cases in which we have the same  $\beta$  and  $Re_\tau$ , but a different history of  $\beta$ . As highlighted with black dots in Figure 1, the first selected case is with  $\beta = 1.4$  and  $Re_\tau = 340$ , obtained from the wing (which starts from very low values of  $\beta$  and exhibits approximately exponential growth with  $x$ ) and from the flat-plate case *m13* (in which a decreasing trend in  $\beta$ , starting from higher values, is observed). The second case exhibits a slightly higher friction Reynolds number  $Re_\tau = 367$ , at a stronger adverse pressure gradient  $\beta = 2.9$ , and in this case also the wing is selected (with the exponentially increasing  $\beta(x)$ ), together with the flat-plate APG case *m18*, which at that point exhibits a slightly increasing trend in  $\beta$ . The third case highlighted in Figure 1 involves the two flat-plate APG TBLs *m16* and *b2*, at a higher Reynolds number of  $Re_\tau = 762$ , and with  $\beta = 2.0$ . Note that in this particular case both boundary layers are in near-equilibrium, and that the *b2* configuration exhibits a constant value of  $\beta = 2$  starting at  $x \simeq 1000$ , whereas in the *m16* case the  $\beta$  curve shows a decreasing trend.

In Figure 2 we show the inner-scaled mean flow for the various comparisons discussed above, as well as selected components of the Reynolds-stress tensor. The first two important observations from this figure are: although the

three comparisons are at the same  $\beta$  and  $Re_\tau$ , the turbulence statistics in the outer layer are essentially different among the cases, while they agree in the viscous region. This highlights the significant impact of history effects on the state of the outer layer of a turbulent boundary layer. Focusing on Figure 2(a), we can observe the general effect of a moderate APG with  $\beta = 1.4$  on the boundary layers, compared with the equivalent ZPG case: the APG TBLs exhibit a steeper logarithmic region, and a more prominent wake than the ZPG, associated with stronger energetic structures in the outer region, as also observed by Monty *et al.* (2011) and Vinuesa *et al.* (2014). With respect to the differences between the two APG cases, it is important to recall that the profiles on the suction side of the wing were obtained by means of DNS, whereas the flat-plate boundary layers are based on LES. This could be the reason for the subtle discrepancies between both profiles in the buffer region, since as documented by Eitel-Amor *et al.* (2014) the coarser resolution used in the LES produces slightly lower mean velocities in this region of the boundary layer. Nevertheless, the effect of the LES is negligible in the outer region, and therefore the differences observed in the wake of the two APG cases can be attributed to their particular streamwise evolution. Monty *et al.* (2011) showed that the APG energizes the largest turbulent structures in the outer flow, leading to the more prominent wake, as well as to the outer peak in the streamwise velocity fluctuation profile. As noticeable in Figure 1, the  $\beta(x)$  curve from the  $m13$  case exhibits values above 1.4 from the start of the pressure-gradient region, whereas in the wing the initial  $\beta$  values are close to zero, and they only reach the value 1.4 after a certain streamwise development. Therefore, in the  $m13$  case the outer flow was subjected to a stronger APG throughout its streamwise development, and therefore the larger structures received much more energy from the APG. As a consequence, and although at  $Re_\tau = 340$  the wing and the flat-plate boundary layers have the same value of  $\beta = 1.4$ , the accumulated  $\beta(x)$  effect leads to a stronger impact of the APG in the  $m13$  case. The Reynolds-stress tensor components are analyzed for this case in Figure 2(b), where again the most characteristic features of APG TBLs can be observed in comparison with the ZPG case (Monty *et al.*, 2011): the streamwise velocity fluctuation profile develops an outer peak, a consequence of the energizing of the large-scale motions, which also produces an increase of the near-wall peak due to the modulation of the near-wall region by the outer flow. Note that the location of this inner peak,  $y^+ \simeq 15$ , is essentially unaffected by the APG. The wall-normal and spanwise velocity fluctuations, as well as the Reynolds shear-stress profile, exhibit a more prominent outer region compared with the ZPG due to the effect of the APG on the outer flow. Regarding the characteristics of the two APG cases, the first noticeable feature is the fact that the value of the inner peak appears to be approximately the same in the two cases, whereas the  $m13$  case exhibits a stronger outer peak. The larger value of the outer peak can be explained, as well as the more prominent wake, by the fact that the flat-plate case was exposed to a higher accumulated  $\beta(x)$ , therefore the large-scale motions in the outer flow were effectively more energized than those in the wing. Nevertheless, it would be expected that the inner peak would also be larger in the  $m13$  case, due to the modulation effect mentioned above. A possible explanation for this apparent contradiction lies in the use of LES for the  $m13$ , which as also mentioned above does not have a noticeable effect on the outer region. Interestingly, the outer-region

wall-normal and spanwise fluctuations are also stronger in the  $m13$  case than in the wing, although the Reynolds shear-stress profiles exhibit values slightly larger in the wing. An alternative explanation might be related to the different upstream histories of the boundary layers exposed to nearly the same  $\beta$  parameter: the boundary layer on the wing increases in terms of the strength of the APG along its downstream evolution, while the TBL in the  $m = -0.13$  case stems from a stronger APG that relaxes in terms of  $\beta$ . Whereas the inner layer adapts quickly to the imposed pressure gradient, the outer layer inherits the different upstream histories further downstream, thereby yielding matched inner-layer turbulence statistics at the same  $\beta$ -value, while the outer layer exhibits amplitudes that are rather representative of the respective  $\beta$  at a more upstream station, *i.e.*, a higher and lower  $\beta$  value for the  $m = -0.13$  and wing, respectively.

The second comparison is also between a flat-plate APG and the boundary layer developing on the suction side of the wing, this time at  $\beta = 2.9$  and  $Re_\tau = 367$ . In Figure 2(c) the effect of a stronger APG on the mean flow can be observed in comparison with the ZPG, more precisely, the wake region is significantly stronger (a fact associated with much lower skin friction and the lifting up of the boundary layer by the action of the APG), and the incipient log region is steeper. Also in this case, the  $\beta(x)$  history from the flat-plate case ( $m18$ ) leads to higher accumulated effect of the APG in comparison with the wing. In particular, the  $m18$  case exhibits values of  $\beta$  starting around 2 (at the beginning of the APG region), and increasing up to the value of around 2.9 where the comparison with the wing is performed. On the other hand, in the wing the initial values are around zero and rise quickly up to the value of 2.9, but the accumulated APG effect is significantly inferior to that of the flat-plate case. This is again manifested in the more prominent wake region from the  $m18$  configuration, due to the fact that the most energetic structures in the outer flow have been exposed to a stronger APG throughout the boundary layer development. Interestingly, the discrepancy in the logarithmic and buffer regions is larger in this case than what was observed in Figure 2(a), at a lower  $\beta$ . Note that the lower velocities in the buffer region with stronger localized APGs have already been reported by Monty *et al.* (2011), and therefore it is plausible that in this case they could be caused by the different  $\beta(x)$  from the two cases. Figure 2(d) further supports the fact that the accumulated  $\beta(x)$  in the  $m18$  case leads to a much more energetic outer region compared with the wing, although the local magnitude of  $\beta$  and the Reynolds number are the same for the compared profiles. The outer peak in the streamwise fluctuations is significantly larger in the flat-plate case, and the differences in the outer region are also noticeable in the other two fluctuation components, as well as in the Reynolds shear stress (as opposed to what was observed in the lower  $\beta$  case described above). Interestingly, also in this case the inner peak in the streamwise fluctuations from the two APG TBLs exhibits approximately the same value, despite the large difference in the outer region. The attenuation effect of the LES reported by Eitel-Amor *et al.* (2014) is also around 4% at this  $Re_\tau$  in ZPG TBLs, therefore it can also be argued that the inner peak would be marginally larger in the  $m18$  than in the wing if a DNS had been performed.

Finally, in Figure 2(e) we compare the mean flow from two flat-plate cases, one with a constant  $\beta$  region ( $b2$ ), and the other one with no constant  $\beta$  ( $m16$ ); both in

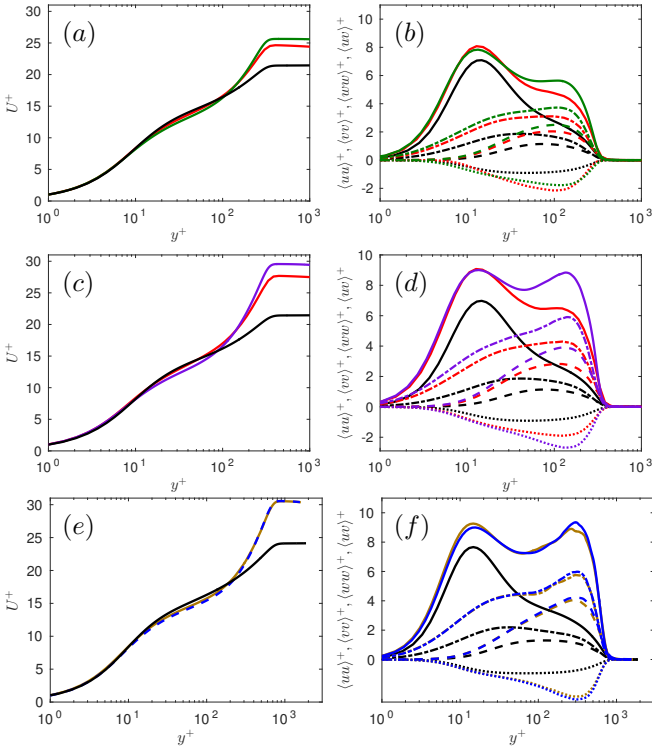


Figure 2: (a),(c),(e) Inner-scaled mean velocity profiles of the wing (red),  $m = -0.13$  (green),  $m = -0.16$  (blue),  $m = -0.18$  (purple),  $\beta = 2$  (brown) and ZPG (black). (b),(d),(f) Variation of the inner-scaled Reynolds stress profiles:  $\langle uu \rangle^+$  (solid),  $\langle vv \rangle^+$  (dashed),  $\langle ww \rangle^+$  (dot-dashed) and  $\langle uv \rangle^+$  (dotted). (a),(b) I:  $\beta = 1.4$  and  $Re_\tau = 340$ . (c),(d) II:  $\beta = 2.9$  and  $Re_\tau = 367$ . (e),(f) III:  $\beta = 2.0$  and  $Re_\tau = 762$

near-equilibrium. In particular, the comparison is done at  $\beta = 2$  and at a higher friction Reynolds number of  $Re_\tau = 762$ . The effect of the APG is also noticeable in this case, with the more prominent wake and lower velocities in the buffer region, in comparison with the ZPG. Note that the  $U_\infty^+$  value from the flat-plate boundary layers is around 30, approximately the value obtained in the  $m18$  case. Interestingly, this inner-scaled freestream velocity is obtained here with a lower  $\beta$  (2 instead of 2.9), but higher  $Re_\tau$  (762 instead of 367). This, together with the similarities between Figure 2(f) and d) in terms of inner and outer peaks of the streamwise velocity fluctuations, suggests certain connections between Reynolds-number and pressure-gradient effects. More precisely, a low- $Re$  APG TBL may exhibit features of a high- $Re$  ZPG TBL, if the magnitude of the APG is strong enough. This also points towards certain connections between the energizing mechanisms in the outer flow present at higher Reynolds numbers and with stronger APGs. Focusing on Figure 2(e), it is interesting to note that the two flat-plate cases exhibit very good agreement in their mean flow profiles, although their streamwise developments are different. Nevertheless, Figure 1(b) shows that although the  $m16$  exhibits a decreasing trend in  $\beta(x)$ , and in the  $b2$  a region of constant  $\beta$  is observed, from  $x \simeq 1500$  to around 2000 (location where the comparison is done), the two curves converge, and the relative differences between the two curves are below 15%. Hence, both APGs share a similar upstream history for about 6.5 local boundary-layer thicknesses. Regarding the components of the Reynolds-stress tensor shown in Figure 2(f), first of all the pressure gradient effects (combined with

the moderate  $Re_\tau$  of 762) lead to significantly more energized components in the outer region compared with the ZPG, as well as a larger near-wall peak in the streamwise component. Interestingly, in this case the outer peak of the streamwise velocity fluctuations is slightly larger than the inner peak; a phenomenon that suggests the development of a different energy distribution throughout the boundary layer, compared with that of moderately high ZPG TBLs. Such an overtaking of the inner peak by an outer peak has for instance been predicted by the diagnostic profile as shown by Alfredsson *et al.* (2012), although there, the outer peak resided within the overlap region, which is not the case for strong APGs. The other significant observation is the fact that the two flat-plate APG boundary layers exhibit very good agreement in all the components of the Reynolds-stress tensor, again highlighting the convergence of the two boundary layers towards the same state. These results suggest that, in this particular configuration with a moderately changing  $\beta$ , a streamwise distance of around  $x/\delta_0^* \simeq 500$  (where  $\delta_0^*$  is the displacement thickness of the inflow laminar boundary layer), corresponding to  $6.5\delta_{99}$ , may be sufficient for the APG TBL to become independent of its initial downstream development, and converge towards a certain state uniquely characterized by the  $\beta$  and  $Re_\tau$  values.

## 4 Assessment of alternative scaling laws

Due to the significant impact of history effects on the local flow features as discussed above, in this work we aim at characterizing configurations with values of  $\beta$  constant over a significant portion of the domain. As observed by Mellor and Gibson (1966), the constant  $\beta$  configuration is a particular case of near-equilibrium TBL, and therefore the  $U_\infty(x)$  is also defined by a power law with particular choices of  $x_0$  and  $m$ . A detailed characterization of constant  $\beta$  cases will ultimately allow to assess pressure-gradient effects with progressively more complex history effects, given by the particular  $\beta(x)$  distribution. In the present work we obtained a configuration exhibiting a constant value of  $\beta = 1$  in the range  $500 < x < 2300$ , and another one with a constant value of  $\beta \simeq 2$  in the range  $1000 < x < 2300$ . In Figure 3 we show a schematic representation of the constant  $\beta = 1$  region, in comparison with the one obtained in the recent work by Kitsios *et al.* (2015), also for a constant  $\beta = 1$  case. Note that although Kitsios *et al.* (2015) explored higher Reynolds numbers than the ones considered here, the range over which  $\beta$  is constant is 1.6 times larger in the present simulation.

Figures 4(a) and (b) show the inner-scaled mean flow and velocity fluctuations corresponding to case  $b1$ , schematically discussed in Figure 3. The profiles within the region of constant  $\beta = 1$  are highlighted in the two panels. The mean flow shows all characteristic features of APG TBLs, as discussed in §3. Moreover, the velocity fluctuations develop an outer peak in all components, connected with the most energetic structures in the outer region. An alternative scaling for these quantities was considered by Kitsios *et al.* (2015) in their simulation, based on the displacement thickness  $\delta^*$  and the local edge velocity  $U_e$ . They observed an apparent collapse of the mean flow and the fluctuations in their region of constant  $\beta$ , which as indicated in Figure 3 corresponds to a streamwise distance of around 23 integrated boundary-layer thicknesses  $\bar{\delta}$ . In Figures 4(c) and (d) we apply the

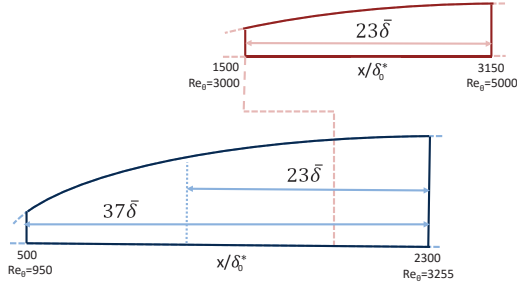


Figure 3: (Blue) Sketch of the APG turbulent boundary layer showing the area where a constant value of  $\beta = 1$  was obtained, where  $\delta_0^*$  is the displacement thickness of the laminar inflow boundary layer. (Red) Domain of interest with  $\beta = 1$  extracted from the study by Kitsios *et al.* (2015). The extent of the constant  $\beta = 1$  regions are shown in both cases normalized with the averaged boundary-layer thicknesses  $\bar{\delta}$ . The extent of the domain of interest from Kitsios *et al.* (2015) is also represented in our case

same scaling to our data, and we do not observe such a collapse in any of the investigated quantities in our constant  $\beta$  region, which spans a longer streamwise distance of  $37\bar{\delta}$ . One possible explanation for this discrepancy could be that the scaling considered by Kitsios *et al.* (2015) does not lead to self-similarity, and since their constant  $\beta$  region is shorter than ours and their  $Re$ -range spans only 20% of a decade, their streamwise development would be insufficient to reveal this conclusion. The present data exhibits a clear  $Re$  trend (spanning 23% of a decade in  $Re_\theta$ ), which is furthermore extended through the higher  $Re$  data by Kitsios *et al.* (2015). This would indeed be in agreement with Townsend (1956), since in principle the sink flow is the only flow that can be described from the wall to the free-stream in terms of a single similarity variable in  $y$ . These aspects are further explored by analyzing the constant  $\beta = 2$  case, over a streamwise distance of  $28\bar{\delta}$ . A higher  $Re_\theta$  range is reached in this case, which is more comparable to the one analyzed by Kitsios *et al.* (2015), albeit at a higher value of  $\beta$ . As seen from Figures 4(e) and (f), the scaling by Kitsios *et al.* (2015) does not lead to self-similarity in this case either. Also here a clear  $Re$  trend is noticed, supporting the statements presented above, and also the validity of the classic two-layer similarity, at least for the  $\beta$  range under consideration.

## 5 Conclusions

The present study is focused on the history effects in turbulent near-equilibrium boundary layers with pressure gradients. After defining the *near-equilibrium* state according to Townsend (1956), large-eddy simulations were performed over a flat plate to assess the effect of different evolutions of the pressure-gradient parameter  $\beta$ . The adverse pressure gradient was imposed by a varying free-stream velocity profile at the top of the domain, *i.e.*, in the free-stream. Hereby constant and non-constant pressure distributions were achieved. With the constant pressure gradients, turbulent boundary layers at a certain state (due to the imposed pressure distribution), can be investigated over a wide range of Reynolds numbers. An interesting finding was obtained when comparing the mean and Reynolds stress profiles of the non-constant pressure and constant APG TBLs at matched

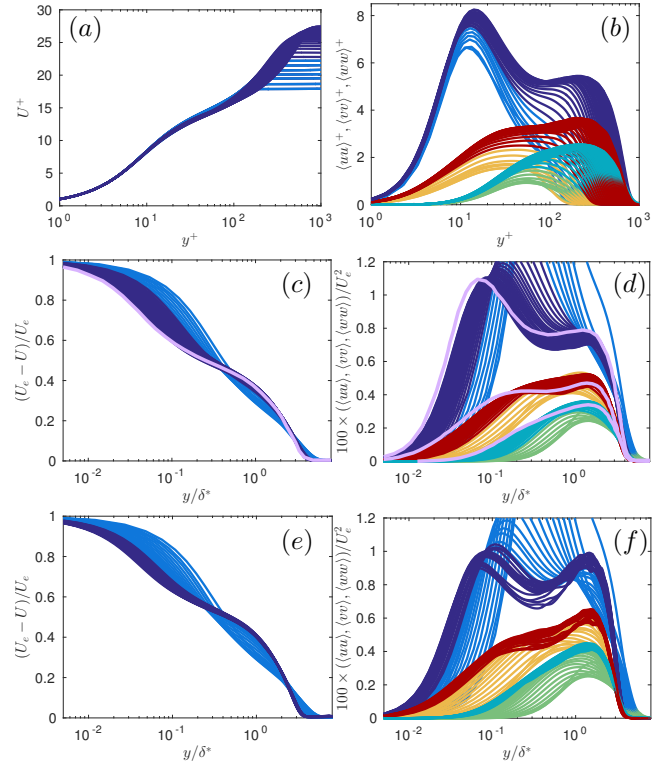


Figure 4: Case  $\beta = 1$ : Mean velocity profiles (31 positions in the range of  $100 < x < 2300$ ) non-dimensionalised by (a)  $u_\tau$  and  $l^* = \nu/u_\tau$ , (c)  $U_e$  and  $\delta^*$ . Dark blue indicates the area of constant  $\beta$  and light blue the non-constant  $\beta$  region. Reynolds-stress profiles non-dimensionalised by (b)  $u_\tau$  and  $l^* = \nu/u_\tau$ , (d)  $U_e$  and  $\delta^*$ . Dark blue, turquoise, red denotes the constant  $\beta$  region for  $\langle uu \rangle, \langle vv \rangle, \langle ww \rangle$ , respectively, and light blue, green, yellow indicate the non-constant  $\beta$  region. Scaled profiles reported by Kitsios *et al.* (2015): purple. Case  $\beta = 2$ : (e) Mean velocity profiles (23 positions in the range of  $100 < x < 2300$ ). (f) Reynolds-stress profiles

$\beta$  and  $Re_\tau$ . The non-constant  $\beta$  case appears to converge towards the canonical state after a sufficiently long downstream length. For the conditions investigated in the present study, this length is  $6.5\delta_{99}$ . The history effects were studied not only in flat-plate TBLs, but also in the APG boundary layer developing over the suction side of a NACA4412 wing section. The large structures in the outer region were found to be less energetic on the suction side of the wing than in the flow over the flat plate for matched  $\beta$  and  $Re_\tau$ . The structures were exposed to a lower PG over the streamwise direction (compared to the ones over the flat plate), resulting in a less pronounced wake region and a less intense outer region in the Reynolds stresses. A connection between PG TBLs and high- $Re$  ZPG TBLs might be able to be drawn, since the mechanisms, by which the large-scale motions are energised, in APG TBLs seem to share some similar features with those present in high- $Re$  ZPG TBLs. Finally, we investigated the scaling proposed by Kitsios *et al.* (2015), in which  $\delta^*$  and  $U_e$  are considered as length and velocity scales. Our results show that this scaling does not lead to self-similar boundary layer profiles in the constant  $\beta$  region. This conclusion is in agreement with Townsend, who showed that the sink-flow is the only boundary layer exhibiting self-similarity. Stronger streamwise constant pressure gradients at higher Reynolds numbers should be investigated

in order to characterise cases closer to wind-tunnel experiments and general applications.

## Acknowledgments

The simulations were performed on resources provided by the Swedish National Infrastructure for Computing (SNIC) at the PDC Center for High Performance Computing at KTH Stockholm. Financial support provided by the Knut and Alice Wallenberg Foundation, the Swedish Research Council (VR) and the Lundequvist Foundation is gratefully acknowledged.

## References

- Alfredsson, P. H., Örlü, R. and Segalini, A. (2012), A new formulation for the streamwise turbulence intensity distribution in wall-bounded turbulent flows, *Eur. J. Mech. B/Fluids*, Vol. 36, pp. 167–175.
- Bailey, S. C. C., Hultmark, M., Monty, J. P., Alfredsson, P. H., Chong, M. S., Duncan, R. D., Fransson, J. H. M., Hutchins, N., Marusic, I., Mckeeon, B. J., Nagib, H. M., Örlü, R., Segalini, A., Smits, A. J. and Vinuesa, R. (2013), Obtaining accurate mean velocity measurements in high Reynolds number turbulent boundary layers using Pitot tubes, *J. Fluid Mech.*, Vol. 715, pp. 642–670.
- Bobke, A., Vinuesa, R., Örlü, R. and Schlatter, P. (2016), Large-eddy simulations of adverse pressure gradient turbulent boundary layers, *J. Phys.: Conf. Ser.*, Vol. 708, pp. 012012.
- Chevalier, M., Schlatter, P., Lundbladh, A. and Henningson, D. S. (2007), SIMSON— A pseudo-spectral solver for incompressible boundary layer flow, *Tech. Rep. TRITA-MEK 2007:07*, KTH Mechanics.
- Eitel-Amor, G., Örlü, R. and Schlatter, P. (2014), Simulation and validation of a spatially evolving turbulent boundary layer up to  $Re_\theta = 8300$ , *Int. J. Heat Fluid Flow*, Vol. 47, pp. 57–69.
- Fischer, P. F., Lottes, J. W. and Kerkemeier, S. G. (2008), Nek5000: Open source spectral element CFD solver, Available at: <http://nek5000.mcs.anl.gov>
- Monty, J. P., Harun, Z. and Marusic, I. (2011), A parametric study of adverse pressure gradient turbulent boundary layers, *Int. J. Heat Fluid Flow*, Vol. 32, pp. 575–585.
- Hosseini, S. M., Vinuesa, R., Schlatter, P., Hanifi, A. and Henningson, D. S. (2016), Direct numerical simulation of the flow around a wing section at moderate Reynolds number, *Int. J. Heat Fluid Flow*, doi:10.1016/j.ijheatfluidflow.2016.02.001
- Kitsios, V., Atkinson, C., Sillero, J. A., Borrell, G., Gungor, A., Jiménez, J. and Soria, J. (2015), Direct numerical simulation of a self-similar adverse pressure-gradient turbulent boundary layer, *Proc. 9th Intl Symp. on Turbulence and Shear Flow Phenomena*, Melbourne, Australia.
- Marusic, I., Mckeeon, B. J., Monkewitz, P. A., Nagib, H. M., Smits, A. J. and Sreenivasan, K. R. (2010), Wall-bounded turbulent flows at high Reynolds numbers: Recent advances and key issues, *Phys. Fluids*, Vol. 22, pp. 065103.
- Mellor, G. L. and Gibson, D. M. (1966), Equilibrium turbulent boundary layers, *J. Fluid Mech.*, Vol. 24, pp. 225–253.
- Schlatter, P., Örlü, R., Li, Q., Brethouwer, G., Fransson, J. H. M., Johansson, A. V., Alfredsson, P. H. and Henningson, D. S. (2009), Turbulent boundary layers up to  $Re_\theta = 2500$  studied through simulation and experiment, *Phys. Fluids*, Vol. 21, pp. 051702.
- Townsend, A. A. (1956), *The Structure of Turbulent Shear Flow*, Cambridge Univ. Press, Cambridge, UK.
- Vinuesa, R., Bobke, A., Örlü, R. and Schlatter, P. (2016), On determining characteristic length scales in pressure-gradient turbulent boundary layers, *Phys. Fluids*, Vol. 28, pp. 055101.
- Vinuesa, R., Rozier, P. H., Schlatter, P. and Nagib, H. M. (2014), Experiments and computations of localized pressure gradients with different history effects, *AIAA J.*, Vol. 55, pp. 368–384.

# INVESTIGATION OF TURBULENT BOUNDARY LAYERS APPROACHING SEPARATION

A. Drózdź<sup>1</sup> and W. Elsner<sup>1</sup>

<sup>1</sup>*Institute of Thermal Machinery, Czestochowa Univ. of Tech.,  
Armii Krajowej 21, 42-201, Czestochowa, Poland*

welsner@imc.pcz.czyst.pl

## Abstract

The present paper deals with the experimental analysis of strong decelerated turbulent boundary layer developed on a flat plate. The special design of the test section equipped with perforated, movable upper wall allow to generate on the bottom wall turbulent boundary layer, which is at the verge of separation. The objective of the work is to examine the effects of pressure gradient on non-equilibrium boundary layer, while indicating local areas of equilibrium flow. The emphasis is on the analysis of mean flow statistics i.e. streamwise Reynolds stress and mean velocity profiles.

It has been shown that a small increase in the pressure gradient induced by applied suction on the upper wall causes a significant response of boundary layer on the bottom wall. It results in stronger deformation of mean velocity profiles and faster decay of  $u'u'$  inner peak. Comparative analysis with external data indicates that turbulent boundary layer structure depends not only on the local effects of pressure gradient, but also on the upstream history of the flow.

## 1 Introduction

Among various types of near wall flows the turbulent boundary layers (TBLs) subjected to an adverse pressure gradient (APG) are in the spotlight. If a turbulent boundary layer flow encounters a strong APG, the flow becomes unstable and, if the APG is sufficiently large, it separates from the surface. The existence of separation involves an increase of energy losses connected sometimes with pressure and velocity fluctuations. The evidence of the latter phenomenon was given by Cherry et al. (1984), who investigated the unsteady structure of a separated and reattaching flow. Unstable location of turbulent separation results among the other from the impact of vortex structures that fall into the area of separation, causing a temporary increase in momentum. An extensive phenomenological description of the flow separation distinguishing various stages of separation was given by Simpson (1989). The turbulent boundary layer that is maintained on the verge of separation has already been studied numerically and experimentally (Elsberry et al. 2000; Gungor et al. 2016; Krogstad and Skare 1995; Skote and Henningson 1998). Krogstad and Skare claim that the flow close to separation exhibited a definite non-equilibrium character, indicated by the different scales required for collapse of the mean velocity and turbulence intensity profiles. Castillo et al. (2004) showed, however that outer part of turbulent boundary layer under strong adverse pressure gradient and even near and past the separation tends to remain in equilibrium state.

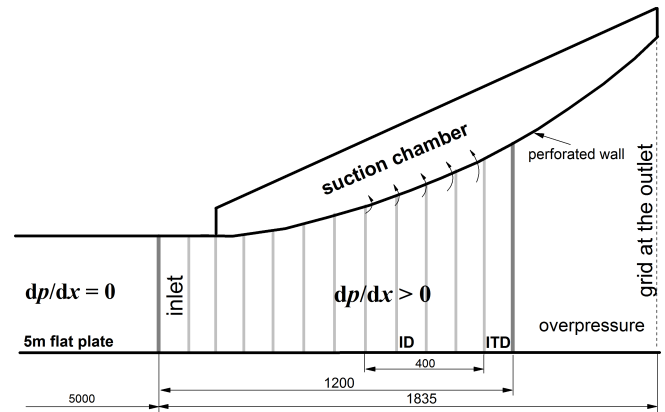


Figure 1: Test section geometry

As it was mentioned by Gungor et al. (2014) there is a lack of well-documented data sets near boundary layer detachment. The paper deals with the experimental analysis of strong decelerated turbulent boundary layer developed on the flat plate. The newly developed test section allows to generate on the bottom wall turbulent boundary layer, which is at the verge of separation. The objective of the work is to examine the effects of pressure gradient on non-equilibrium boundary layer, while indicating local areas of equilibrium flow.

## 2 Experimental setup

Experimental investigations were performed in an open-circuit wind tunnel, where the turbulent boundary layer developed along the flat plate, which is 6,87 m long. The wind tunnel is designed with large dimension settling chamber and three contraction sections, which allows to achieve free stream turbulence intensity below 1% at the inlet plane. The inlet rectangular channel with a length of 5.035 m located upstream the proper test section has two pairs of suction gaps aimed to control the two-dimensionality of the flow by minimizing of boundary layers on the side walls. A slight inclination of the upper wall helped to keep zero pressure gradient (ZPG) conditions at the at the entire length of this section. The specially design test section located at the end of the wind-tunnel (see figure 1) is equipped with perforated, movable upper wall. Computer-controlled suction system equipped with a low power axial compressor allows for smooth adjustment of the amount of the exhausted air from the top of the wall. Changing the shape and position of the upper wall as well with the suction flux it is possible to generate wide range of pressure gradient conditions, while at the inlet channel the zero pressure

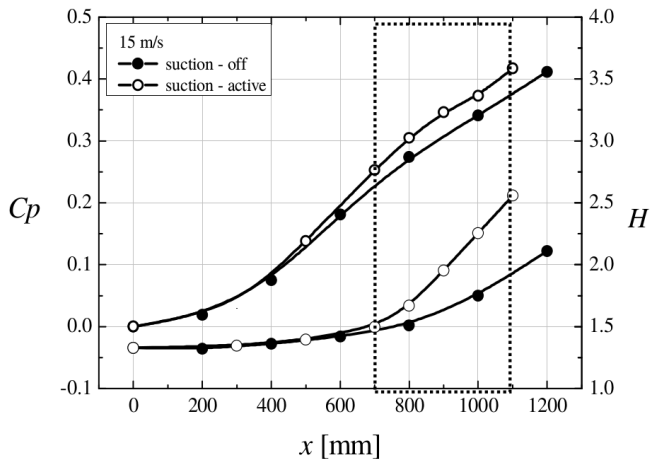


Figure 2: Pressure coefficient,  $C_p$  and shape factor,  $H$  distributions

gradient conditions were secured. The static pressure in the test section is controlled by the throttling at the outlet of the test section. For certain pressure conditions it is possible to generate on the bottom wall the turbulent boundary layer, which is at the verge of separation. Flow parameters determined in core flow at the inlet plane to test section (i.e. 5035) mm downstream the flat plate leading edge), located in the zero pressure gradient area, are the mean velocity  $U \approx 10, 15$  and  $20$  m/s and turbulence intensity  $Tu < 1\%$ . The inlet Reynolds number based on friction velocity and boundary layer thickness was equal 1900, 2600 and 3300 respectively. However, in the paper only intermediary set of data are analyzed.

The measurements were performed with hot-wire anemometry CCC developed by Polish Academy of Science in Krakow. A single hot-wire probe of a diameter  $d = 3 \mu m$  and length  $l = 0.4$  mm was used. In the experiment for each case the wire length was always below 20 in inner variables as it was recommended by Ligrani and Bradshaw (1987). The ambient conditions were carefully controlled during the measurements. In the course of a single profile measurement the scatter of ambient temperature at the end of the test section did not exceed  $\pm 0.2^\circ$ . At the same time the free-stream velocity was monitored by the means of a Prandtl's tube.

Acquisition was maintained at frequency 25 kHz with 30 s sampling records. The grey lines in Fig. 1 represent the positions where the measurements of velocity profiles on flat plate were performed.

### 3 Results

Initially the effect of flow suction was examined. For this purpose, measurements were performed for reference case (Suction-off), where no suction was applied and for Suction-on, with assumed flow suction, where external conditions were set in order to achieve turbulent boundary layer with incipient separation at the end of test section. The underpressure in the suction chamber of  $\Delta P = 25$  Pa caused the suction of the upper boundary layer and as consequence the change of the flow conditions on the lower plate. The flow conditions are characterized by pressure coefficient:

$$C_p = \left(1 - \frac{U_\infty}{U_{\infty 0}}\right)^2 \quad (1)$$

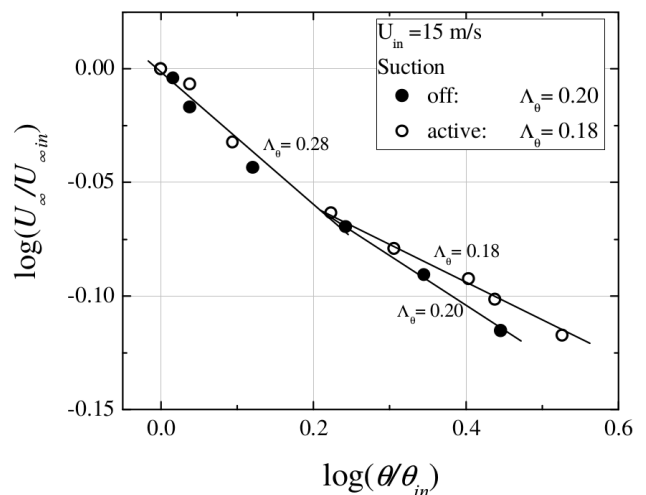


Figure 3: Distribution of pressure gradient  $\Lambda$

where  $U_{\infty 0}$  is the maximal mean velocity for inlet zero pressure gradient conditions. Figure 2 presents the distributions of  $C_p$  and shape factor  $H$  in the streamwise direction for inlet velocity 15 m/s. The effect of the suction is clearly seen by elevation of  $C_p$  parameter downstream  $x = 600$  mm. The reaction of  $H$  is a little delayed. One can observe much more rapid increase of  $H$  in the reference to suction-off case from  $x = 700$  mm indicating the stronger process of the flow destabilization.

Next figure (Fig. 3) presents the  $U_\infty$  versus  $\theta$  reduced by inlet values in double logarithmic scale following the concept of Castillo and George (2001), who proposed pressure parameter  $\Lambda_\theta$  as a criterion of locally equilibrium flows. As can be seen,  $\Lambda_\theta$  is constant only in some parts of the flow. Initially the value of  $\Lambda_\theta$  is equal to 0.28, but moving towards the separation it changes the value to 0.20 for suction-off and 0.18 for suction-on. This means that in both cases the analyzed boundary layer is nonequilibrium one, however, it can be stated that it remains in local equilibrium.

Separation of turbulent boundary layer is a very complex process, and it is difficult to predict properly the position of separation. There are number of separation criteria available in the literature and their valuable review was published by Castillo et al. (2004). According to Simpson definition Insipient Detachment (ID) is, when the reverse flow occurs only 1% of the time and Intermittent Transitory Detachment ITD is, when the reverse flow occurs about 20% of the time. This last point is a bit ahead of detachment point, where the time averaged wall shear stress is zero. For the purposes of this study it was decided to use the criterion proposed by Sandborn and Kline. (1961). They showed that the shape factor defined as:

$$H_{sep} = 1 + \frac{1}{1 - \delta^*/\delta} \quad (2)$$

has a value 2.7 at the Intermittent Transitory Detachment (ITD) position. Fig. 4 presents the downstream evolution of  $H_{sep}$ . For the reference non-suction case the value of  $H_{sep}$  parameter reaching the level above 2.5 at 1200 mm. For the suction case the changed conditions forced the earlier boundary layer separation, what is confirmed by the significant change of  $H_{sep}$  distribution, which is due to the abrupt rise of the displacement thickness. It can be seen that the  $H_{sep}$  is closed to 2.7 for 1100 mm, which means that ITD point is almost reached. Selected profiles of the mean velocity and streamwise

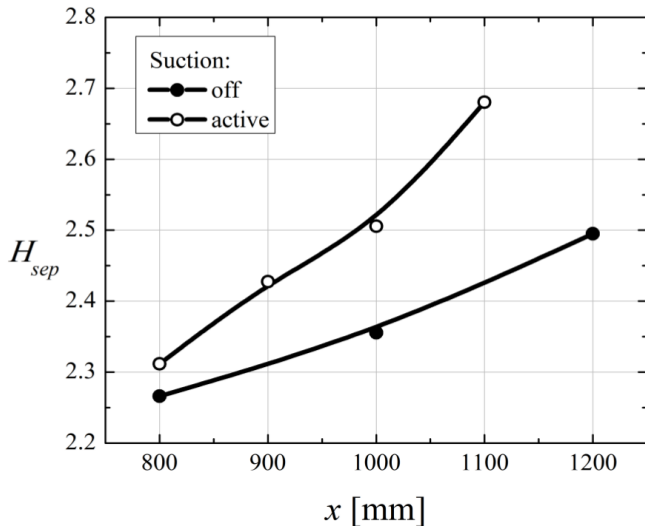


Figure 4: Distribution of shape factor  $H_{sep}$

Reynolds stresses for 15 m/s and for both cases are presented in Fig. 5. The mean velocity is normalized by the local freestream velocity  $U_\infty$  and Reynolds stress by outer scale velocity,  $U_0 = 2(U_\infty - U_{y=0.5\delta})$ , which is similar to Zagarola-Smith scale (Zagarola and Smits 1998). The  $y$  coordinate is scaled by the boundary layer thickness  $\delta$ . At inlet plane the profiles are exactly the same. In downstream direction with the increasing of velocity defect the disappearance of near-wall maximum of streamwise Reynolds stress can be noticed, however with suction the process is more advanced. In both cases the outer maximum of  $u'u'$  develops, however gradually loses its intensity when flow approaching separation, when scaled with  $U_0$ . For very last traverses the maximum moves towards the middle of boundary layer. The much stronger enhancement of the outer peak of  $u'u'$  observed for the flow with suction confirms the increasing dominant role of the outer length scales with the rise of pressure gradient and is different to the observation for canonical zero pressure gradient flows.

It is clear that the turbulence properties differ between equilibrium turbulent boundary layer and the turbulent boundary layer being under the influence of strong adverse pressure gradient, where upstream history of the flow is substantial. In order to elucidate the feature of the present data it was decided to referee to literature data sets. The first is the well-known experimental data of equilibrium APG TBL of Krogstad and Skare (1994) (SK) obtained for  $H = 2.0$  and high Reynolds number  $Re_\theta = 39000$ . The other is DNS data of separated TBL of Gungor et al. (2016) (GMSS) obtained for  $H = 2$  and 2.5 and low  $Re_\theta = 1000$ . Own data are obtained for Reynolds number in the range  $Re_\theta = 6300-32000$ .

The comparison has been performed for mean velocity and streamwise Reynolds stress profiles characterising by the same shape factor  $H \approx 2$  and 2.5. In the legend the local pressure gradient parameter  $\beta$  is also given. In the first case (Figure 6a) irrespective of similar values of  $\beta$  substantial difference in shapes of mean velocity profiles are observed. Especially different from others is the shape of equilibrium SK mean velocity profile. On the other hand, despite the lower Reynolds number the shape of the profile of GMSS is quite similar to suction-off case. The worse convergence is obtained for the  $u'u'$  distributions (Figure 6b). For the present flow with suction the maximum is nearly twice the value of the literature data

and is placed at  $y/\delta \approx 0.2$ , which is due to the high mean shear joined with the rapidly increase of boundary layer thickness. For the case with no suction the maximum amplitude is much smaller and placed much closer to the GMSS data. Moving to the profiles for  $H \approx 2.5$  (Figure 6c and 6d) much better convergence between present data (suction-on) and GMSS data are observed. It can be expected that near the point of detachment the similarity should be even better.

Preliminary data analysis indicates that turbulent boundary layer structure depends not only on the local effects of pressure gradient, but also on the upstream history of the flow. It seems also that the influence of Reynolds number is less important.

## 4 Conclusions

The effects of pressure gradient on non-equilibrium boundary layer being at the verge of separation, with local areas of equilibrium flow was investigated. The emphasis is on the analysis of mean flow statistics i.e. streamwise Reynolds stress and mean velocity profiles. The comparison with external data i.e. one equilibrium and other non-equilibrium was performed.

It has been shown that a small increase in the pressure gradient induced by applied suction on the upper wall causes a high response of the boundary layer on the bottom wall. It results in stronger deformation of mean velocity profiles and faster decay of  $u'u'$  inner peak. Comparative analysis with external data indicates that turbulent boundary layer structure depends very much not only on the local effects of pressure gradient, but also on the upstream history of the flow.

## Acknowledgements

The investigation was supported by National Science Centre under Grant no. UMO-2012/07/B/ST8/03791 and the statutory funds BS/PB 1-103-3010/2011/P.

## References

- Castillo, Luciano, and William K George. 2001. "Similarity Analysis for Turbulent Boundary Layer with Pressure Gradient: Outer Flow." *AIAA Journal* 39(1): 41-47.
- Castillo, Luciano, Xia Wang, and William K George. 2004. "Separation Criterion for Turbulent Boundary Layers Via Similarity Analysis." *Journal of Fluids Engineering* 126(3): 297.
- Cherry, N. J., R. Hillier, and M. E. M. P. Latour. 1984. "Unsteady Measurements in a Separated and Reattaching Flow." *Journal of Fluid Mechanics* 144(-1): 13-46.
- Elsberry, K., J. Loeffler, M. D. Zhou, and I. Wygnanski. 2000. "An Experimental Study of a Boundary Layer That Is Maintained on the Verge of Separation." *Journal of Fluid Mechanics* 423(-1): 227-61.
- Gungor, Ayse G, Y. Maciel, M. P. Simens, and J. Soria. 2016. "Scaling and Statistics of Large-Defect Adverse Pressure Gradient Turbulent Boundary Layers." *International Journal of Heat and Fluid Flow* 59: 109-24.
- Gungor, Ayse G, Yvan Maciel, Mark P Simens, and Julio Soria. 2014. "Analysis of a Turbulent Boundary Layer Subjected to a Strong Adverse Pressure Gradient." *Journal of Physics: Conference Series* 506: 012007.

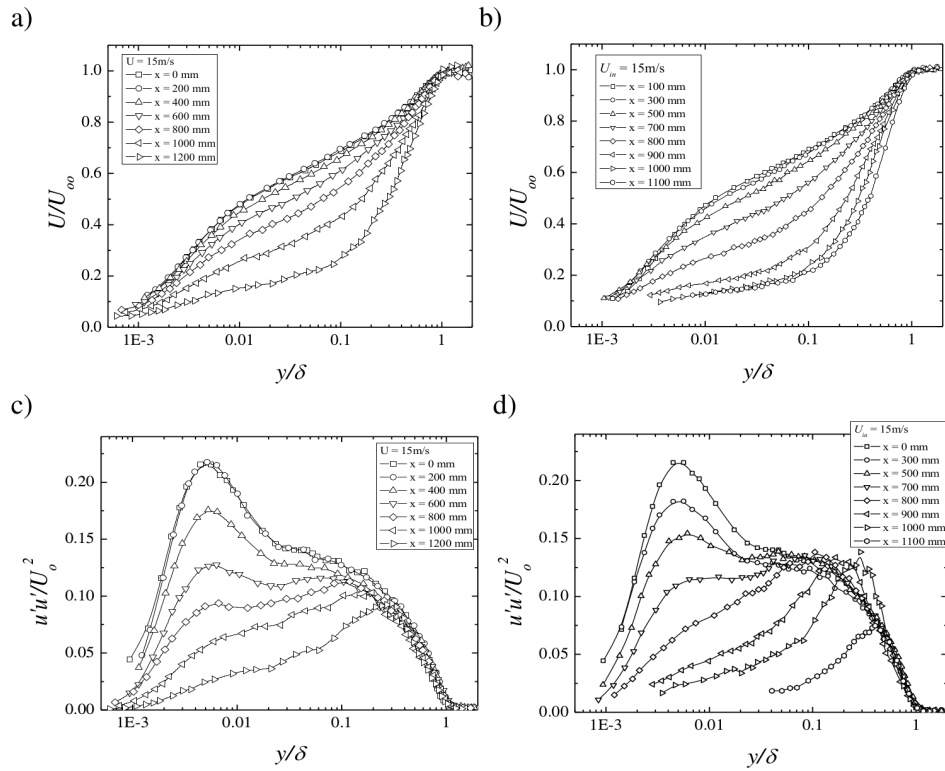


Figure 5: Mean velocity profiles; a) suction - off; b) suction - active, and streamwise Reynolds stresses for 15 m/s c) suction - off; b) and d) suction - active

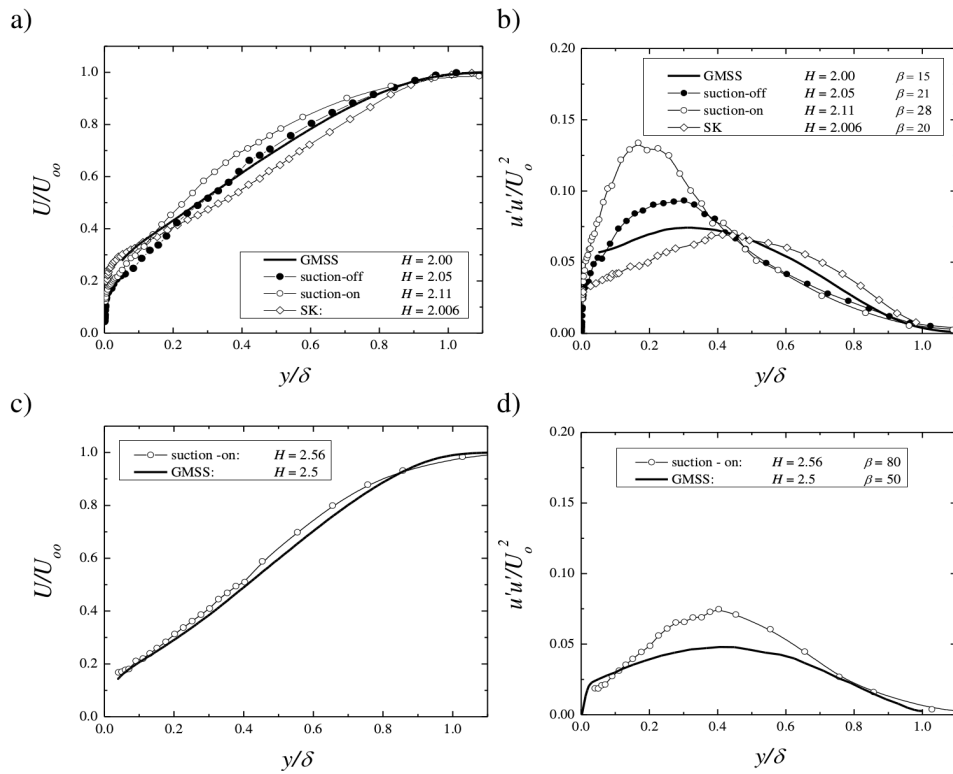


Figure 6: Mean velocity profiles for  $H \approx 2$  (a) and  $H \approx 2.5$  (c), and streamwise Reynolds stresses for  $H \approx 2$  (b) and  $H \approx 2.5$  (d)

- Krogstad, Per-Åge, and Egil Skare. 1995. "Influence of a Strong Adverse Pressure Gradient on the Turbulent Structure in a Boundary Layer." *Physics of Fluids* 7(8): 2014-24.
- Ligrani, P.M., and Peter Bradshaw. 1987. "Spatial Resolution and Measurement of Turbulence in the Viscous Sublayer Using Subminiature Hot-Wire Probes." *Experiments in Fluids* 5: 407-17.
- Sandborn, V. A., and S. J. Kline. 1961. "Flow Models in Boundary-Layer Stall Inception." *Journal of Fluids Engineering* 83(3): 317-27.
- Skote, M, and D S Henningson. 1998. "Direct Numerical Simulation of Self-Similar Turbulent Boundary Layers in Adverse Pressure Gradients." *Flow, Turbulence and Combustion* 60: 47-85.
- Zagarola, Mark V., and Alexander J. Smits. 1998. "Mean-Flow Scaling of Turbulent Pipe Flow." *Journal of Fluid Mechanics* 373: 33-79.

# ASSESSMENT OF TURBULENT BOUNDARY LAYERS ON A NACA4412 WING SECTION AT MODERATE $Re$

R. Vinuesa<sup>1</sup>, S. M. Hosseini<sup>1</sup>, A. Hanifi<sup>1,2</sup>, D. S. Henningson<sup>1</sup> and P. Schlatter<sup>1</sup>

<sup>1</sup>Linné FLOW Centre, KTH Mechanics and Swedish e-Science Research Centre (SeRC), Stockholm, Sweden

<sup>2</sup>Swedish Defence Research Agency, FOI, Stockholm, Sweden

rvinuesa@mech.kth.se

## Abstract

The results of a DNS of the flow around a wing section represented by a NACA4412 profile, with  $Re_c = 400,000$  and  $5^\circ$  angle of attack, are presented in this study. The high-order spectral element code Nek5000 was used for the computations. The Clauser pressure-gradient parameter  $\beta$  ranges from  $\simeq 0$  and 85 on the suction side, and the maximum  $Re_\theta$  and  $Re_\tau$  values are around 2,800 and 373, respectively. Comparisons between the suction side with ZPG TBL data show a more prominent wake, a steeper logarithmic region and lower velocities in the buffer region. The APG also leads to a progressively increasing value of the inner peak in the tangential velocity fluctuations, as well as the development of an outer peak, which is also observed in the other components of the Reynolds stress tensor. Other effects of strong APGs are increased production and dissipation profiles across the boundary layer, together with enhanced viscous diffusion and velocity-pressure-gradient correlation values near the wall. All these effects are connected to the fact that the large-scale motions of the flow become energized due to the APG, as apparent from spanwise premultiplied power spectral density plots.

## 1 Introduction

Despite their great technological importance, the turbulent boundary layers developing around wing sections have not been characterized in detail in the available literature. One of the most remarkable studies in this regard is the work by Coles (1956) 60 years ago, where he, among other aspects, analyzed several sets of measurements on airfoils approaching separation, and he introduced the concept of the “law of the wake”. Progressive increase in computer power has allowed in the recent years to perform numerical simulations on relatively complex geometries, which have shed some light on the physics taking place on wing sections. Some examples are the direct numerical simulations (DNSs) of Jones *et al.* (2008) and the large-eddy simulations (LESs) of Alferez *et al.* (2013), at Reynolds numbers based on freestream velocity  $U_\infty$  and wing chord length  $c$  of  $Re_c = 50,000$  and  $100,000$ , respectively. Nevertheless, these studies focus on laminar separation bubbles (LSBs), and therefore do not allow to characterize the development of the turbulent boundary layers throughout the suction and pressure sides of the wing (which will be denoted as  $ss$  and  $ps$ , respectively).

In the present study we report the results of a DNS of the flow around a NACA4412 wing section, at an unprecedented  $Re_c = 400,000$ , with  $5^\circ$  angle of attack. Although incipient separation is observed beyond  $x_{ss}/c \simeq 0.9$  ( $x$  being the chord-wise coordinate), the

mean skin friction coefficient  $C_f$  is always positive, which indicates that the mean flow is attached throughout the whole wing. Note that  $C_f = 2(u_\tau/U_e)^2$ , where  $U_e$  is the local velocity at the boundary-layer edge and  $u_\tau$  is the friction velocity. Therefore the emphasis of this work is on the streamwise development of the turbulent boundary layers developing around the wing, and the effect of the pressure gradient on the most relevant turbulent features.

## 2 Numerical method

In order to properly simulate the complex multi-scale character of turbulence, it is essential to use high-order numerical methods. The DNS described in this work was carried out with the code Nek5000 (Fischer *et al.*, 2008), which is based on the spectral element method, and Lagrange interpolants of polynomial order  $N = 11$  were considered for the spatial discretization. The computational domain has chord-wise and vertical lengths  $L_x = 6.2c$  and  $L_y = 2c$  respectively, and the periodic spanwise direction has a length of  $L_z = 0.1c$ . As can be observed in Figure 1, we considered a C-mesh; a Dirichlet boundary condition extracted from a previous RANS simulation was imposed in all the boundaries except at the outflow, where the natural stress-free condition was used. A total of 1.85 million spectral elements was employed to discretize the domain, which amounts to around 3.2 billion grid points. Moreover, the boundary layers developing over the suction and pressure sides of the wing were tripped using the volume-force approach proposed by Schlatter and Örlü (2012), at a chord-wise distance of  $x/c = 0.1$  from the wing leading edge. The mesh was designed in order to satisfy the condition  $h \equiv (\Delta x \cdot \Delta y \cdot \Delta z)^{1/3} < 5\eta$  everywhere in the domain, where  $\eta = (\nu^3/\varepsilon)^{1/4}$  is the Kolmogorov scale and  $\varepsilon$  is the local isotropic dissipation, so that the mesh is fine enough to capture the smallest turbulent scales. This can be observed in the level of detail obtained even in the near-wall region in Figure 1. A comprehensive description of the setup can be found in the work by Hosseini *et al.* (2016).

## 3 Turbulence statistics

In order to compute complete turbulence statistics, the simulation was run for a total of 10 flow-over times, which correspond to at least 12 eddy-turnover times (defined as  $\delta_{99}/u_\tau$ , where  $\delta_{99}$  is the 99% boundary layer thickness) throughout the whole wing except for  $x_{ss}/c > 0.9$ . Note that this region is subjected to a very strong adverse pressure gradient (APG), and therefore the tur-

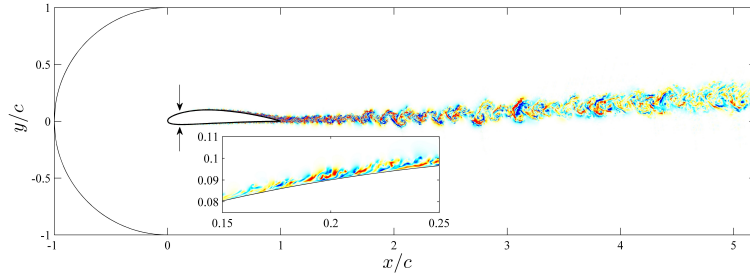


Figure 1: Two-dimensional slice of the computational domain showing with arrows the locations where the flow is tripped. Instantaneous spanwise velocity is also shown, where blue and red indicate positive and negative values, respectively. The insert shows a detailed view of the flow on the suction side of the wing, and the spanwise velocities range from  $-0.52$  to  $0.52$

bulent scales are significantly larger than in the rest of the wing. The boundary layers developing around the wing were characterized at a total of 80 profiles on both sides, projected on the directions tangential ( $t$ ) and normal ( $n$ ) to the wing surface, and the magnitude of the pressure gradient was quantified in terms of the Clauser pressure-gradient parameter  $\beta = \delta^*/\tau_w dP_e/dx_t$ . Note that  $\delta^*$  is the displacement thickness,  $P_e$  is the pressure at the boundary-layer edge and  $x_t$  is the coordinate tangential to the wing surface. Figure 2 shows mean flow, Reynolds-stress tensor components and turbulent kinetic energy (TKE) budgets at  $x_{ss}/c = 0.8$  and  $0.9$ , respectively. The boundary layer is subjected to a strong APG at  $x_{ss}/c = 0.8$ , where the value of  $\beta$  is 4.1, and as can be observed in Figure 2 (top) the APG leads to a more prominent wake region (as also reported by Monty *et al.* (2011) and Vinuesa *et al.* (2014)), a steeper incipient log region, and reduced velocities in the buffer layer compared with the DNS of ZPG boundary layer by Schlatter and Örlü (2010). Table 1 shows several mean flow parameters of the boundary layer at  $x_{ss}/c = 0.8$  compared with the ZPG at approximately matching friction Reynolds number  $Re_\tau = \delta_{99}u_\tau/\nu$  (where  $\nu$  is the fluid kinematic viscosity). Note that the difficulties of determining the boundary-layer thickness in pressure-gradient TBLs were discussed by Vinuesa *et al.* (2016), and their method was considered in the present study to calculate  $\delta_{99}$ . The APG effectively lifts up the boundary layer and increases its thickness, which leads to a larger shape factor  $H = \delta^*/\theta$  (where  $\theta$  is the momentum thickness), and also to a reduced skin friction coefficient. The lower value of the von Kármán coefficient  $\kappa$  is connected with a steeper log law, and the larger wake parameter  $\Pi$  shows the strong impact on the wake region. As shown by Monty *et al.* (2011), the APG energizes the large-scale structures in the flow, which have a strong interaction with the outer flow (thus the impact on the wake region). These large-scale motions are usually wall-attached eddies, which leave their footprint at the wall and therefore significantly affect the overlap and buffer layers. Additional insight on the effect of pressure gradients on the turbulent boundary layers developing around the wing can be achieved by analyzing the components of the Reynolds-stress tensor also shown in Figure 2. The impact of the APG can clearly be observed at  $x_{ss}/c = 0.8$  on the tangential velocity fluctuations  $u_t^2$ : the inner peak is increased, and the effect on the outer region is quite noticeable, as also observed by Skåre and Krogstad (1994), Marusic and Perry (1995) and Monty *et al.* (2011). This is associated with the largest and most energetic scales in the flow interact-

ing with the APG, as is also noticeable from the larger values of  $w^2$  in the outer region. Note that the tangential velocity fluctuation profile starts to develop an outer peak, as also observed by Monty *et al.* (2011), which is connected to the fact that the structures in the outer flow are more energetic due to the effect of the APG. It is also interesting to note that the effect on the wall-normal velocity fluctuations  $v_n^2$  and the Reynolds shear stress is also significant, although slightly less pronounced. Figure ?? (top) also shows the TKE budget at  $x_{ss}/c = 0.8$ , and it is interesting to note that the effect of the pressure gradient is noticeable in all the terms. More specifically, the APG leads to an increased inner peak in the production profile (around 70% larger than the one in the ZPG boundary layer), which is connected to the increased peak in tangential velocity fluctuations, as well as an incipient peak in the outer region. The effect on the dissipation is significant in the near-wall region, which shows enhanced dissipation levels (around 90% larger than the ZPG TBL), although the discrepancy with respect to the ZPG case progressively diminishes as the outer region is approached. Interestingly, the viscous diffusion is also increased in the near-wall region as a consequence of the APG, and when it becomes negative it also exhibits larger values than the ZPG TBL, in this case to balance the rapidly growing production. Beyond  $y_n^+ \simeq 10$  the APG profile converges to the one from the ZPG. Therefore the interactions between the large-scale motions in the outer region have a manifestation in the redistribution of TKE terms close to the wall, as can also be observed in the increased values of the velocity-pressure-gradient correlation for  $y_n^+ < 10$ , which is positive, and also balances the increased dissipation.

The TBL on the suction side of the wing is subjected to a strong APG with  $\beta \simeq 14.1$  at  $x_{ss}/c = 0.9$ , and its statistics are shown in Figure 2 (bottom). The inner-scaled mean flow is shown on the left panel of Figure 2, and the most relevant flow parameters are summarized in Table 1. The effects observed in the moderate-APG case at  $x_{ss}/c = 0.8$  are even more noticeable in this case, where the impact on the wake parameter, incipient log layer and buffer region is even larger. Similar effects on the mean flow can be observed in the experimental study by Skåre and Krogstad (1994) with a comparably large  $\beta$  value of 19.9, at  $Re_\theta$  up to 39,120. Regarding the Reynolds-stress tensor components, the first interesting observation is the fact that the inner peak in the tangential velocity fluctuation profile exceeds the one from the ZPG by a factor of around 2, and the outer peak is

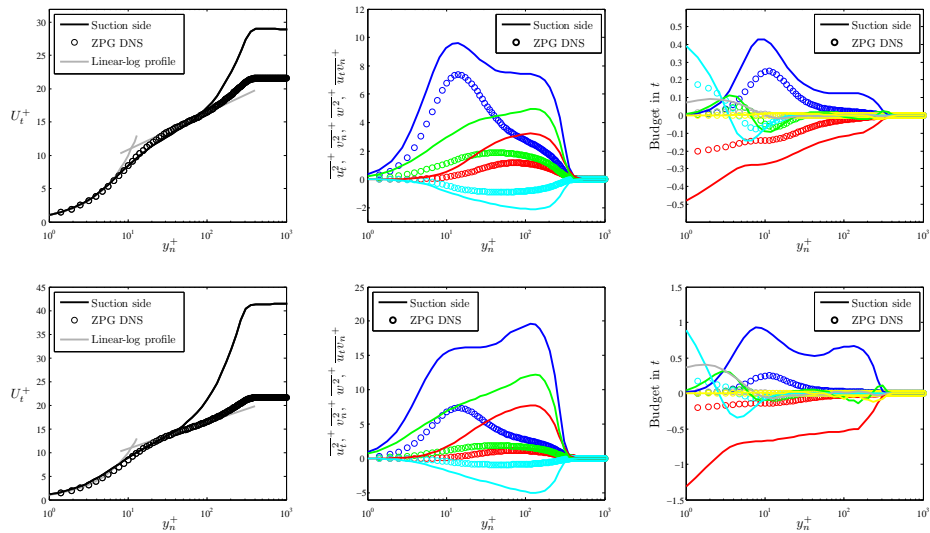


Figure 2: (Left panel) Inner-scaled mean flow (with reference low- $Re$  values  $\kappa = 0.41$  and  $B = 5.2$ ), (middle panel) inner-scaled Reynolds-stress tensor components and (right panel) TKE budget scaled by  $u_\tau^4/\nu$ . Reynolds stresses are represented as: — tangential, — wall-normal and — spanwise velocity fluctuations, and — Reynolds shear stress. Budget terms are represented as follows: — Production, — Dissipation, — Turbulent transport, — Viscous diffusion, — Velocity-pressure-gradient correlation and — Convection. Data extracted at (top line)  $x_{ss}/c = 0.8$  and (bottom line)  $x_{ss}/c = 0.9$ , and compared with the ZPG data by Schlatter and Örlü (2010)

around 33% larger than the inner one. The other components of the Reynolds-stress tensor also exhibit significantly larger values in the outer region compared with the ZPG case, which again shows the effect of the APG energizing the large-scale motions of the flow, and in particular the significantly modified Reynolds shear stress shows the very different momentum distribution mechanisms across the boundary layer under the effect of the APG. Although Skåre and Krogstad (1994) did not take measurements close to the wall, they also characterized the significantly large peaks in the outer region of the various components of Reynolds stress tensor. In this sense, it can be argued that APG TBLs exhibit features of higher Reynolds number boundary layers, as also pointed out by Harun *et al.* (2013), who compared the features of TBLs subjected to APG, ZPG and FPG conditions, and suggested the possibility of connecting high  $Re$  effects in ZPG boundary layers with the effect of APGs. In this context, Hutchins and Marusic (2007) showed how the energy of the turbulent structures in the log region increases with  $Re$ , becoming comparable with the energy in the near-wall region. This was also observed in the experiments by Vallikivi *et al.* (2015) on pressurized ZPG boundary layers up to  $Re_\theta \simeq 223 \times 10^3$ , which start to exhibit a prominent outer peak in the streamwise velocity fluctuation profile, of magnitude comparable to the one of the inner peak. However, a proper assessment of these effects would require investigations of numerical and experimental nature at much higher Reynolds numbers, in order to properly isolate Reynolds number and pressure gradient effects. Regarding the TKE budget on the right panel, both production and dissipation profiles exceed by at least a factor of 4 the ones of the ZPG throughout the whole boundary layer. It is also remarkable the emergence of an outer peak in the production profile, which is around 40% lower than the inner production peak. This phenomenon was also observed by Skåre and Krogstad (1994) in their experimental boundary layer with  $\beta \simeq 19.9$  and  $Re_\theta \simeq 39, 120$ , although in

their case the magnitude of the outer peak was almost as large as the one from the inner peak, and they found it farther away from the wall: at  $y/\delta \simeq 0.45$ , whereas in our case it is located at  $y/\delta_{99} \simeq 0.35$ . It can be argued that the discrepancy in magnitude and location of this outer peak is caused both by APG strength and Reynolds-number effects. Skåre and Krogstad (1994) also showed that there was considerable diffusion of turbulent kinetic energy from the central part of the boundary layer towards the wall, which was produced by the emergence of this outer peak. Since in our case the outer peak of the streamwise velocity fluctuations is larger than the inner peak, but in the production profile the outer peak is smaller, it could be conjectured that the APG effectively energizes the large-scale motions of the flow, and eventually these more energetic structures become a part of the production mechanisms characteristic of wall-bounded turbulence. The high levels of dissipation observed in our case also far from the wall were also reported in the experiment by Skåre and Krogstad (1994), and in particular they also documented the presence of the inflection point in the dissipation profile at roughly the same wall-normal location as the outer peak of the production. Other relevant terms significantly affected by the APG are the viscous diffusion, which again shows larger values very close to the wall to balance the increased dissipation, and in this case changes sign at an even lower value of  $y_n^+$ :  $\simeq 2.5$ . The velocity-pressure-gradient correlation also shows significantly increased values close to the wall compared with the ZPG case, but as in the  $\beta \simeq 4.1$  APG, for  $y_n^+ > 10$  both the viscous diffusion and the velocity-pressure-gradient profiles approximately converge to the ZPG ones. In addition to the increased maxima of turbulent transport and convection observed close to the boundary-layer edge, this strong APG case exhibits a relative minimum of turbulent transport at approximately the same location as the outer production peak, which is interesting because beyond this location this term changes sign. This suggests that the very

Parameter	$x_{ss}/c = 0.8$	$x_{ss}/c = 0.9$	ZPG DNS
$Re_\tau$	373	328	359
$\beta$	4.1	14.1	$\simeq 0$
$Re_\theta$	1,722	2,255	1,007
$H$	1.74	2.03	1.45
$C_f$	$2.4 \times 10^{-3}$	$1.2 \times 10^{-3}$	$4.3 \times 10^{-3}$
$\kappa$	0.33	0.23	0.41
$B$	2.08	-2.12	4.87
$\Pi$	1.35	1.83	0.37

Table 1: Boundary-layer parameters at  $x_{ss}/c = 0.8$  and  $0.9$ , compared with ZPG results by Schlatter and Örlü (2010)

strong production in the outer region leads to additional negative turbulent transport to balance, together with the dissipation, this locally increased production level.

## 4 Spectral analysis

In order to further assess the characteristics of the boundary layers developing around the wing section, their energy distribution is studied through the analysis of the inner-scaled spanwise premultiplied power spectral density of the tangential velocity  $k_z \Phi_{u_t u_t}^+$ , shown at  $x_{ss}/c = 0.8$  and  $0.9$  in Figure 3. The first interesting feature of these spectra is the fact that they exhibit the so-called inner-peak of spectral density, at a wall-normal distance of around  $y_n^+ \simeq 12$ , and for wavelengths of around  $\lambda_z^+ \simeq 120$ . This was also observed in the LES of ZPG boundary layer by Eitel-Amor *et al.* (2014) up to a much higher  $Re_\theta = 8,300$ , and is a manifestation of the inner peak of the tangential velocity fluctuations discussed in §3. In fact, the value of this inner peak is also highly affected by the pressure gradient: at  $x_{ss}/c = 0.8$  it takes a value of around 5, which is larger than the value of approximately 4 in ZPG TBLs, and at  $x_{ss}/c = 0.9$  it rises up to 6. This behavior strongly resembles the one of the tangential velocity fluctuations, and highlights the connection between the coherent structures in the boundary layer and the turbulence statistics. Moreover, the wavelength  $\lambda_z^+ \simeq 120$  corresponds to the characteristic streak spacing in wall-bounded turbulence, as shown for instance by Lin *et al.* (2008). In this context, it is also interesting to note that the domain is sufficiently wide to capture the contributions of all the relevant turbulent scales in the boundary layer, even in the strongly decelerated and very thick boundary layer conditions found at  $x_{ss}/c = 0.9$ .

Regarding the spectra in the outer region of the boundary layer, it is first interesting to note the emergence of an outer peak with a value of inner-scaled power spectral density of around 4 at  $x_{ss}/c = 0.8$ . The very strong APG found at  $x_{ss}/c = 0.9$  leads to a power spectral density level on the outer region larger than the one in the inner region of the boundary layer, with an inner-scaled value of around 8. The connection with the streamwise turbulence intensity profiles is again clear in the development of the outer region, since at  $x_{ss}/c = 0.8$  the outer peak is also slightly below the inner one (but of the same magnitude as the inner peak in a ZPG boundary layer), and at  $x_{ss}/c = 0.9$  also in the  $u_t^2$  profile the outer peak is larger than the inner one. Therefore, the progressively stronger APG energizes the large-scale motions of the flow, which on the other hand have a footprint in the near-wall region responsible for the increase of energy in the buffer

layer. The emergence of this outer spectral peak was also observed by Eitel-Amor *et al.* (2014) in their ZPG simulations at much higher Reynolds numbers, with an incipient outer peak at  $Re_\theta \simeq 4,400$  which started to become more noticeable at around  $Re_\theta \simeq 8,300$ . Note that in their case the spectral density level in the outer region was significantly lower than the one in the inner region, and therefore much higher Reynolds numbers would be necessary in a ZPG boundary layer in order to reach similar outer energy levels. On the other hand, Eitel-Amor *et al.* (2014) observed the emergence of the outer spectral peak at around  $\lambda_z \simeq 0.8\delta_{99}$ , whereas the results in Figure 3 show that in the suction side of the wing the outer peak emerges at around  $\lambda_z \simeq 0.65\delta_{99}$ . Due to the significantly lower Reynolds numbers present in the wing, it is difficult to assess whether this difference in the structure of the outer region is due to a fundamentally different mechanism in the energizing process of the large-scale motions from APGs and high- $Re$  ZPGs, or whether this is due to low- $Re$  effects. In any case, and as also noted by Harun *et al.* (2013), the effect of the pressure gradient on the large-scale motions in the flow has features in common with the effect of  $Re$  in ZPG boundary layers, and therefore further investigation at higher Reynolds numbers would be required to separate pressure-gradient and Reynolds-number effects.

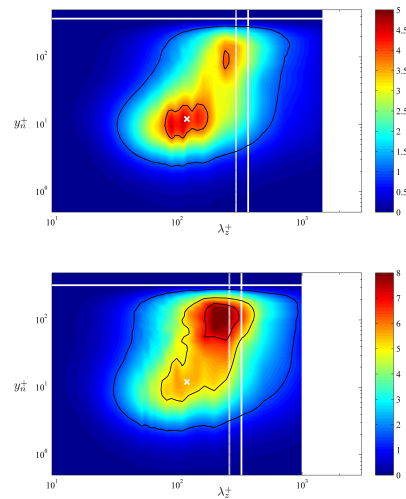


Figure 3: Inner-scaled spanwise premultiplied power spectral density of the tangential velocity  $k_z \Phi_{u_t u_t}^+ / u_\tau^2$ . Spectra calculated at (top)  $x_{ss}/c = 0.8$  and (bottom)  $x_{ss}/c = 0.9$ . White crosses indicate the location  $y_n^+ = 12$ ,  $\lambda_z^+ = 120$ , white solid lines denote the inner-scaled boundary layer thickness  $\delta_{99}^+$ , and white dashed lines show the position  $\lambda_z \simeq 0.8\delta_{99}$ . Black solid lines indicate contour levels of 1 and 3.8 at  $x_{ss}/c = 0.8$ , and 1.5, 5 and 7 at  $x_{ss}/c = 0.9$

## 5 Conclusions

In the present study we perform a DNS of the flow around a wing section represented by a NACA4412 profile, with  $Re_c = 400,000$  and  $5^\circ$  angle of attack. The high-order spectral element code Nek5000 is used for the computations, which are carried out with 16,384 cores on the Cray XC40 system “Beskow” at KTH, Stockholm. The Clauser pressure-gradient parameter  $\beta$  ranges from  $\simeq 0$  and 85 on the suction side, and thus this TBL is sub-

jected to a progressively stronger APG. The first effect of the APG on the mean flow is the more prominent wake, reflected in a larger  $U_e^+$  and a larger wake parameter  $\Pi$ . In addition to this, the APG produces a steeper logarithmic region, which is characterized by lower values of the von Kármán coefficient  $\kappa$  and  $B$ , as well as decreased velocities in the buffer region. These effects, which were also observed by Monty *et al.* (2011) and Vinuesa *et al.* (2014), are due to the fact that the APG energizes the largest scales in the flow, which become shorter and more elongated, and have their footprint in their near-wall region. Also, these manifestations of the APG become more evident as  $\beta$  increases. Moreover, comparisons of the Reynolds-stress tensor showed a progressive increase in the value of the inner peak of the streamwise turbulence intensity profile, as well as the development of an outer peak which in the strong APG case ( $\beta \simeq 14.1$ ) exceeds the magnitude of the inner peak. Note that the development of a more energetic outer region with increasing  $\beta$  is also observed in the wall-normal and spanwise fluctuation profiles, as well as in the Reynolds shear stress. Comparison of the TKE budgets also shows the different energy distribution across the boundary layer when an APG is present, with increased production and dissipation profiles throughout the whole boundary layer. The emergence of an incipient outer peak in the production profile is observed at  $\beta \simeq 14.1$ , phenomenon which was also reported by Skåre and Krogstad (1994). The increased dissipation leads to larger values of the viscous diffusion and the velocity-pressure-gradient correlation near the wall in order to balance the budget.

Analysis of the inner-scaled premultiplied spanwise spectra showed the presence of the inner spectral peak at around  $y_n^+ \simeq 12$  and  $\lambda_z^+ \simeq 120$ , in agreement with the observations by Eitel-Amor *et al.* (2014) in ZPG TBLs at higher  $Re_\theta$  up to 8,300. As in the inner peak of  $\overline{u_i^2}^+$ , the spectral near-wall peak increases with the magnitude of the APG, as a consequence of the energizing process of the large structures in the flow, which have their footprint close to the wall. Also as a consequence of this energizing process, an outer spectral peak emerges at strong APGs with  $\beta \simeq 4.1$ , which is responsible for the development of larger outer region values in all the components of the Reynolds stress tensor. This spectral outer peak is observed at wavelengths of around  $\lambda_z \simeq 0.65\delta_{99}$ , closer to the wall than the outer peak observed at  $Re_\theta \simeq 8,300$  by Eitel-Amor *et al.* (2014) in the ZPG case, with  $\lambda_z \simeq 0.8\delta_{99}$ . At this point it is not possible to state whether this difference arises from low- $Re$  effects, or from a mechanism of energy transfer to the larger scales fundamentally different between high- $Re$  at ZPG and the effect of the APG.

Future studies at higher Reynolds numbers will be aimed at further assessing the connections between the effect of APGs on the large-scale motions in the flow and the effect of  $Re$  in ZPG boundary layers, in order to separate pressure-gradient and Reynolds-number effects.

## Acknowledgments

RV and PS acknowledge financial support from the Swedish Research Council (VR) and the Knut and Alice Wallenberg Foundation. The simulations were performed on resources provided by the Swedish National Infrastructure for Computing (SNIC) at the Center for Parallel Computers (PDC), in KTH, Stockholm.

## References

- Coles, D. (1956), The law of the wake in the turbulent boundary layer, *J. Fluid Mech.*, Vol. 1, pp. 191–226.
- Jones, L. E., Sandberg, R. D. and Sandham, N. D. (2008), Direct numerical simulations of forced and unforced separation bubbles on an airfoil at incidence, *J. Fluid Mech.*, Vol. 602, pp. 175–207.
- Alferez, N., Mary, I. and Lamballais, E. (2013), Study of stall development around an airfoil by means of high fidelity large eddy simulation, *Flow Turb. Comb.*, Vol. 91, pp. 623–641.
- Fischer, P. F., Lottes, J. W. and Kerkemeier, S. G. (2008), NEK5000: Open source spectral element CFD solver. Available at: <http://nek5000.mcs.anl.gov>.
- Schlatter, P. and Örlü, R. (2012), Turbulent boundary layers at moderate Reynolds numbers: inflow length and tripping effects, *J. Fluid Mech.*, Vol. 710, pp. 5–34.
- Hosseini, S. M., Vinuesa, R., Schlatter, P., Hanifi, A. and Henningson, D. S. (2016), Direct numerical simulation of the flow around a wing section at moderate Reynolds number, *Int. J. Heat Fluid Flow*, doi:10.1016/j.ijheatfluidflow.2016.02.001
- Monty, J., Harun, Z. and Marusic, I. (2011), A parametric study of adverse pressure gradient turbulent boundary layers, *Int. J. Heat Fluid Flow*, Vol. 32, pp. 575–585.
- Vinuesa, R., Rozier, P. H., Schlatter, P. and Nagib, H. M. (2014), Experiments and computations of localized pressure gradients with different history effects, *AIAA J.*, Vol. 52, pp. 368–384.
- Schlatter, P. and Örlü, R. (2010), Assessment of direct numerical simulation data of turbulent boundary layers, *J. Fluid Mech.*, Vol. 659, pp. 116–126.
- Vinuesa, R., Bobke, A., Örlü, R. and Schlatter, P. (2016), On determining characteristic length scales in pressure-gradient turbulent boundary layers, *Phys. Fluids*, Vol. 28, pp. 055101.
- Skåre, P. E. and Krogstad, P.-Å. (1994), A turbulent equilibrium boundary layer near separation, *J. Fluid Mech.*, Vol. 272, pp. 319–348.
- Harun, Z., Monty, J. P., Mathis, R. and Marusic, I. (2013), Pressure gradient effects on the large-scale structure of turbulent boundary layers, *J. Fluid Mech.*, Vol. 715, pp. 477–498.
- Hutchins, N. and Marusic, I. (2007), Large-scale influences in near-wall turbulence, *Phil. Trans. R. Soc. A*, Vol. 365, pp. 647–664.
- Vallikivi, M., Hultmark, M. and Smits, A. J. (2015), Turbulent boundary layer statistics at very high Reynolds number, *J. Fluid Mech.*, Vol. 779, pp. 371–389.
- Eitel-Amor, G., Örlü, R. and Schlatter, P. (2014), Simulation and validation of a spatially evolving turbulent boundary layer up to  $Re_\theta = 8300$ , *Int. J. Heat Fluid Flow*, Vol. 47, pp. 57–69.
- Lin, J., Laval, J. P., Foucaut, J. M. and Stanislas, M. (2008), Quantitative characterization of coherent structures in the buffer layer of near-wall turbulence. Part 1: Streaks, *Exp. Fluids*, Vol. 45, pp. 999–1013.

# REVISITING HOT-WIRE ANEMOMETRY CLOSE TO SOLID WALLS

Y. Ikeya<sup>1,2</sup>, R. Örlü<sup>2</sup>, K. Fukagata<sup>1</sup> and P. H. Alfredsson<sup>2</sup>

<sup>1</sup>*Department of Mechanical Engineering, Keio University, Yokohama, Japan*

<sup>2</sup>*Linné FLOW Centre, KTH Mechanics, Stockholm, Sweden*

ramis@mech.kth.se

## Abstract

The present paper deals with the erroneous velocity reading of hot-wire anemometry close to a solid wall caused by additional heat losses examined by means of experiment and numerical simulation. Measurements in both quiescent air and laminar/turbulent-boundary layer confirmed the influences of parameters such as wall conductivity, overheat ratio and probe dimensions on the output voltage (not just the mean value but also its fluctuations). The accompanying two-dimensional numerical simulation indicated its usefulness for qualitative discussion of the problem.

## 1 Introduction

Hot-wire anemometry (HWA) has been the most widely used laboratory method to measure local fluid velocities in experimental fluid mechanics, which enabled the study of turbulent fluctuations quantitatively. Furthermore, it was the only method capable of measuring high frequency and amplitude velocity fluctuations with a high spatial resolution and has been dominant in the experimental field until the development of laser-based techniques such as laser Doppler velocimetry (LDV) and particle image velocimetry (PIV). HWA is therefore prominently in use for acquiring data in wall-bounded turbulent flows.

However, a well-known major drawback in HWA is that a hot-wire probe calibrated in the wall-remote region registers a seemingly higher velocity in the near-wall region, known as the wall-proximity effect. Additional heat losses from the heated sensor to the cooler wall are erroneously read as an increase in velocity as the wire approaches the wall surface. The wall-proximity effect causes a problem especially when the friction velocity, *the* characteristic scale in wall-bounded turbulence, needs to be deduced from the velocity profile in the viscous sub-layer (Örlü et al., 2010).

The aforementioned problem has been investigated in numerous studies in the literature, with many of them concerned with possible correction schemes for the mean velocity and its dependence on operational and geometrical parameters. Generally, it is widely agreed upon that the wall conductivity, overheat ratio, and sensor dimensions have an influence on the erroneous velocity reading, such that:

- Highly conductive materials register larger apparent velocity reading than poorly conductive materials do (see e.g. Polyakov & Shindin, 1978; Bhatia et al., 1982; Durst & Zanoun, 2002).
- Larger length-to-diameter ratio  $l/d$  of the wire results in a larger apparent velocity reading (see e.g. Krishnamoorthy et al., 1985; Chew et al., 1995).

- The larger the overheat ratio is, the larger the apparent velocity reading becomes (see e.g. Krishnamoorthy et al., 1985; Zanoun et al., 2009).

However, the detailed principle of the heat transfer for the hot-wire in the near-wall region including its interaction with the wall material is still not entirely understood. In addition, most of the previous studies, if not all, are concerned with errors in the mean velocity and there is little, if not no, knowledge of the measured turbulence quantities: turbulence intensity and higher-order moments. In light of the recent demands for increased accuracies in determining the friction velocity and/or absolute wall-position (Örlü et al., 2010), the interest in higher-order moments in the near-wall region (Örlü et al., 2016) as well as its wall-limiting quantities, e.g. the fluctuating wall-shear stress (Alfredsson et al, 1988; Örlü & Schlatter, 2011), there is a need to revisit the effect of hot-wire measurements close to solid walls.

The present investigation carries out a systematic parameter study on the misreading of hot-wire anemometry in the near-wall region so that further insight can be provided into this field, which will eventually help researchers to investigate this topic effectively in the future. In particular, measurements under no-flow and flow conditions, in a laminar and a turbulent boundary layer, have been performed by varying the wall material, overheat ratio, and probe dimensions. Furthermore, a numerical investigation is carried out to further study the heat conduction inside the wall material.

## 2 Experimental Part

### 2.1 Natural convection measurements

To study the effect of parameters in the absence of a cross flow, measurements in a specially designed enclosed box were performed. The schematic of the setup is illustrated in figure 1. A probe mounted on a metallic arm can be vertically traversed manually by means of a micrometer. The output voltage of the anemometer was acquired at thirtyfive heights up to a distance of  $y = 2$  mm from the wall. Additionally, the voltage output at  $y = 5$  mm was recorded as  $E_0$ , where the effect of the wall is considered to be negligible.

The effect of thermal conductivity of the wall was investigated by changing the wall material between aluminum, brass, steel, Plexiglas, and styrofoam. Besides the wall material, the wire length and resistance overheat ratio

$$a_R = \frac{R_w - R_0}{R_0}, \quad (1)$$

were also taken as parameters to see their influence on the voltage reading. Here, the subscript 0 denotes the cold state, i.e. reference state, and  $w$  denotes the heated state, i.e. when the wire is under operation.

## 2.2 Wind-tunnel experiment

HWA measurements were also carried out inside the *Minimum Turbulence Level* (MTL) closed-loop wind tunnel located at the Royal Institute of Technology (KTH) in Stockholm, which has a 7 m long test section and a cross-sectional area of  $0.8 \times 1.2 \text{ m}^2$ .

A probe is mounted on a traversing system above a flat plate as shown in figure 2 and can be controlled from a computer. The flat plate has both aluminum and Plexiglas surfaces at different spanwise positions at the same streamwise location, which were used to investigate the effect of wall conductivity. Furthermore, both laminar and turbulent boundary layers developing on the plate with zero-pressure gradient were considered with momentum-loss thickness Reynolds numbers ( $Re_\theta$ ) of around 400 and 950, respectively. The sampling frequency in this measurement is 20000 Hz and the sampling time is 10 seconds.

Calibration of the probes was carried out in the free-stream and upstream of the flat plate, against a Prandtl tube which was also used to monitor the free-stream velocity in the tunnel. The free-stream velocity is controlled by a computer and the corresponding voltage output from the probe is recorded. The voltage without flow  $E_0$  is also recorded and used for the calibration. In the present study, a 4th-order polynomial was used to relate the top-of-the-bridge voltage to the velocity (see e.g. George et al., 1989).

## 2.3 Experimental results

Results from the measurements on different wall materials in quiescent air are depicted in figure 3a) and show, as expected, the dependency of the wall conductivity on the hot-wire reading (platinum core wire with  $2.5 \mu\text{m}$  diameter and 0.6 mm nominal length operated at an resistance overheat ratio  $a_R = 0.8$ ). In accordance with Durst et al. (2002), large differences can be observed between poorly conducting walls (Plexiglas and styrofoam with heat conductivities of the order of  $10^{-1}$  and  $10^{-2}$

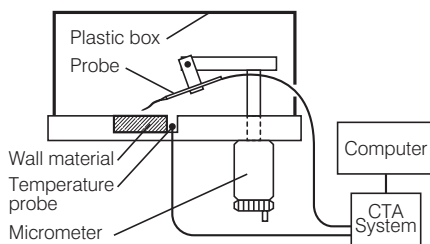


Figure 1: Schematic of the setup for the natural convection measurements.

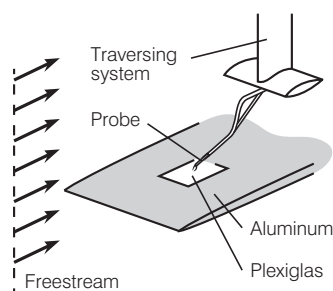


Figure 2: Schematic of the setup for the windtunnel experiments.

W/mK, respectively), while the results from highly conducting materials (such as aluminum, brass and steel, with heat conductivities of the order of  $10^1$ – $10^2$  W/mK) do not vary between each other. The dependency on the overheat ratio for the same probe on the aluminum wall, shown in figure 3b), is also in accordance with the main body of previous studies (Durst & Zanoun, 2002).

Figure 3c) shows the overheat ratio dependency in a laminar boundary layer, in which the overheat ratio exhibits the same effect as for the results in quiescent air; the higher the overheat ratio, the stronger the deviation from the linear profile. In both cases, the effect is however limited to  $y^+ \lesssim 3$ , where the superscript ‘+’ denotes scaling in wall units.

The mean streamwise velocity and root-mean square profiles for a turbulent boundary layer are shown in figure 4a) for two different wall materials (aluminum and Plexiglass) and display no differences in the inner layer of the boundary layer. The marginal differences in the outer layer are due to slightly different conditions of the boundary layers (i.e. slight differences in the Reynolds number as well as probable inhomogeneities in the spanwise direction). One should, however, recall that the accurate determination of the absolute wall position in wall-bounded flows is by no means trivial (see Örlü et al., 2010), and that small difference can easily be “hidden” (due to inaccuracies in the absolute wall position and/or the determined friction velocity by shifting the profiles by less than one inner unit) in a semi-logarithmic plot. If one considers instead the profiles in the diagnostic plot (Alfredsson et al., 2011b) shown in figure 4b), which is independent of the wall position and the friction velocity, differences do appear in the region  $U/U_\infty < 0.25$ ; which corresponds to the viscous sublayer (Alfredsson & Örlü, 2010). As apparent, the measured turbulence intensity (and in turn the related rms value of the fluctuating wall shear stress, i.e.  $\tau_{w,rms}/\tau_w = \lim_{y \rightarrow 0} u_{rms}/U$ ) is reduced for

highly conducting materials. To illuminate this effect further figure 4c) depicts the probability density distribution (PDF) for the streamwise velocity fluctuations in inner scaling. In accordance with Alfredsson et al. (2011a), the PDF contour lines should be parallel to each other in the viscous sublayer, which is observed for the contour lines at higher velocities. The deviation at lower velocities is more apparent for the highly conducting wall material. The aforementioned observations can also be made when considering the effect of the overheat ratio as demonstrated in figure 5.

## 3 Numerical Part

### 3.1 Physical model and boundary conditions

A two-dimensional numerical simulation using OpenFOAM (version 2.2.2) is conducted. In the present study, an infinitely long cylinder parallel to a wall and normal to the flow is employed to represent the hot-wire sensor as shown in figure 6. The entire computational domain is divided into a fluid and solid region. The wire centre is located at  $(x/d, y/d) = (0, 100)$  and the domain spreads in the streamwise direction  $-3000 < x/d < 6000$ . The fluid region is from  $0 < y/d < 5000$  and the solid region is from  $-5000 < y/d < 0$ . The mesh is created with ANSYS ICEM and the domain contains 339,040 points in its fluid region and 197,600 points in the solid region.

A Couette flow is reproduced to simulate the phenomenon of a hot wire located in the viscous sublayer.

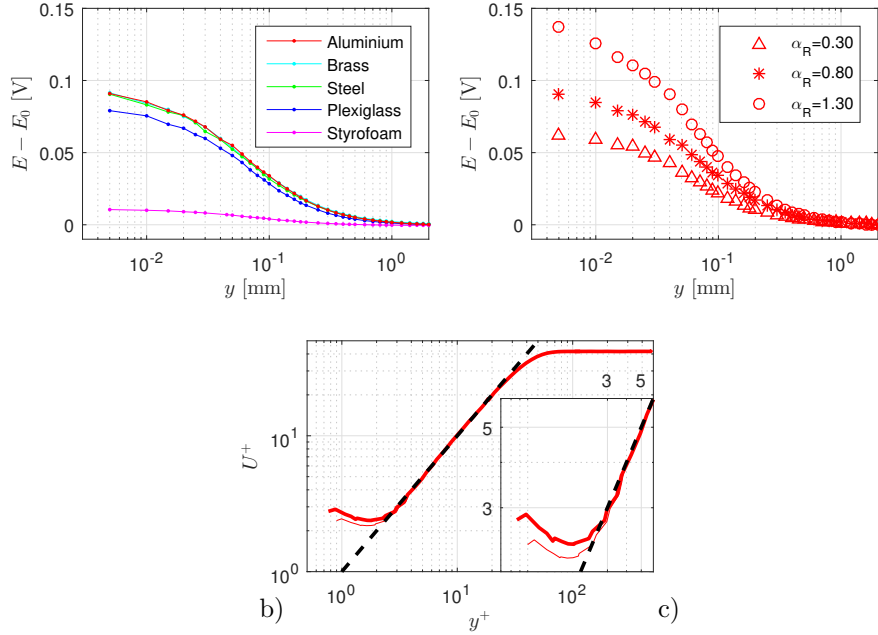


Figure 3: Voltage difference from hot-wire readings in quiescent air a) on different wall materials measured with a resistance overhear ratio  $\alpha_R = 0.8$ , and b) at different resistance overhear ratio measured on aluminum. c): Inner-scaled velocity profile in a laminar boundary layer at  $Re_\theta \approx 400$  on the aluminum wall at a resistance overhear ratio of  $a_R = 0.3$  (thin line) and  $a_R = 0.8$  (thick line). Black dashed line indicates the linear profile  $U^+ = y^+$ .

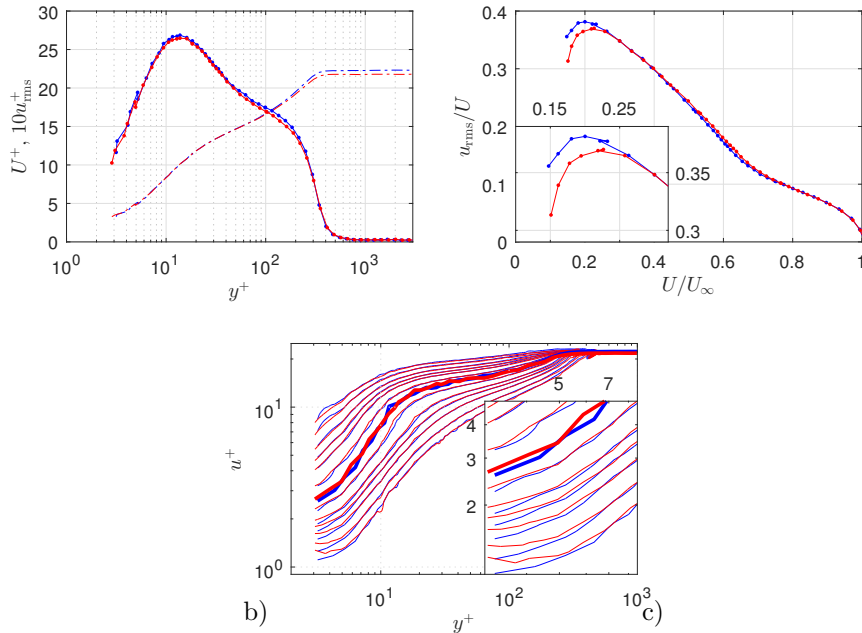


Figure 4: Effect of different wall materials in a turbulent boundary layer at  $Re_\theta \approx 950$  measured with an resistance overhear ratio of  $a_R = 0.8$ : aluminum (red) and Plexiglass (blue). a): Inner-scaled mean and rms profile. b): Diagnostic plot with inset highlighting the viscous sublayer. c): Inner-scaled velocity PDF. Thin lines denote 1, 5, 20, 40, 60 and 90 % of the local maximum (thick line) of the PDF.

In the present calculation, the inner-scaled distance between the wire center and the wall surface is changed by varying the velocity gradient  $S = dU/dy|_{inlet}$ . The temperatures at the inflow and the top moving wall are set to  $T_\infty = 20$  °C while the surface of the cylinder is set to  $T_w = 100$  °C. No-slip conditions are applied at the solid walls and zero-gradient Neumann boundary conditions for velocity and temperature are applied at the outlet. In the solid region, the Dirichlet boundary condition  $T = T_\infty$  was applied at the upstream wall, and adiabatic Neumann conditions were set at the bottom and the downstream boundaries. These two regions were

coupled by means of the temperature continuity and heat flux conservation at the interfaces, namely,

$$T_{fluid} = T_{solid} \quad \text{and} \quad \left( k \frac{\partial T}{\partial y} \right)_{fluid} = \left( k \frac{\partial T}{\partial y} \right)_{solid} . \quad (2)$$

The thermal conductivity of the solid region was set to  $k_{solid} = 205$  and  $0.19$  W/(mK), corresponding to the properties of aluminum and Plexiglas, respectively.

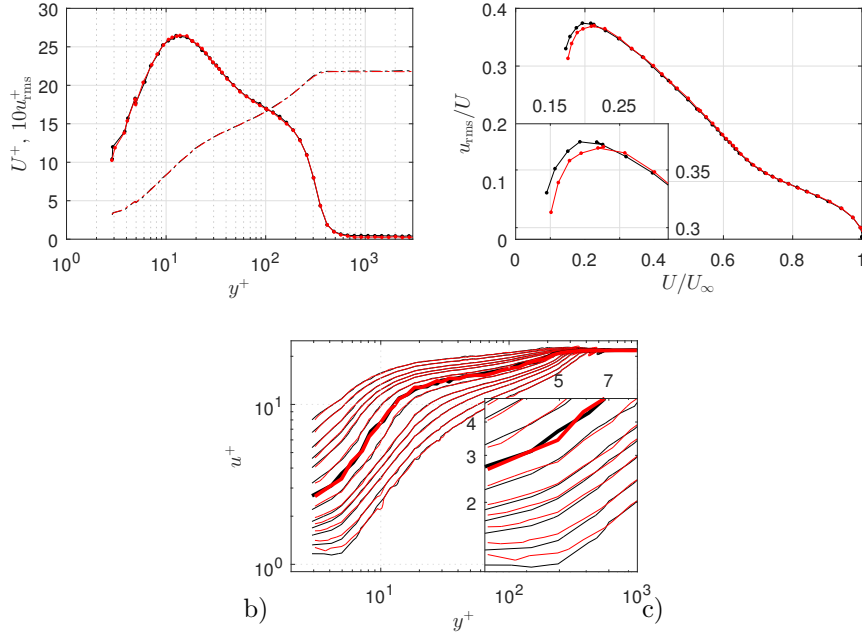


Figure 5: Effect of different resistance overhear ratios  $a_R$  in a turbulent boundary layer at  $Re_\theta \approx 950$  measured on an aluminum wall:  $a_R = 0.3$  (black) and  $a_R = 0.8$  (red). a): Inner-scaled mean and rms profile. b): Diagnostic plot with inset highlighting the viscous sublayer. c): Inner-scaled velocity PDF. Thin lines denote 1, 5, 20, 40, 60 and 90 % of the local maximum (thick line) of the PDF.

### 3.2 Mathematical model

A built-in solver *chtMultiRegionSimpleFoam* capable of calculating conjugate heat transfer in fluid and solid zones is used for the simulation. The governing equations in the fluid region are the conservation of mass, momentum and energy for compressible flow.

$$\frac{\partial(\rho^* U_i^*)}{\partial x_i^*} = 0 \quad (3)$$

$$\frac{\partial(\rho^* U_i^* U_j^*)}{\partial x_i^*} = -\frac{\partial P^*}{\partial x_j^*} + \rho^* g_j^* + \frac{1}{\text{Re}} \frac{\partial}{\partial x_i^*} \left[ \mu^* \left( \frac{\partial U_j^*}{\partial x_i^*} + \frac{\partial U_i^*}{\partial x_j^*} - \frac{2}{3} \frac{\partial U_k^*}{\partial x_k^*} \delta_{ij} \right) \right] \quad (4)$$

$$\frac{\partial(\rho^* h^* U_i^*)}{\partial x_i^*} + \frac{\text{Ec}}{2} \frac{\partial(\rho^* U_i^* U_j^* U_j^*)}{\partial x_i^*} = \frac{1}{\text{RePr}} \frac{\partial}{\partial x_i^*} \left( \frac{k^*}{c_p^*} \frac{\partial h^*}{\partial x_i^*} \right) + \text{Ec} \rho^* U_i^* g_i^* \quad (5)$$

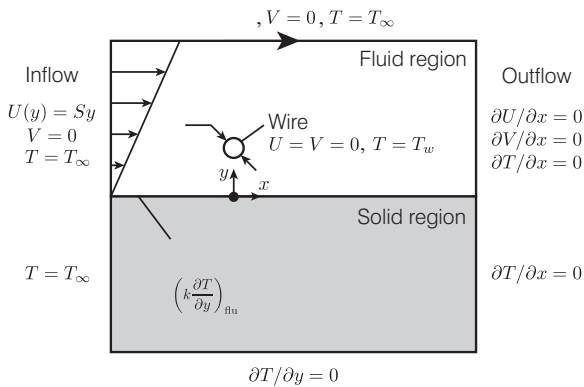


Figure 6: The computational domain with the boundary conditions.

In the solid region, the heat-conduction equation is solved:

$$\frac{k^*}{\rho^* c_p^*} \frac{\partial^2 T^*}{\partial x_i^* \partial x_i^*} = 0.$$

The inlet velocity at the height of the wire centre  $U_w$  and the wire diameter  $d$  are employed to normalize the velocity components and coordinates, respectively, while the temperature is scaled as  $T^* = (T - T_\infty)/(T_w - T_\infty)$ . The thermal physical properties  $\rho^*$ ,  $\mu^*$ ,  $k^*$ , and  $c_p^*$  (density, dynamic viscosity, thermal conductivity and specific heat at constant pressure, respectively) in the equations are chosen as 7th polynomial functions of temperature and normalized by the corresponding values at inflow temperature  $T_\infty$ . The other non-dimensional parameters are the Eckert number, the Prandtl number and the Reynolds number, which are defined as follows:

$$\text{Eckert number : } \text{Ec} = \frac{U_w^2}{c_{p\infty}(T_w - T_\infty)}, \quad (6)$$

$$\text{Prandtl number : } \text{Pr} = \frac{\mu_\infty c_{p\infty}}{k_\infty}, \quad (7)$$

$$\text{Reynolds number : } \text{Re} = \frac{\rho_\infty U_w d}{\mu_\infty}. \quad (8)$$

The heat loss from the wire was evaluated as the mean Nusselt number  $\text{Nu}$  on the wire surface, which is calculated from the local Nusselt number  $\text{Nu}(\theta)$ . The heat flux at a certain point on the surface  $\dot{q}(\theta)$  is calculated as

$$\dot{q}(\theta) = -k(T_w) \left. \frac{\partial T(r, \theta)}{\partial r} \right|_{r=d/2}, \quad (9)$$

where  $r$  and  $\theta$  are the polar coordinates originated at the wire centre. Normalizing  $\dot{q}(\theta)$  with a reference heat flux  $\dot{q}_c = k(T_f)(T_w - T_\infty)/d$  to obtain the local Nusselt number:

$$\text{Nu}(\theta) = \frac{\dot{q}(\theta)}{\dot{q}_c} = -\frac{k(T_w)}{k(T_f)} \left. \frac{\partial T^*(r^*, \theta^*)}{\partial r^*} \right|_{r^*=0.5}, \quad (10)$$

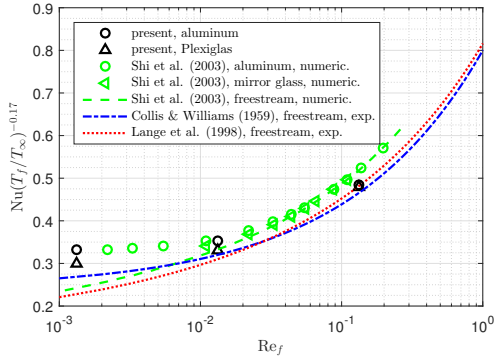


Figure 7: Nusselt number on the wire surface as a function of Reynolds number together with results from previous studies. The result of aluminum/mirror glass wall ( $k^* = 29.6$ ) and the calibration result in a freestream by Shi et al. (2003) are corrected based on their temperature setting of  $T_\infty$  and  $T_w$ .

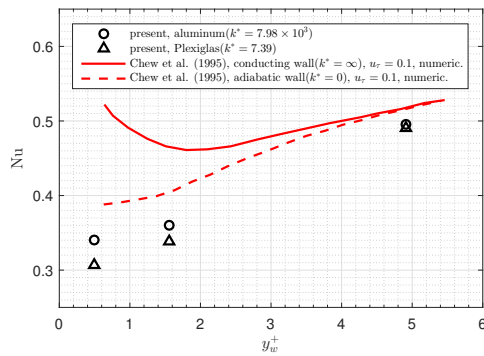


Figure 8: Nusselt number  $Nu$  on the wire surface as a function of the inner-scaled height of the wire. The present result is plotted together with that of the previous numerical study employing walls with heat conductivities of  $k^* = \infty$  and  $k^* = 0$ .

where  $\theta^* = \theta/(2\pi)$  and  $T_f$  is the film temperature:  $T_f = (T_w + T_\infty)/2$ . By taking the average of  $Nu$  over the wire surface, the mean Nusselt number is derived as:

$$Nu = \int_0^1 Nu(\theta^*) d\theta^*. \quad (11)$$

### 3.3 Numerical results

The result of the numerical calculation is plotted in figure 7 in the form

$$Nu \left( \frac{T_f}{T_\infty} \right)^{-0.17} = f(Re_f), \quad (12)$$

where the subscript  $f$  indicates the corresponding value at the film temperature. This correction of the Nusselt number is proposed by Collis & Williams (1959) to eliminate the effect of the overheat ratio. The results from several previous studies about the heat loss from a hot-wire sensor are also plotted together. The present results shows reasonable agreement in a qualitative tendency with the previous studies and it is again observed that higher conductivity of the material results in larger heat loss.

The Nusselt number as a function of the inner-scaled height of the wire centre  $y_w^+$  is shown in figure 8, where  $y_w^+$  can be calculated as  $y_w^+ = y_w \sqrt{S\rho_\infty/\mu_\infty}$ . The heat loss difference for the different wall conductivity becomes smaller as  $y_w^+$  increases and almost vanishes when

$y_w^+ = 4.9$ , which implies that the wall-proximity effect is negligible outside of the viscous sublayer. However, the present result is found to deviate from that of Chew et al. (1995). Apart from the wall conductivity, the difference in the size of computational domain (not mentioned) or the overheat ratio (although the effect of this factor is said to be negligible in their paper) might be the reasons for this discrepancy. Furthermore, the procedure in which they varied the wire height  $y_w^+$  by changing the real-scale position maintaining the velocity gradient  $S$  of the inflow is likely to be another reason, which may indicate that not only the inner-scaled height of the wire but also the real-scale distance have an influence on the heat loss.

The field temperature distribution around the wire is shown in figure 9. It is apparent that the heat from the wire hardly remains in the aluminum wall while it does for the Plexiglas wall. For the Plexiglas wall, a high-temperature zone inside the wall shifts further downstream due to the interaction of the temperature wake and the wall as the velocity gradient  $S$  increases, i.e. the distance  $y_w^+$  increases. The heat accumulates right beneath the wire for the cases with smaller  $y_w^+$ , which causes less heat loss from the wire. However, the  $Nu$  for the wire near solid walls are still higher than that of the wire in a freestream far away from a wall.

## 4 Conclusions

An experimental and numerical investigations of HWA measurement close to solid walls were carried out. Based on the present results, the following conclusions can be drawn:

- The thermal conductivity of the wall material affects the HWA reading, viz., walls with higher thermal conductivity lead to higher output voltages, i.e. larger overestimation of the velocity. It should be noted that highly conductive materials, such as aluminum, brass and steel show similar results despite the fact that the conductivity differs a factor of ten between them, For poorly conductive materials Plexiglas shows a much larger effect than styrofoam, despite the fact that Plexiglas has a thermal conductivity 3 orders of magnitude less than the metals, whereas styrofoam has an order of magnitude further reduced conductivity.
- Employing higher overheat ratios or longer sensors contributes to larger velocity overestimationst as these factors assist the additional heat loss from the sensor.
- The measured turbulence intensity and the velocity PDF are also affected by the wall conductivity and the overheat ratio: employing higher conductivity and higher temperature loading of the wire suppresses the reading of the turbulence intensity, and results in a narrower PDF in the low speed region within the viscous sublayer.
- The difference of the output voltage by varying the parameters can be seen only in the viscous sublayer, and one should note that the effect within the sublayer can easily be “hidden” when measured velocity profiles are employed to determine the absolute wall position and friction velocity as it is common.
- For poorly conducting walls, the heat accumulates beneath the wire inside the wall and it suppresses the additional heat loss. This heat accumulation

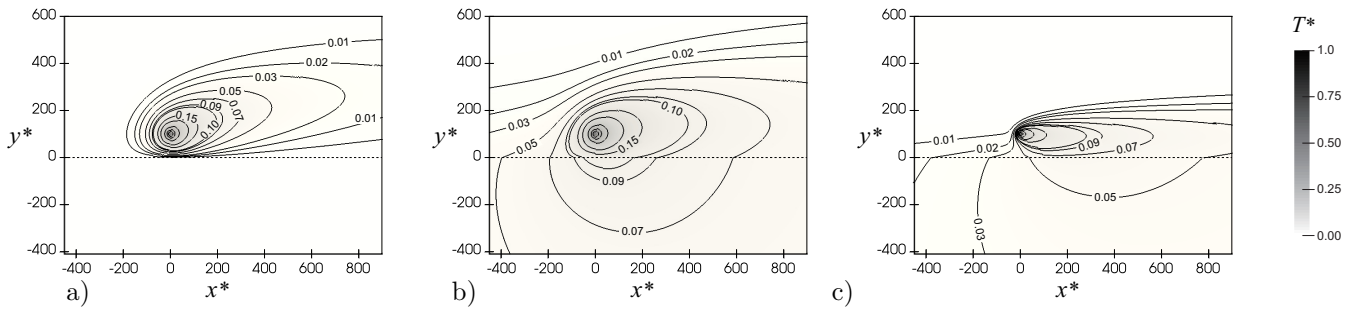


Figure 9: The distribution of temperature  $T^*$  around the heated wire above a solid wall. The broken line indicates the interface of the fluid and solid regions. a) Aluminum wall with the velocity gradient of  $S = 100 \text{ s}^{-1}$ . b) Plexiglas wall with the velocity gradient of  $S = 100 \text{ s}^{-1}$ . c) Plexiglas wall with the velocity gradient of  $S = 1000 \text{ s}^{-1}$ .

becomes larger as the inner-scaled height of the wire decreases.

Hence, in order to reduce the wall-effect on hot-wire readings in the viscous sublayer, it is beneficial to perform measurements above low conducting materials as well as operate the hot-wire at a low overheat ratio in order to obtain accurate measurements of both mean and fluctuating velocities.

## Acknowledgments

This work was done in the framework of the Keio University-KTH double-degree program and partly supported through JSPS KAKENHI Grant Number JP16K06900.

## References

- Alfredsson, P. H., Johansson, A. V., Haritonidis, J. H. & Eckelmann, H. (1988), The fluctuating wall-shear stress and the velocity field in the viscous sublayer, *Phys. Fluids*, Vol. 31, pp. 1026-1033.
- Alfredsson, P. H. & Örlü, R. (2010), The diagnostic plot—a litmus test for wall bounded turbulence data, *Eur. J. Mech. B-Fluids*, Vol. 29, pp. 403-406.
- Alfredsson, P. H., Örlü, R. & Schlatter, P. (2011a) The viscous sublayer revisited—exploiting self-similarity to determine the wall position and friction velocity, *Exp. Fluids*, Vol. 51, pp. 271-280.
- Alfredsson, P. H., Segalini, A. & Örlü, R. (2011b), A new scaling for the streamwise turbulence intensity in wall-bounded turbulent flows and what it tells us about the “outer” peak, *Phys. Fluids*, Vol. 23, 041702.
- Bhatia, J. C., Durst, F. & Jovanovic, J. (1982), Corrections of hot-wire anemometer measurements near walls, *J. Fluid Mech.*, Vol. 122, pp. 411-431.
- Chew, Y., Shi, S. & Khoo, B. (1995), On the numerical near-wall corrections of single hot-wire measurements, *Int. J. Heat Fluid Flow*, Vol. 16, pp. 471-476.
- Collis, D. & Williams, M. (1959), Two-dimensional convection from heated wires at low Reynolds numbers, *J. Fluid Mech.*, Vol. 6, pp. 357-384.
- Durst, F., Shi, J.M. & Breuer, M. (2002), Numerical prediction of hot-wire corrections near walls, *J. Fluids Eng.*, Vol. 124, pp. 241-250.
- Durst, F. & Zanoun, E. S. (2002), Experimental investigation of near-wall effects on hot-wire measurements, *Exp. Fluids*, Vol. 33, pp. 210-218.
- George, W. K., Beuther, P. D. & Shabbir, A. (1989), Polynomial calibrations for hot wires in thermally varying flows, *Exp. Therm Fluid Sci.*, Vol. 2, pp. 230-235.
- Krishnamoorthy, L., Wood, D., Antonia, R. & Chambers, A. (1985), Effect of wire diameter and overheat ratio near a conducting wall, *Exp. Fluids*, Vol. 3, pp. 121-127.
- Lange, C., Durst, F. & Breuer, M. (1998), Momentum and heat transfer from cylinders in laminar crossflow at  $10^{-4} \leq \text{Re} \leq 200$ , *Int. J. Heat Mass Transfer*, Vol. 41, pp. 3409-3430.
- Örlü, R., Fransson, J. H. M. & Alfredsson, P. H. (2010), On near wall measurements of wall bounded flows — The necessity of an accurate determination of the wall position, *Prog. Aerosp. Sci.*, Vol. 46, pp. 353-387.
- Örlü, R., Segalini, A., Klewicki J. & P. H. Alfredsson (2016) High-order generalisation of the diagnostic plot to turbulent boundary layers. *J. Turbul.* Vol. 17, pp. 664-677.
- Örlü, R. & Schlatter, P. (2011), On the fluctuating wall shear stress in zero pressure-gradient turbulent boundary layer flows, *Phys. Fluids*, Vol. 23, 021704.
- Polyakov, A. & Shindin, S. (1978), Peculiarities of hot-wire measurements of mean velocity and temperature in the wall vicinity, *Lett. Heat Mass Transfer*, Vol. 5, pp. 53-58.
- Shi, J. M., Breuer, M., Durst, F. & Schäfer, M. (2003), An improved numerical study of the wall effect on hot-wire measurements, *J. Heat Transfer*, Vol. 125, pp. 595-603.
- Zanoun, E. S., Durst, F. & Shi, J. M. (2009), The physics of heat transfer from hot wires in the proximity of walls of different materials, *Int. J. Heat Mass Transfer*, Vol. 52, pp. 3693-3705.

# FURTHER ASSESSMENT OF THE GREY-AREA ENHANCED $\sigma$ -DES APPROACH FOR COMPLEX FLOWS

M. Fuchs<sup>1</sup>, C. Mockett<sup>2</sup>, J. Sesterhenn<sup>1</sup> and F. Thiele<sup>1</sup>

<sup>1</sup>*Technische Universität Berlin, Germany*

<sup>2</sup>*CFD Software Entwicklungs- und Forschungsgesellschaft mbH, Berlin, Germany*

marian.fuchs@cfp.tu-berlin.de

## Abstract

In Mockett et al. (2015) and Fuchs et al. (2014), we presented a novel DES-based approach referred to as  $\sigma$ -DES, which targets accelerated transition from RANS to LES in free separated shear layers, a problem often encountered for state-of-the-art hybrid RANS-LES models such as DDES as proposed by Spalart et al. (2006). The contribution aims at summarising experience gained with the new method over the last two years for a range of different complex test cases, i.e. an unheated, static round jet at  $M = 0.9$  as well as two incompressible cases, i.e. an inclined delta wing and a 4-wheel rudimentary landing gear. Results show that the new  $\sigma$ -DES improves predictive accuracy significantly for both the jet and delta wing cases, which are both strongly impacted by the RANS to LES transition issue. The landing gear test case furthermore demonstrates that the new approach is applicable to complex geometries and maintains key features of standard hybrid RANS-LES methods, e.g. an automatic switch between RANS- and LES-mode as well as a shielding capability for attached boundary layers.

## 1 Introduction

Since its introduction in Spalart et al. (1997), detached-eddy simulation (DES) has become a powerful tool to accurately calculate aerodynamics and aeroacoustics statistics for high Reynolds number wall-bounded flows at moderate computational expense. In recent years, the focus of further enhancing DES and indeed other hybrid RANS-LES methods has shifted to a particular issue which concerns the potential delay of transition from RANS to LES in separated shear layers (often referred to as the “grey area”).

For non-zonal methods such as DES, the selection of RANS and LES mode is automatic and no sharp interface between the two regions exist. Creating resolved turbulent content from a smooth 2D incoming RANS boundary layer downstream of separation is therefore a challenge, bearing in mind that missing information effectively has to be generated in this region. Experience shows (e.g. see Spalart (2009)) that standard DES methods often exhibit a high production of eddy viscosity in this sensitive region, which leads to a strong damping of the natural Kelvin-Helmholtz instabilities vital to transition from a quasi “laminar” 2D to fully turbulent 3D flow state. The spatial extent of the grey area significantly influences the flow prediction, as usually in this scenario modelled turbulent stresses drop from RANS levels without appropriate compensation through resolved stresses as the model switches to LES-mode, resulting in an under-prediction of the total stress balance.

Within the recent EU-funded research project Go4Hybrid (2013-2015), an improvement to DES denoted as  $\sigma$ -DES has been developed, which was first published by Mockett et al. (2015) with subsequent results presented in Fuchs et al. (2014) and Fuchs et al. (2015). The new approach focusses on mitigating the grey area problem whilst maintaining both the generality and non-zonal nature of DES. This contribution aims at summarising the experience gained with the new approach for more complex flows over the last two years, thereby illustrating its potential to replace standard DES in the future.

## 2 Formulation of approach

Two approaches are subsequently presented which aim at mitigating the grey area issue. Both methods use only local flow quantities and are hence suitable for implementation in general purpose unstructured CFD codes.

### 2.1 Modification of LES branch of DES

The first approach concerns the modification of the LES branch of DES. For DES formulations based on linear eddy viscosity RANS models (in this paper, we are presenting a formulation based on the Spalart-Allmaras (SA) RANS model, but the method is generally not restricted to a particular RANS model), the SGS model behaviour is equivalent to the algebraic LES Smagorinsky model (assuming local equilibrium between production and dissipation). In our approach, we seek to alter the SGS behaviour of DES so that it reduces to the LES  $\sigma$  model of Nicoud et al. (2011) instead. The  $\sigma$  LES model offers the particular advantage that it can discern between a quasi “laminar” 2D flow state as in the early shear layer region and a fully 3D turbulent state. For the former, it returns very low levels of eddy viscosity, which frees up the vital Kelvin-Helmholtz instabilities to accelerate transition to fully resolved LES. In contrast, the LES Smagorinsky model is sensitised to all velocity gradients (corresponds with its inability to model transitional flows), thus produces excessive levels of eddy viscosity even when the flow is two-dimensional such as in the early shear layer region after separation from a smooth RANS boundary layer.

We present a formulation based on the Spalart-Allmaras delayed-DES (DDES) model of Spalart et al. (2006), as we want to use its inbuilt shield function. The SA-DDES model contains the vorticity rate invariant  $S^* = \sqrt{(2\Omega_{ij}\Omega_{ij})}^1$  as part of the modified vorticity magnitude:

<sup>1</sup>where  $\Omega_{ij} = 0.5(\partial U_i/\partial x_j - \partial U_j/\partial x_i)$

$$\tilde{S} = S^* + \frac{\tilde{\nu}}{\kappa^2 L_{\text{DDES}}^2} f_{v2}, \quad (1)$$

$$L_{\text{DDES}} = L_{\text{RANS}} - f_d \max[0, L_{\text{RANS}} - L_{\text{LES}}],$$

where  $L_{\text{DDES}}$  is the turbulent length scale of the hybrid model,  $L_{\text{RANS}} = d_w$  the wall distance,  $L_{\text{LES}} = C_{\text{DES}} \Psi \Delta$  the LES length scale and  $f_d$  the shield function. The modified vorticity magnitude  $\tilde{S}$  enters into the production term of the  $\tilde{\nu}$  transport equation as well as the SA model  $r$ -function:

$$P_{\tilde{\nu}} = C_{b1} [1 - f_{t2}] \tilde{S} \tilde{\nu}, \quad (2)$$

$$r = \min[\tilde{\nu} / (\tilde{S} \kappa^2 L_{\text{DDES}}^2), 10]. \quad (3)$$

To obtain the  $\sigma$ -DDES formulation, the term  $S^*$  in Eq. 1 is substituted with a corresponding term including the velocity gradient based scale  $S_\sigma$  of the  $\sigma$  LES model:

$$S_{\sigma\text{-DDES}}^* = S^* - f_d \cdot \text{pos}(L_{\text{RANS}} - L_{\text{LES}}) \cdot (S^* - B_\sigma S_\sigma^*), \quad (4)$$

where the pos-function is defined as:

$$\text{pos}(a) = \begin{cases} 0 & , \text{ if } a \leq 0 \\ 1 & , \text{ if } a > 0 \end{cases}. \quad (5)$$

$B_\sigma = 67.7$  is a calibrated constant which accounts for the difference of  $S^*$  to  $S_\sigma$  in turbulent regions.  $S_\sigma$  is directly taken from the  $\sigma$  LES-model:

$$S_\sigma^* = \frac{\sigma_3 (\sigma_1 - \sigma_2) (\sigma_2 - \sigma_3)}{\sigma_1^2}, \quad (6)$$

where  $\sigma_1 \geq \sigma_2 \geq \sigma_3 \geq 0$  are the three singular values of the local velocity gradient tensor  $g_{ij} := \partial U_i / \partial x_j$ . The DDES shielding function  $f_d$  is used in the definition of the new production scale  $S_{\sigma\text{-DDES}}^*$  (Eq. 4) to prevent an activation of the  $\sigma$  LES-mode inside attached boundary layers and to use the original vorticity rate invariant  $S^*$  instead. To ensure equivalent shielding behaviour as in standard SA-DDES, the constants of the shield function  $f_d$  had to be re-calibrated (see Fuchs et al. (2015)).

## 2.2 Alternative definition of LES filter width $\Delta$

As an additional means to accelerate RANS to LES transition in separated shear layers, an alternative formulation for the LES filter width  $\Delta$  is used, which was proposed by P. Spalart in Mockett et al. (2015). It is based on the idea to sensitise the filter width  $\Delta$ , which for standard DDES is usually a geometric measure of the local grid size, i.e.  $\Delta_{\text{max}} = \max(\Delta_x, \Delta_y, \Delta_z)$ , to the orientation of the vorticity vector. The new LES filter scale denoted as  $\tilde{\Delta}_\omega$  reduces to  $\mathcal{O}(\max\{\Delta_x, \Delta_y\})$  in regions where the flow is two-dimensional with respect to the xy-plane and the vorticity vector aligned to the third direction  $z$ . Hence, it cancels out the influence of the  $\Delta_z$  spacing on the calculation of  $\Delta$ , which is physically justifiable as the smallest resolvable scales in the 2D flow should not depend on  $\Delta_z$ . Given a cell with its cell centre vector being  $\vec{r}$  and its vertices located at  $\vec{r}_n$  ( $n = 1 \dots n_{\text{max}}$ , where  $n_{\text{max}}$  is the number of cell vertices), the modified formulation reads:

$$\tilde{\Delta}_\omega = \alpha \cdot \frac{1}{\sqrt{3}} \max_{n,m=1 \dots n_{\text{max}}} |I_n - I_m|, \quad (7)$$

where  $I_n = \vec{n}_\omega \times (\vec{r}_n - \vec{r})$ ,  $\vec{n}_\omega$  is the normalised vorticity vector and  $\alpha = 1.025$ . On many practical grids,  $\Delta_z$  is often relatively coarse in the early shear layer region relative to  $\Delta_x$  and  $\Delta_y$ , so that the  $\tilde{\Delta}_\omega$  scale returns effectively lower values than the standard  $\Delta_{\text{max}}$  formulation here. Thus, it has a similar effect as using the  $\sigma$  SGS model in a sense that it reduces the effective eddy viscosity entering the viscous term in this region (in LES-mode,  $\nu_t \propto \Delta^2$ ). Unlike the  $\sigma$  modification, the  $\tilde{\Delta}_\omega$  is only active on strongly anisotropic grids, and neutral (i.e. same performance as  $\Delta_{\text{max}}$ ) for isotropic cells.

## 3 Numerical methodology

A customised version of the open source CFD package OpenFOAM® was used in this work, which is a cell-centred, unstructured, finite-volume based code. All applied solvers are based on the SIMPLE pressure-velocity coupling algorithm. An implicit second order accurate Euler scheme was applied for time integration, and the hybrid blending scheme of Travin et al. (2000) was used to discretise the convective term of the momentum equation. The latter applies a localised blending between low-dissipation second order central differences in well-resolved turbulent regions and a robust second order accurate upwind scheme in coarse grid regions or regions of irrotational flow.

## 4 Results and discussion

One of the most prominent examples of the arey area impact are jet flows, for which DES-like methods were considered unsuitable prior to the Go4Hybrid project (at least on practical grids). To demonstrate the improvement achieved with the new  $\sigma$ -DDES approach, simulations for an unheated, round static jet at  $M = 0.9$  have been conducted, for which preliminary results were presented in Fuchs et al. (2014). The case is suitable to benchmark CFD methodologies for jet flow prediction, where results have been published in numerous CFD studies before, e.g. by Shur et al. (2011). In this study, simulations were conducted on three different grids ranging from 1.6M (G1) to 8.4M (G3) in cell count (detailed grid statistics can be found in Shur et al. (2011)).

Fig. 1 gives an impression of the instantaneous flow field for standard and  $\sigma$ -DDES on different grids. The new  $\sigma$ -DDES seems to be very effective in promoting resolved turbulent structures in the early shear layer region, whereas standard SA-DDES features stable shear layers and a much delayed onset of realistic turbulence. A noticeable effect of using the  $\tilde{\Delta}_\omega$  length scale compared to  $\Delta_{\text{max}}$  is seen for SA-DDES, but not to the extent that the grey area is sufficiently mitigated.

The model behaviour of  $\sigma$ -DDES can be inspected in Fig. 2. Both the modified SGS behaviour and the additional reduction of  $\Delta$  through  $\tilde{\Delta}_\omega$  result in significantly reduced levels of eddy viscosity in the early shear layer, which frees flow instabilities to promote rapid transition to 3D turbulence. Once fully resolved LES structures have established, eddy viscosity increases to regular SGS levels.

In terms of mean flow statistics, standard SA-DDES +  $\Delta_{\text{max}}$  massively over-predicts the jet core length on G1, whereas  $\sigma$ -DDES +  $\tilde{\Delta}_\omega$  performs very reliable on all three grids (see Fig. 3). Velocity fluctuation profiles on the jet lipline visualised in Fig. 4 confirm these findings. The  $\sigma$ -DDES is very effective in predicting the unsteady

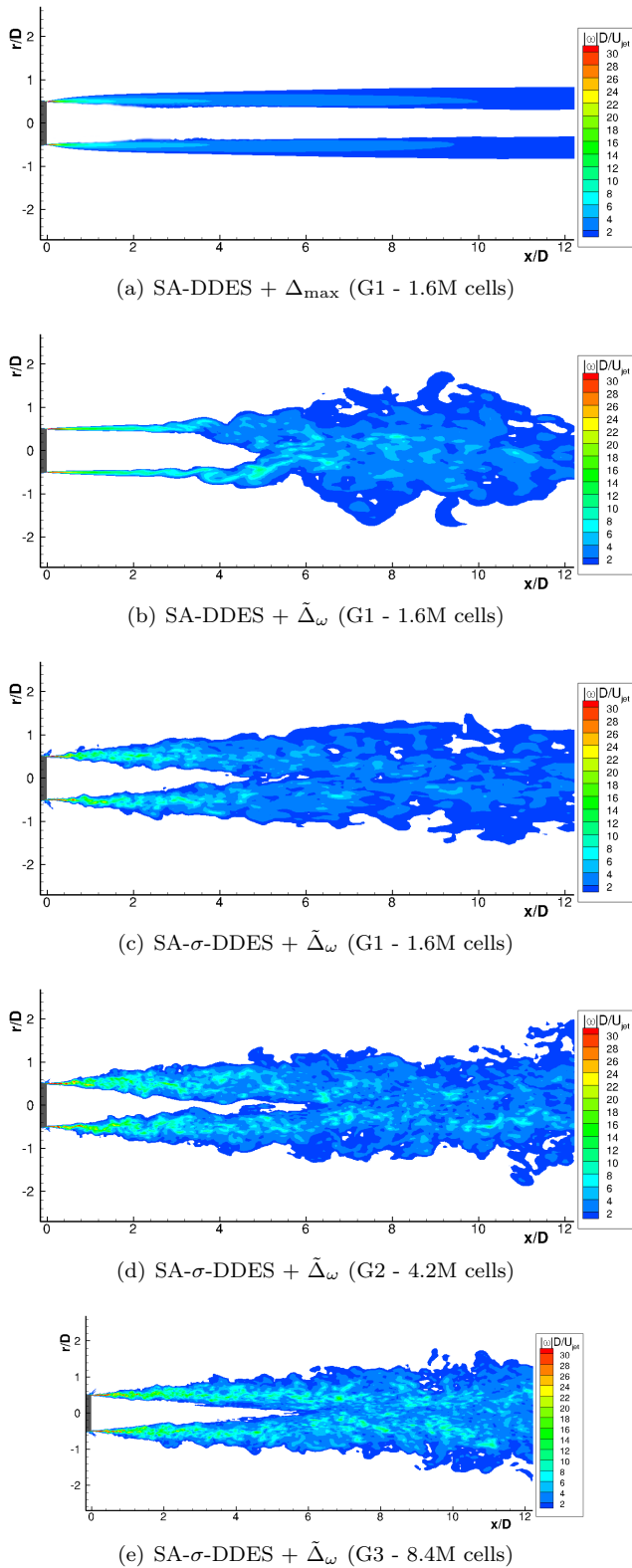


Figure 1: Contours of instantaneous vorticity magnitude on jet symmetry plane.

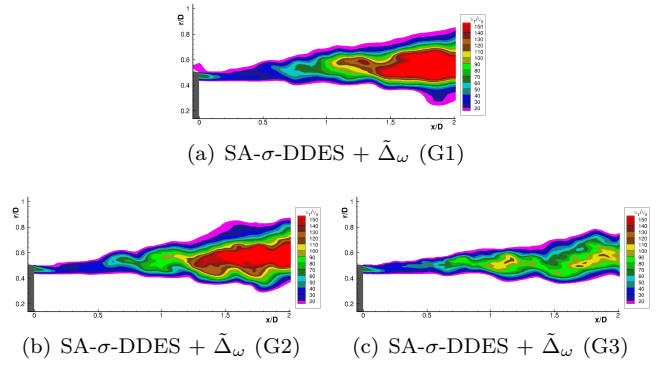


Figure 2: Contours of instantaneous eddy viscosity ratio on jet symmetry plane for  $\sigma$ -DDES.

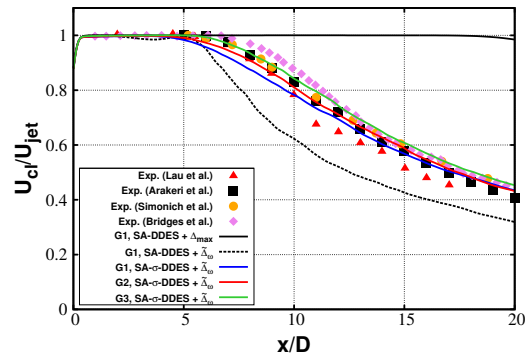


Figure 3: Profiles of streamwise mean and velocity fluctuations along the centreline (middle) and lipline (bottom).

solution content and is hence also capable for aeroacoustics jet simulations.

The main advantage of using  $\sigma$ -DDES however is not envisioned for simulations of isolated jets, for which rigorous grid refinement or switching to alternative approaches such as implicit LES (ILES) are also viable options for countering the grey area problem. In offering an inbuilt shielding functionality for attached boundary layers treated with RANS, the method enables studying installation effects such as jet-wing interaction at meaningful Reynolds numbers, for which e.g. ILES is not suitable. First promising results from an ongoing research project using  $\sigma$ -DDES for jet noise installation effects are presented in Mockett et al. (2016).

To assess the generality of the  $\sigma$ -DDES approach for a flow topology deviating from planar shear, the incompressible flow over a generic delta wing subjected to an angle of attack  $\alpha = 23^\circ$  and at  $Re_{mac} = 1 \times 10^6$  was studied (see Fuchs et al. (2015) for more details). Here, the flow separates from the sharpened leading edges of the wing to form two dominant vortices on the suction side, whereby the shear layers roll up inwards. A block-structured grid consisting of 6.3M cells has been employed for the test case, which features a conical structure over large parts of the wings and fans out downstream to ensure a constant resolution of the primary vortices using essentially isotropic cells.

Instantaneous pictures of the flow field and turbulent structures for both standard SA-DDES using  $\Delta_{max}$  and SA- $\sigma$ -DDES using  $\Delta_\omega$  are depicted in Fig. 5. For standard SA-DDES, the primary vortices remain relatively stable until far downstream of the apex up to  $\approx 70\%$  of

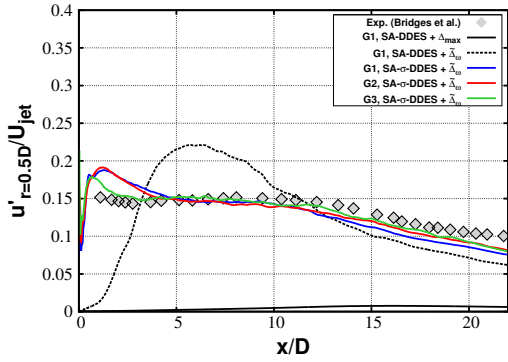


Figure 4: Profiles of streamwise mean and velocity fluctuations along the centreline (middle) and lipline (bottom).

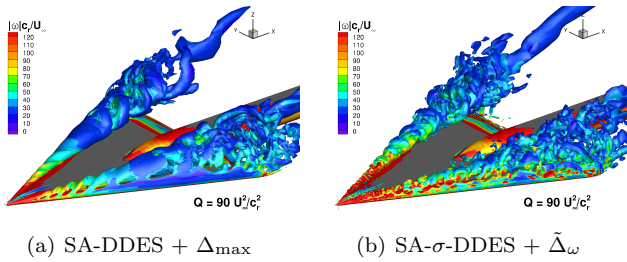


Figure 5: Instantaneous vortex structures over delta wing visualised via Q-criterion.

the wing depth. This is different for  $\sigma$ -DDES, where rich fine-scale turbulent content is seen very early on in the shear layers.

Correspondingly, we see much improved prediction of pressure fluctuations on the surface, where spanwise profiles at two different chord stations are plotted in Fig.6). At early chord stations, SA-DDES strongly under-predicts fluctuations, whereas fluctuations are soundly over-predicted ones the energy-containing main vortices break-up. One of the key quantities of interest for delta wings is the prediction of the vortex breakdown location, which occurs at some point upstream of the trailing edge for the selected angle of attack. Fig. 7 shows a comparison of PIV data and the two DDES variants at two different downstream locations, which indicate a very acceptable performance of  $\sigma$ -DDES for this sensitive test case, whereas the onset of vortex breakdown is predicted too far upstream by standard SA-DDES.

In addition to flow cases for which the separation position is geometrically fixed, a 4-wheel rudimentary land-

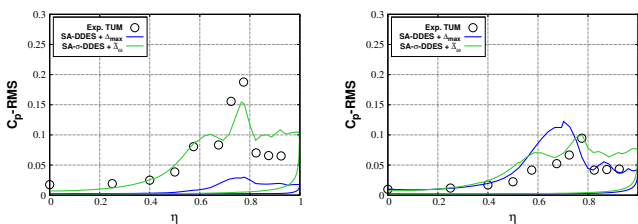


Figure 6: Spanwise profiles of surface pressure fluctuations at streamwise locations  $x/c_r = 0.4$  (left) and  $x/c_r = 0.6$  (right),  $c_r$  ... root chord.

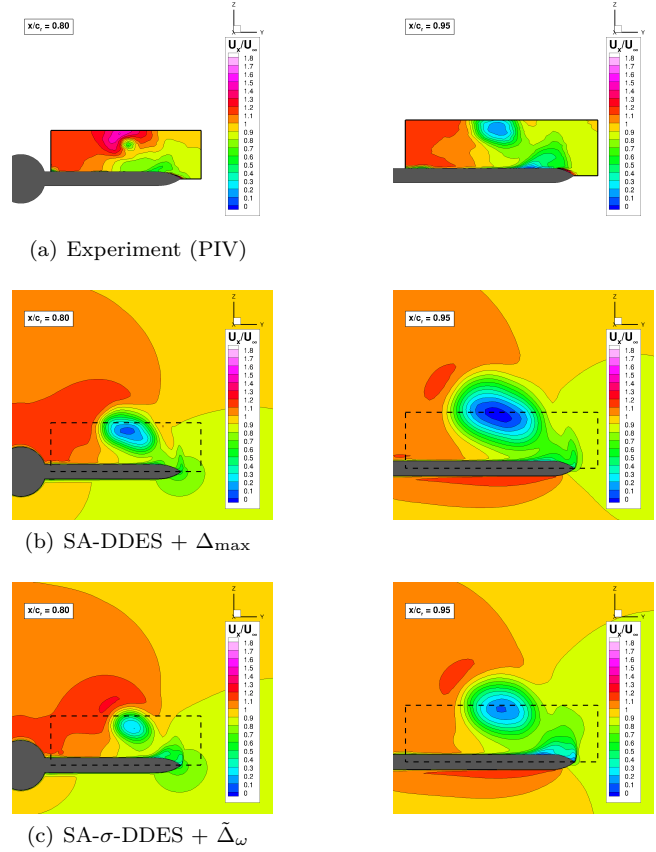


Figure 7: Comparison of time-averaged streamwise velocity component for two scanning windows at  $x/c_r = 0.8$  (left) and  $x/c_r = 0.95$  (right).

ing gear (RLG) configuration was investigated which features pressure-induced separation and flow impingement. The test case was frequently studied in the past, e.g. in Wang et al. (2013), and is envisioned to be used to validate the  $\sigma$ -DDES approach for the prediction of low-Mach number aeroacoustics. In a first step towards this goal, the validation of the incompressible aerodynamic flow field is presented here. The case is run at  $Re_D = 1 \times 10^6$  ( $D$  ... diameter of wheel) on a structured grid exhibiting  $\sim 11$ M cells.

For this test case,  $\sigma$ -DDES was compared to the Spalart-Allmaras improved-DDES (IDDES) model (see Shur et al. (2008)). IDDES was chosen here to allow for direct comparability to existing benchmark simulations, however no noticeable difference in model behaviour between SA-DDES and SA-IDDES is expected for the RLG (this is supported by findings of previous studies, e.g. Wang et al. (2013)). Fig. 8 gives an impression of the unsteady solution of both SA-IDDES and  $\sigma$ -DDES, where both models are seen to deliver rich turbulent content. This is in line with expectation, as the RLG was identified as only weakly affected by the grey area issue in previous studies.

In terms of mean aerodynamic prediction, both models perform equivalently, where predicted mean surface pressure (Fig. 9) and integral force coefficients ( $C_{D,L} = 1.725, -0.230$  for IDDES,  $C_{D,L} = 1.738, -0.241$  for  $\sigma$ -DDES) are very comparable. Shielding of the attached RANS boundary layers is active and working for both models, as can be deduced from the corresponding surface pressure values upstream of separation (i.e. for  $0^\circ < \Theta \lesssim 120^\circ$  and  $240^\circ \lesssim \Theta < 360^\circ$ ).

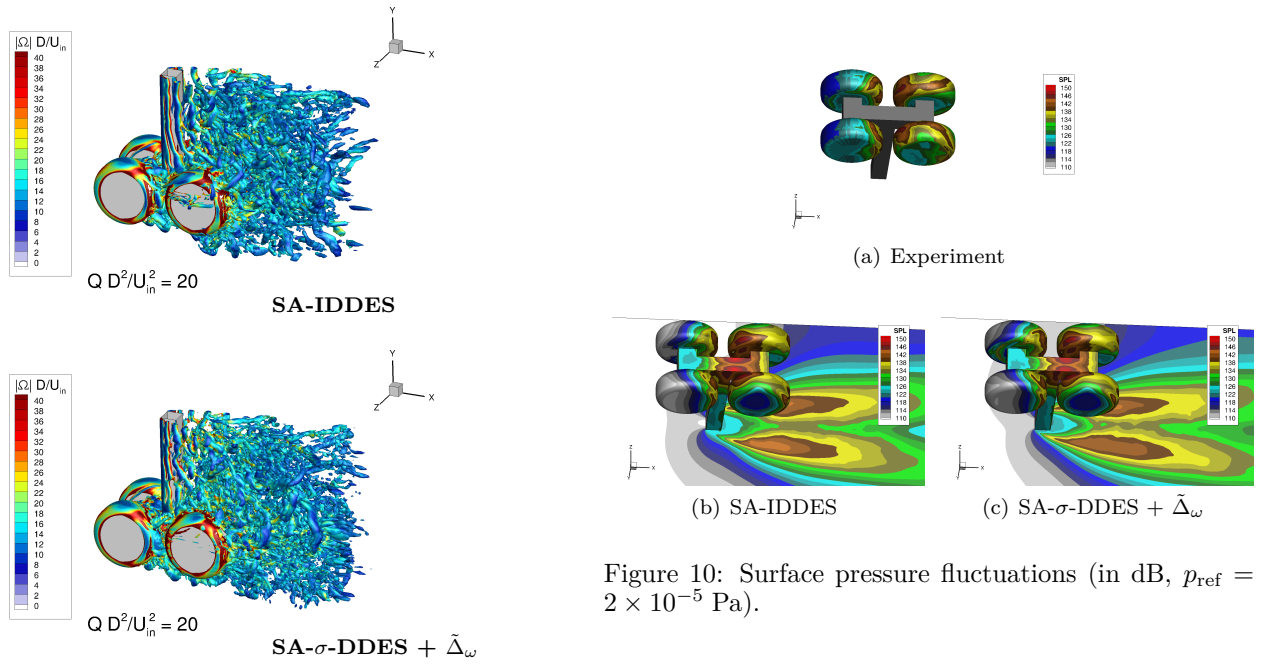


Figure 10: Surface pressure fluctuations (in dB,  $p_{ref} = 2 \times 10^{-5}$  Pa).

Figure 8: Instantaneous turbulent structures around RLG visualised via the  $Q$ -criterion.

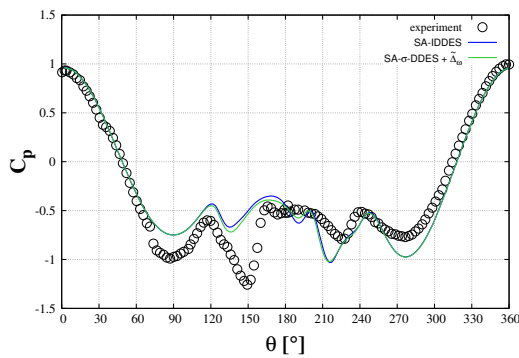


Figure 9: Surface pressure coefficient on front wheel.

To assess the suitability of the  $\sigma$ -DDES approach to predict farfield noise for the RLG, contours of surface pressure fluctuations are inspected in Fig. 10. Despite the more aggressive switch following separation for the  $\sigma$ -DDES model, no excessive pressure fluctuations on the RLG surface and ceiling wall are noticed, thus indicating that it is suitable to capture the dominant dipole noise sources on the solid surfaces.

The very comparable performance of IDDES and  $\sigma$ -DDES also translates to spectral solution content, although mild local differences are seen in some regions. Fig. 11 highlights two such regions, where power spectral densities of surface pressure are analysed. The  $\sigma$ -DDES approach seems to have a mildly enhancing effect for the separation around the inner shoulder of the wheel, but shows identical behaviour for the main separation line on the wheel. In addition, slightly enhanced high-frequency content is noticed in the impingement region of the rear wheels, where the separated wake from the front wheels penetrates the rear wheel surface.

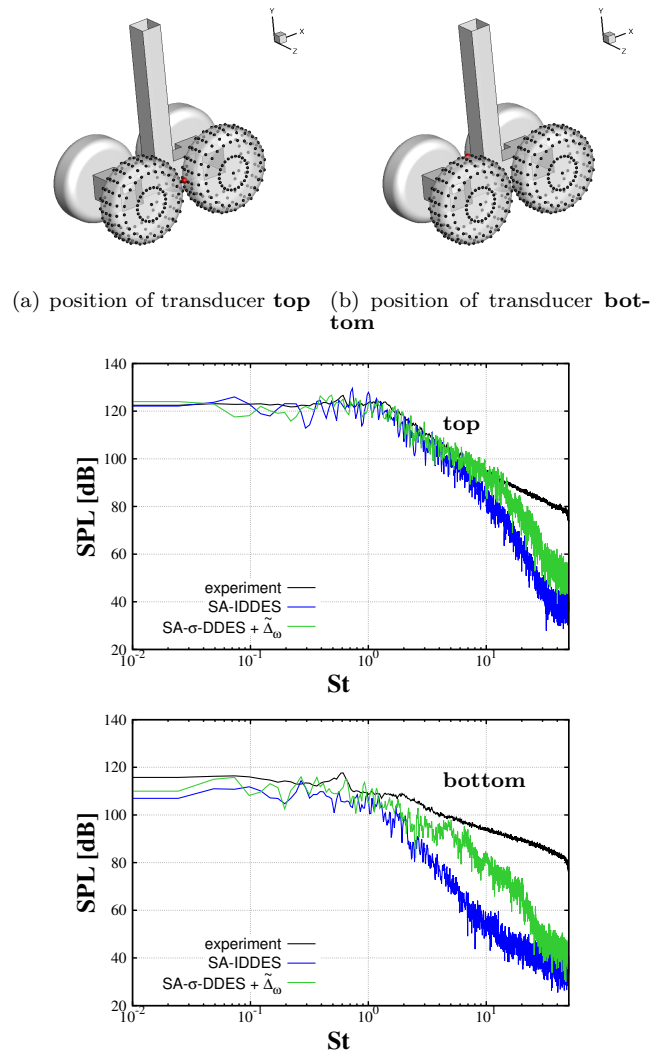


Figure 11: Power spectral densities of surface pressure fluctuations at different positions.

## 5 Conclusions and outlook

Results for the novel hybrid RANS-LES approach  $\sigma$ -DDES have been presented for three fairly different flow topologies, where a comparison was drawn to a currently standard industrial-used hybrid RANS-LES model, i.e. SA-(I)DDES. The  $\sigma$ -DDES approach proves to be very effective in mitigating the grey area problem (i.e. delayed transition of RANS to LES in free shear layers) for test cases strongly affected by it such as jet flows and the delta wing using a moderate grid resolution. Furthermore, the landing gear test case demonstrates that for cases with lesser relevance of the grey area issue, the new method performs equally as good as the standard hybrid model. Core features of SA-DDES such as its non-zonal nature, its general applicability to complex geometries and the shielding capability of attached boundary layers are maintained, so that the method can be considered a candidate to replace standard SA-DDES entirely in the future.

### Acknowledgments

This work has been partly financed by the EU FP7 project “Go4Hybrid” (ACP3-GA-2013-60536-Go4Hybrid). The assistance of Denes Fischer (TU Berlin) with the landing gear test case is gratefully acknowledged.

### References

Fuchs M., Mockett C., Steger M. and Thiele F. (2014), A novel DES-based approach to improve transition from RANS to LES in free shear layers, *Proceedings of the 10th International ERCOFTAC Symposium on Engineering Turbulence Modelling and Measurements*, Marbella / Spain.

Fuchs M., Mockett C., Sesterhenn J. and Thiele F. (2015), Assessment of novel DES approach with enhanced SGS modelling for prediction of separated flow over a delta wing, *Proceedings of the 22nd AIAA Computational Fluid Dynamics Conference*, AIAA 2015-3433, Dallas / TX.

Mockett C., Fuchs M., Garbaruk A., Shur M., Spalart P., Strelets M., Thiele F. and Travin A. (2015), Two

non-zonal approaches to accelerate RANS to LES transition of free shear layers in DES, *Notes on Numerical Fluid Mechanics and Multidisciplinary Design*, vol. 130, pp. 187–202, Springer.

Mockett C., Fuchs M., Kramer F., Michel U. and Thiele F., Turbulence modelling and meshing developments for the prediction of jet noise installation effects, *Proceedings of the 22nd AIAA/CEAS Aeroacoustics Conference*, AIAA 2016-2933, Lyon / France.

Nicoud F., Baya Toda H., Cabrit O., Bose S. and Lee J. (2011), Using singular values to build a subgrid-scale model for large eddy simulations, *Physics of Fluids*, 23, 085106.

Shur M., Spalart P., Strelets M. and Travin A. (2008), A hybrid RANS-LES approach with delayed-DES and wall-modelled LES capabilities, *International Journal of Heat and Fluid Flow*, 29:1638-1649.

Shur M., Spalart P. and Strelets M. (2011), LES-based evaluation of a microjet noise reduction concept in static and flight conditions, *Journal of Sound and Vibration*, Vol. 330, No.17, pp. 4083–4097.

Spalart P., Jou W., Strelets M. and Allmaras S. (1997), Comments of feasibility of LES for wings, and on a hybrid RANS/LES approach, *Advances in DNS/LES*, 1.

Spalart P., Deck S., Shur M., Squires K., Strelets M. and Travin A. (2006), A new version of detached-eddy simulation, resistant to ambiguous grid densities. *Theoretical and Computational Fluid Dynamics*, 20:181-195.

Spalart P. (2009), Detached-Eddy Simulation, *Annual Review Fluid Mechanics*, 41:181-202.

Travin A., Shur M., Strelets M. and Spalart P. (2001), Physical and numerical upgrades in the detached-eddy simulation of complex flows, *Proceedings of the 41st Euromech Colloquium on LES and Complex Transitional and Turbulent Flows*, Munich, Germany, 2000.

Wang L., Mockett C., Knacke T. and Thiele F. (2013), Detached-Eddy Simulation of Landing Gear-Noise, *Proceedings of the 19th AIAA/CEAS Aeroacoustics Conference*, AIAA 2013-2069, Berlin / Germany.

# AN INVESTIGATION OF TRANSITION PREDICTION USING IMPROVED KDO RANS MODEL

J.L. Xu<sup>1</sup>, D. Xu<sup>2</sup>, Y. Zhang<sup>3</sup> and J.Q. Bai<sup>3</sup>

<sup>1</sup>*Department of Energy and Power Engineering, Beihang University, Beijing, 10191, China*

<sup>2</sup>*School of Aerospace, Xi'an Jiaotong University, Shanxi, 710049, China*

<sup>3</sup>*School of Aeronautics, Northwestern Polytechnical University, Shanxi, 710072, China*

xujl@buaa.edu.cn

## Abstract

By extending Bradshaw's assumption from the free shear regions to the wall, KDO turbulence model (Xu, Zhang and Bai, 2015) has established a new Reynolds stress constitution. The turbulence intensity ratio  $\tau_{12}/k$  and the coefficient of the dissipation term are the only two empirical coefficients. They were both calibrated by one slice of incompressible flat plate boundary layer and thus there are Reynolds number effects. This paper discovers that once the Reynolds number effects are cured to some degree, the model could naturally capture various transition phenomena. The test cases includes the classic bypass transition of T3A and T3B boundary layer, natural transition of T3A- boundary layer and separation bubble transition of Aero-A airfoil. This improved KDO model is not able to capture the precise process of the laminar-turbulent flow transition; however, it can capture the transition onset location and the peak of skin friction after the transition. The accuracy is good, especially in high Reynolds number and complex flows.

## 1 Introduction

While RANS turbulence models have not reached the maturity for always-reliable predictions of fully developed turbulence, the transition from laminar to turbulent flows has raised a greater challenge to human beings. Transition phenomena extensively exist in the internal and external flows of industry devices, and the prediction and control of transition are of great importance for the improvements of industry devices. It is often that the accuracy of laminar-turbulence transition prediction is far more important than that of fully developed turbulence prediction. For instance, the skin friction and heat transfer coefficients can rise significantly and exceeds the value in fully developed region. For hypersonic cruise, the magnitudes of the skin friction and wave drag are of the same order.

For decades, the community has the impression that, RANS and related Reynolds stress closure can only describe fully developed turbulence. For laminar-turbulent transition which seems to be far more complex than fully developed turbulence, researchers turn to other strategies such as  $e^N$  method (Smith and Gamberoni 1956) (Ingen 1956) (Krimmelbein, Krumbein and Schrauf 2010) and introductions of intermittency factor  $\gamma$  (Dhawan and Narasimha 1958) (Suzen and Huang 2000) (Suzen et al. 2003) (Menter et al. 2006) (Lantry and Menter 2009) or laminar turbulent kinetic energy (Volino and Simon 1997) (Mayle and Schulz 1997) (Walters and Cokljat 2008) (Lardeau et al. 2009).

In the 1990s, Europe launched the project 'TransPerturb' to evaluate and improve the ability of turbulence models at that time to predict transition under a variety of flow conditions and the influence of varying degrees of free-stream disturbance. Savill (1993) found that only a few generated transitions, and the length of transition region was too short. The latest 'TransPerturb' report concluded that the transition prediction was fragile and unreliable not considering intermittency. Some people even believe that the predicted transition by low-Re models comes from numerical coincidences. Nevertheless, in theory, RANS is undoubtedly able to describe transition phenomena, as long as every unclosed term is given the correct value. Maybe this is one reason why attempts to simulate transition using RANS models have never stopped ever since its invention. A number of studies precede the explorations of effective transition predictions using low-Re turbulence models, including those of Chen, Lien and Leschziner (1998), Palikaras, Yakinthos and Goulas (2002), Lardeau, Leschziner and Li (2004), and Lardeau and Leschziner (2006). This work continues to explore a RANS closure system that relies on the evolution of its own transport equations to reproduce transition process. It does not contain any  $e^N$  method,  $\gamma$  equation or laminar turbulent kinetic energy elements.

## 2 RANS closure strategy for transition

The turbulent Kinetic energy Dependent Only model (KDO) (Xu, Zhang and Bai 2015) tried to adopt a more reliable source and less empirical coefficients, which is a good starting point. Most of its closure strategies are employed here. By extending Bradshaw's assumption down to the wall, a new Reynolds stress constitutive relation is established as,

$$R_b = \tau_{12}/k \quad (1)$$

$$-\overline{u'_i u'_j} = R_b k \frac{2S_{ij}}{S} \quad (2)$$

The turbulence intensity ratio  $R_b$  is the only empirical coefficient in the Reynolds stress constitutive relation, which is regarded as a measurement of wall constraint on the correlation between stream-wise and wall-normal fluctuations. It becomes the Bradshaw's constant, which is about 0.3 far from the wall. This treatment has evaded the difficulties in seeking relations between turbulent stresses and mean strains, which not only reduces the number of empirical coefficients but also implicitly accounts for many physics such as geometry effects and non-locality/Reynolds stress transport. Turbulent Reynolds number  $Re_k = \rho\sqrt{k}d/\mu$  and eddy viscos-

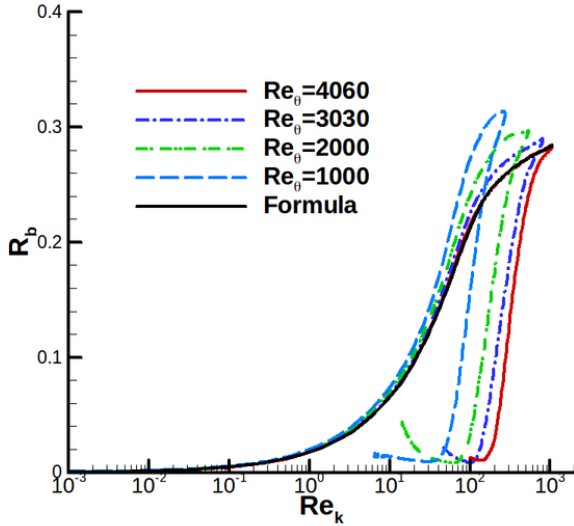


Figure 1: Stress intensity distributed in  $Re_k$

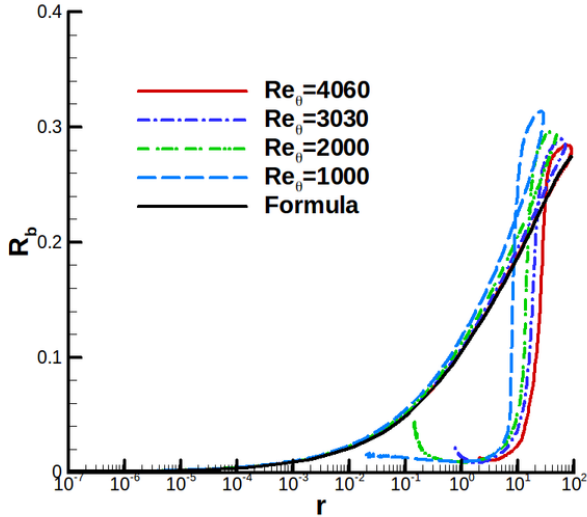


Figure 2: Stress intensity distributed in  $r$

ity ratio  $r = \mu_t/\mu$  are two non-dimensional parameters. The distributions of  $R_b$  versus  $Re_k$  and  $r$  are illustrated in Figure 1 and Figure 2. One interesting phenomenon is that there are discrepancies among the  $R_b$  profiles at different Reynolds numbers, but the profiles match each other very well when  $Re_k$  or  $r$  is small, in other words, Reynolds number effects are small for small  $Re_k$  or  $r$ .

In KDO model,  $R_b$  was calibrated by the DNS data of fully developed turbulent flat plate boundary layer at the slice  $Re_\theta = 4060$  (Schlatter and Orlu 2010). It is refined in this paper to be a basic formula for describing transition,

$$R_b = \min[0.018(Re_k/1)^{0.56} \times (1 + (Re_k/120)^{2.5})^{-0.56/2.5} \times (1 + (Re_k/225)^{10})^{0.05/10}, 0.283] \quad (3)$$

As stated in KDO model,  $Re_k$  contains the wall distance which stays fixed no matter how the fluid moves. That is why KDO presented transition behaviour in the

t3b flat plate boundary layer but the onset location was incorrect. The eddy viscosity ratio is a measurement of how strong the turbulence is, which is calculated all by transport variables. It is thus employed here,

$$R_b = \min[0.1165(r/1)^{0.37} \times (1 + (r/1)^{1.15})^{-0.157/1.15} \times (1 + (r + 72)^2)^{-0.213/2}, 0.283] \quad (4)$$

Equation (4) is the key for capturing transition, which will be shown in section 3.

As seen in Fig.1 and Fig.2, equation (3) and (4) agree very well with the DNS data at  $Re_\theta = 4060$ . They are ‘‘order functions’’. The concept of order function was proposed by She et al. (2009, 2015) to reformulate turbulence problems. The order function is a sub-concept of a new symmetry-based theory named structural ensemble dynamics (SED) (She et al. 2010). SED is one theory that quantifies multilayer structures of complex systems such as wall turbulence. The SED theory shows out that the multilayer structure is well described by a set of functions derived from an analysis of generalized Lie-group dilation invariance imposed by the presence of wall. Hence, the SED theory is very appropriate to describe the variation of  $R_b$  in boundary layer flows. Equation (4) can be rewritten as,

$$R_b = c_0(r/a_0)^{c_0/b_0} \prod_{i=1}^n (1 + (r/a_i)^{b_i})^{c_i/b_i} \quad (5)$$

Fig.3 may demonstrate that, the multilayer structure in boundary layer flows is described using multiple products. Fig.3 may demonstrate that, the multilayer structure in boundary layer flows is described using multiple products.

The turbulence transport equation with the least unclosed terms is the kinetic energy equation, which is the only governing equation in this work.

$$k_{,t} + (u_j k)_{,j} = -\overline{u'_t u'_j} U_{i,j} + [(\nu + \nu_t) k_{,j}]_{,j} - \epsilon \quad (6)$$

In the diffusion term,  $\nu_t = R_b k/S$  can be deduced from equation (2). The viscous dissipation term  $\epsilon$  is the most important unclosed term. The transport of turbulent variables can generate more unclosed higher order correlations, so  $\epsilon$  is closed algebraically rather than solving partial differential equations. According to KDO model,

$$\epsilon = \epsilon_1 + \epsilon_2 \quad (7)$$

$$\epsilon_1 = 2\nu\sqrt{k}_{,j}\sqrt{k}_{,j} \quad (8)$$

$$\epsilon_2 = A_\epsilon k^{3/2}/L \quad (9)$$

$$L = \sqrt{\Omega_i \cdot \Omega_i} / \sqrt{\nabla_j \Omega_i \cdot \nabla_j \Omega_i}, \quad \Omega_i = \epsilon_{ijk} U_{k,j} \quad (10)$$

Now the  $k$  equation formula is closed, but  $A_\epsilon$  the only empirical coefficient needs to be determined using DNS data on the slice of  $Re_\theta = 4060$ . The closure of  $\epsilon_2$  is the same with that in KDO model, but  $A_\epsilon$  is refined as, For  $Re_k < 10$ ,

$$\epsilon_2 = A_\epsilon k^{3/2}/d \quad (11)$$

$$A_\epsilon = 1.34(Re_k/0.25)^{-0.8} (1 + (Re_k/0.25)^{1.5})^{0.45/1.5} (1 + (Re_k/2.4)^{1.5})^{-0.1/1.5} \quad (12)$$

For  $Re_k \geq 10$ ,

$$\epsilon_2 = \min(A_\epsilon, 0.8) k^{3/2} \max(1/L, (1 - e^{-Re_k/1300})/d) \quad (13)$$

$$\begin{aligned}
A_\epsilon &= 1.4(Re_k/4.3)^{-1.9}(1 + (Re_k/4.3)^5)^{0.2/5} \\
&\quad (1 + (Re_k/28)^{4.9})^{2.76/4.9}(1 + (Re_k/66)^{10})^{-0.15/10} \\
&\quad (1 + (Re_k/110)^{10})^{0.12/10}(1 + (Re_k/175)^{10})^{-0.4/10}
\end{aligned} \tag{14}$$

The RANS system is finally closed. Most of the closures are based on physical analysis, but there are two parameters that cannot be constant, namely,  $R_b$  and  $A_\epsilon$ . In the original KDO model, both of them were composed of  $Re_k$  which is not able to entirely adapt itself according to the flow structure.  $R_b$  has been re-calibrated using eddy viscosity the “transport” parameter. Suppose that  $A_\epsilon$  and  $R_b$  as “boundaries” that determine the solution of KDO-RANS system, accurate  $R_b$  is able to arrive at accurate  $A_\epsilon$  although  $A_\epsilon$  contains the wall distance. Therefore, it is not necessary to re-calibrate and  $A_\epsilon$  with eddy viscosity ratio.

### 3 Benchmark tests

The original KDO model had exhibited transition behaviour in the T3B boundary layer, but the onset was ahead of the true location. Equation (4) re-calibrates  $R_b$  in terms of eddy viscosity ratio  $r$  that is presumably able to introduce transport effects and reproduce appropriate transition. Nevertheless, the utilization of  $r$  may cause numerical issues since the determination of eddy viscosity is recursive. An alternative approach is to partly employ equation (4), that is, to employ equation (4) when  $r$  is less than 1.0 and to employ equation (3) when  $r$  is no more than 1.0. When  $r$  exceeds 1.0, the turbulent eddy viscosity has reached the level of the local molecular viscosity, indicating the flow is turbulent or on the edge of turbulent. This approach guarantees that the flow is controlled by equation (4) before transition begins. The numerical simulation using this approach is termed as ‘Present’.

#### 3.1 T3A and T3B bypass transition

European Research Community on Flow Turbulence and Combustion (ERCOFTAC) conducted a series of flat plate boundary layer transition experiments (Savill 1993). T3A and T3B flat plate are chosen as the benchmark test case for bypass transition. The free-stream turbulence intensities are 3.3% and 6.5%, respectively. The mesh  $357 \times 101$  is used for both T3A and T3B. The simulations are presented in Figure 4 and Figure 5. It is clear that equation (4) provides accurate transition onset locations, but the skin friction is somewhat “wavy”. The performance of present approach is similar with that of equation (4), except that accuracy is improved by present approach. The results predicted by the  $\gamma - Re_\theta$  four-equation transition model in Ansys FLUENT are added as comparisons. For T3A boundary layer, present approach yields too short a transition region, failing to describe the transition process, while  $\gamma - Re_\theta$  yields a transition region that matches the experimental data very well. For T3B boundary layer, the inflow turbulent intensity is almost twice larger, inducing an early transition onset position and a very short transition region. Present approach agrees very well with the experiment in this situation, whereas  $\gamma - Re_\theta$  fails to capture the dive of skin friction on the transition onset location. Overall, for bypass transition, present approach is able to yield a reasonable transition onset, and is able to capture the peak of skin friction after transition. However, the transition region is too short, which

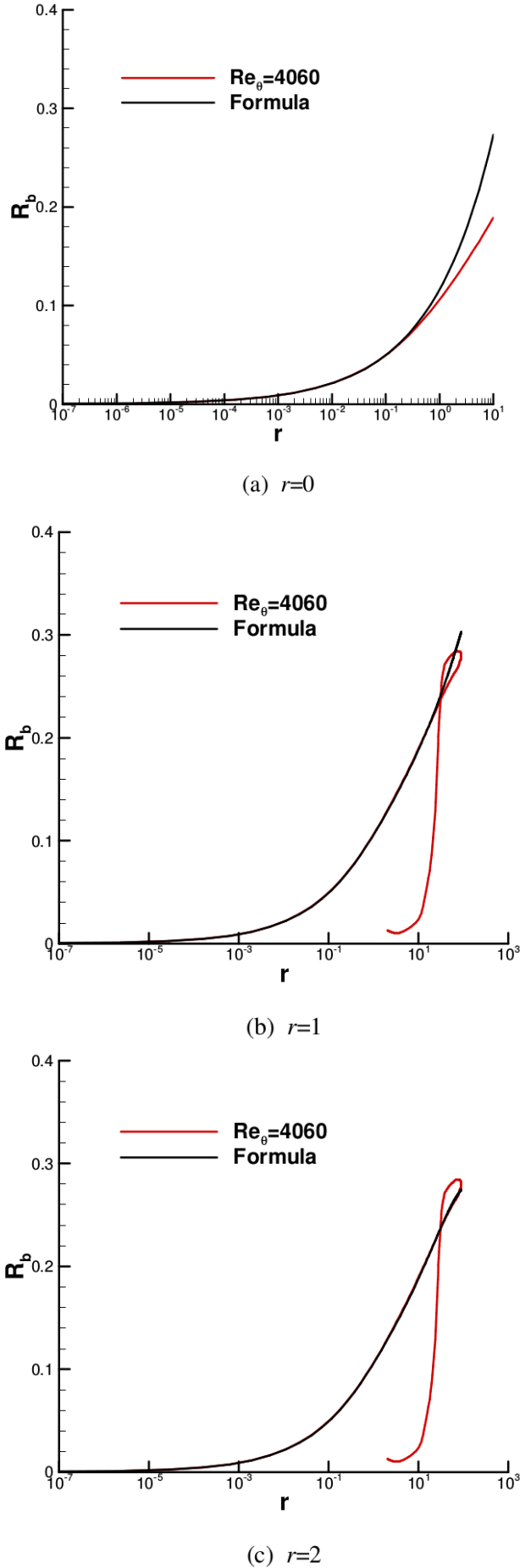


Figure 3: Calibrations of  $R_b$  using equation (5) with multiple products, in which “n” stands for the expressed layer number of wall turbulence structure

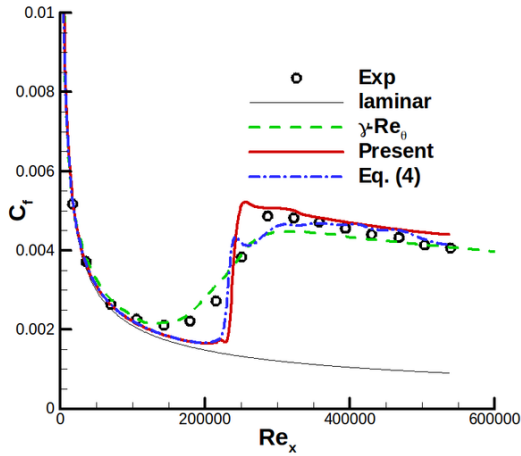


Figure 4: Skin friction on T3A flat plate

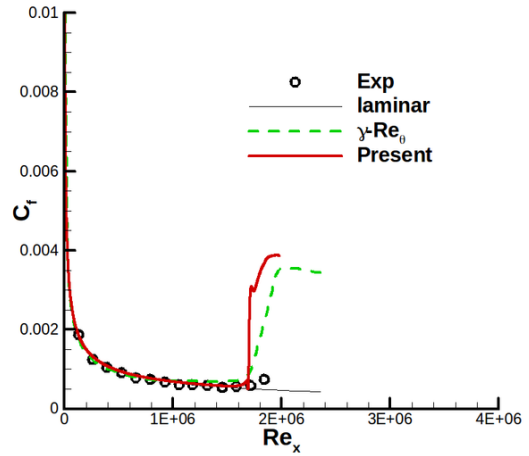


Figure 6: Skin friction on T3A- flat plate

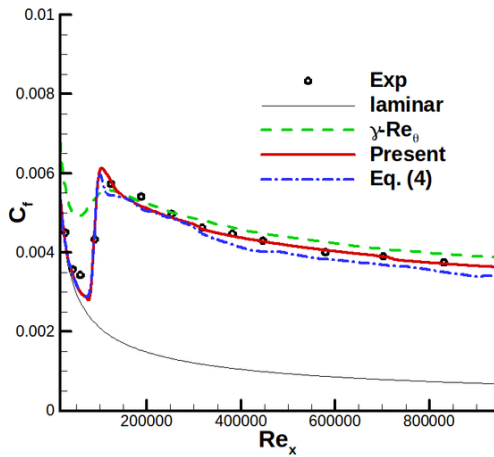


Figure 5: Skin friction on T3B flat plate

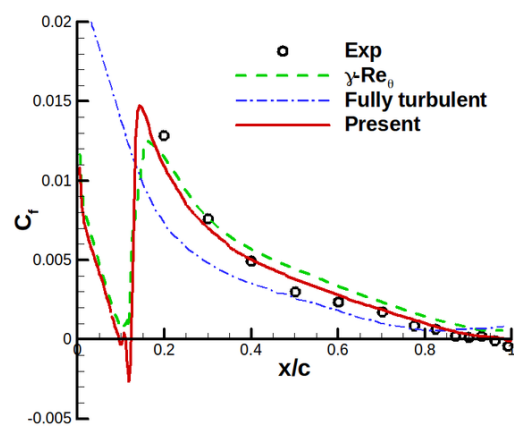


Figure 7: Skin friction on the suction surface of Aero-A airfoil

is probably due to two facts. First,  $R_b$  is calibrated by DNS data on the slice  $Re_\theta = 4060$ , so there are Reynolds number effects. Second, present approach only aims at regions before-transition onset, and thus the evolution of turbulence after transition onset has not been considered.

### 3.2 T3A- natural transition

Hereinafter, the results by equation (4) will not be shown. When the inflow turbulence intensity is small enough (e.g., less than 1%), after a critical Reynolds number, Tollmien-Schlichting instabilities appear and evolve to transition. This transition is named as natural transition. Low-Re turbulence models are recognized as being unable to reflect such mechanism. T3A- is one famous experiments used as the benchmark tests for natural transition, the inflow turbulence intensity was 0.874%. The mesh used for T3A- flat plate boundary layer is the same one used by T3A and T3B. For present approach, the skin friction profile in between laminar and fully turbulent region also mismatches the estimated profile of experiment, as shown in Figure 6. However, the onset of transition location is also reasonable, which is almost identical with that predicted by the  $\gamma - Re_\theta$  four-equation model.

### 3.3 Laminar separation-bubble transition

The Aero-A airfoil was experimentally studied by ON-ERA (Chaput 1997) in a wind tunnel of  $1.5m \times 3.5m$ . The experiment did not place any turbulators on the suction side. The Reynolds number based on the chord length  $c$  was  $2.07 \times 10^6$  and the inflow turbulence intensity was 0.2%. When the attack angle reached 13.1 degree, the boundary layer on the suction side was laminar at first, and then ended up with a laminar bubble at 12% $c$  because of the adverse pressure gradient. The bubble caused separation transition and developed into a turbulent boundary layer downstream. On the tail of the airfoil, turbulent separation happened due to the strong adverse pressure gradient. The geometry is simple but generated several types of complex flows. For CFD simulations, the mesh is composed of multi-blocks. The total number of cells is 66,156. The skin friction on the suction surface of the airfoil is presented in Figure 7. It is clear that both  $\gamma - Re_\theta$  and present approach have captured the transition onset location. Present approach has also captured the laminar separation bubble and the turbulent separation on the tail, which correspond to negative skin friction values.

## 4 Summary

Laminar-turbulent transition is a scientific and practical challenge for RANS system. The key is the closure of unknown Reynolds stresses. There are only two sources for the supplement of missing information. One is physical analysis/phenomenological theory; the other is a combination of transition mechanisms expressed in empirical formulations and coefficients, which are extracted from typical flows. The author tends to adopt the first source more, leading to RANS closure approach based on turbulent kinetic energy.

The governing equation for turbulent kinetic energy is directly derived from Navier-Stokes equations and contains the least unclosed terms. This work dedicates itself to reliable elements for the closure. Two kernel closure theories are employed. One is the direct cascade of turbulent kinetic energy to viscous dissipation, in which von Karman length scale is employed as the characteristic scale in the process. The dissipation term closed is thus flow-structure-adaptive. The other is an extension of Bradshaw's assumption, which has been extensively verified. With the extended Bradshaw's assumption, the turbulent principal shear stress depends on turbulent kinetic energy only, which induces a reconstruction of the Reynolds stress constitutive relation. The new relation has evaded the difficulties in seeking relations between Reynolds stresses and mean strains, which not only reduces the number of empirical coefficients but also implicitly accounts for many physics such as geometry effects and non-locality.

Two empirical coefficients induced by the closures determine whether the system is able to reproduce transition phenomena. One is the parameter of the dissipation term; the other is stress intensity ratio. Both of them were taken from fully turbulent boundary layer at  $Re_\theta = 4060$ . This work re-calibrates stress intensity ratio with turbulence intensity ratio, which is an implicit transport parameter. With this improvement, the new closure approach is able to reproduce bypass transition, natural transition and separation bubble induced transition. The precise processes of the laminar-turbulent flow transition are not described, but the transition onset locations and the peaks of skin friction after transition are well captured. This is due to Reynolds number effects, since the calibration uses only one slice of the flat plate boundary layer. The determination of the two empirical coefficients calls for more ideas. However, this work has demonstrated that a RANS system is able to reproduce transition phenomena, as long as the fidelity of the closure approach is high enough. The closure does not include any transition mechanisms such as TS wave instability. Along with the evolution of the turbulent transport equations, transition phenomena naturally appear, which is similar to what Navier-Stokes equations do. Maybe this is the mechanism for the closure approach to capture bypass, natural and separation bubble transitions.

## Acknowledgements

This work was supported by the National Natural Science Foundation of China (No.11002014). For any commercial use of KDO-transition closure approach, please contact Dr. Xu (xujl@buaa.edu.cn).

## References

- Chapu, E. (1997), Chapter 3: Application-Oriented Synthesis of Work Presented in Chapter II, Notes on Numerical Fluid Mechanics, Vieweg Verlag, Braunschweig, Germany, 58, pp.327-346.
- Chen, W., Lien, F. and Leschziner, M. A. (1998), Non-linear eddy-viscosity modelling of transitional boundary layers pertinent to turbomachine aerodynamics, *Int. J. Heat Fluid Flow*, Vol. 19, pp.297-306.
- Dhawan, S. J. and Narasimha, R. (1958), Some properties of boundary layer flow during the transition from laminar to turbulent motion, *J. Fluid Mech.*, Vol. 3, Issue 04, pp.418-436.
- Van Ingen, J. L. (1956), A Suggested Semi-Empirical Method for the Calculation of the Boundary Layer Transition Region, Delft Univ. of Technology, Rept. VTH-74, Delft, The Netherlands.
- Krumbein, A., Krimmelbein, N. and Schrauf, G. (2010), Automatic Transition Prediction for Three Dimensional Aircraft Configurations Using the DLR TAU Code, *New Results in Numerical and Experimental Fluid Mechanics VII*. Springer Berlin Heidelberg, pp.101-108.
- Langtry, R. B. and Menter, F. R. (2009), Correlation-based transition modeling for unstructured parallelized computational fluid dynamics codes, *AIAA J.*, Vol. 47, Issue 12, pp.2894-2906.
- Lardeau, S., Fadai-Ghotbi, A. and Leschziner, M. A. (2009), Modelling bypass and separation-induced transition by reference to pre-transitional fluctuation energy, *ERCOFTAC Bull.'Transition Modelling'*, 80, pp.72-76.
- Lardeau, S., Leschziner, M. A. and Li, N. (2004), Modelling bypass transition with low Reynolds number non-linear eddy-viscosity closure, *Flow Turbul. Combust.*, Vol. 73, Issue 1, pp.49-76.
- Lardeau, S. and Leschziner, M. A. (2006), Modeling of wake-induced transition in linear low-pressure turbine cascades, *AIAA J.*, Vol. 44, Issue 8, pp.1854-1865.
- Mayle, R. E. and Schulz, A. (1997), Heat transfer committee and turbomachinery committee best paper of 1996 award: The path to predicting bypass transition, *J. Turbomach.*, Vol. 119, Issue 3, pp.405-411.
- Menter, F. R., Langtry, R. B., Likki, S. R., Suzen, Y. B., Huang P. G. and Váülker S. (2006), A correlation-based transition model using local variables-Part I: model formulation, *J. Turbomach.*, Vol. 128, Issue 3, pp.413-422.
- Palikaras, A., Yakinthos, K. and Goulas, A. (2002), Transition on a flat plate with a semi-circular leading edge under uniform and positive shear free-stream flow, *Int. J. Heat Fluid Flow*, Vol. 23, pp.455-470.
- Savill, A. M. (1993), Evaluating turbulence model predictions of transition, *Advances in Turbulence IV*. Springer Netherlands, pp.555-562.
- Schlatter, P. and Orlu, R. (2010), Assessment of Direct Numerical Simulation Data of Turbulent Boundary Layers, *J. Fluid Mech.*, Vol. 659, pp.116-126.
- She Z. S., Chen, X., Wei, B. B., Zou, H. Y. and Bi, W. T. (2015), SED-based studies of turbulence models for wall flows (in Chinese), *Sci. Sin-Phys. Mech. Astron.*, Vol. 45, 124703, pp.1-16.

- She, Z. S., Chen, X., Wu, Y. and Hussain, F. (2010), New perspective in statistical modeling of wall-bound compute-8-13.local ed turbulence, *Acta Mech. Sin.*, Vol. 26, Issue 6, pp. 847-861.
- She, Z. S., Hu, N. and Wu, Y. (2009), Structural ensemble dynamics based closure model for wall-bounded turbulent flow, *Acta Mech. Sin.*, Vol. 25, Issue 5, pp.731-736.
- Smith, A. M. O. and Gamberoni, N. (1956), Transition, Pressure Gradient and Stability Theory, Douglas Aircraft Co., Rept. ES-26388, Long Beach, CA.
- Suzen, Y. B. and Huang, P. G. (2000), Modeling of flow transition using an intermittency transport equation, *J. Fluids Eng.*, Vol. 122, Issue 2, pp. 273-284.
- Suzen, Y. B., Huang, P. G., Hultgren, L. S. and Ashpis D. E. (2003), Predictions of separated and transitional boundary layers under low-pressure turbine airfoil conditions using an intermittency transport equation, *J. Turbomach.*, Vol. 125, Issue 3, pp.455-464.
- Volino, R. J. and Simon, T. W. (1997), Boundary layer transition under high free-stream turbulence and strong acceleration conditions: part 2-turbulent transport results, *J. Heat Transf.*, Vol. 119, Issue 3, pp.427-432.
- Walters, D. K. and Cokljat, D. (2008), A three-equation eddy-viscosity model for Reynolds-averaged Navier-Stokes simulations of transitional flow, *J. Fluids Eng.*, Vol. 130, Issue 12, 121401, pp.1-14.
- Xu, J., Zhang, Y. and Bai, J. (2015), One-equation turbulence model based on extended bradshaw assumption, *AIAA J.*, Vol. 53, Issue 6, pp.1433-1441.

# PREDICTION OF BYPASS AND SEPARATION-INDUCED TRANSITION WITH AN ALGEBRAIC INTERMITTENCY MODEL

S. Kubacki<sup>1</sup>, T. Borzecki<sup>2</sup>, E. Dick<sup>3</sup>

<sup>1</sup>*Institute of Aeronautics and Applied Mechanics, Warsaw University of Technology,  
Nowowiejska 24, 00-665, Warsaw, Poland*

<sup>2</sup>*Avio Aero, Grazynskiego 141, 43-300 Bielsko-Biala*

<sup>3</sup>*Department of Flow, Heat and Combustion Mechanics, Ghent University,  
St.-Pietersnieuwstraat 41, 9000 Ghent, Belgium*

Slawomir.Kubacki@meil.pw.edu.pl

## Abstract

The paper discusses applications of an algebraic intermittency model for prediction of bypass and separation-induced boundary layer transition. The transition model is coupled with a  $k-\omega$  turbulence model. The transition model uses only local variables and is tuned for turbomachinery flows. For bypass transition, two effects in an attached pre-transitional boundary layer are modelled: damping of small-scale disturbances induced by the free stream and breakdown of the near-wall perturbed flow with generation of fine-scale turbulence. For separated flow, the model describes breakdown of a laminar free shear layer. We refer to [1] for a complete discussion of the modelling assumptions and the model validation.

## 1 Transition mechanisms

Transition mechanisms in an attached laminar boundary layer subjected to a high free-stream turbulence level (above 0.5-1%) are discussed by Hack and Zaki [2]. Streamwise elongated disturbances are generated. These are zones of forward and backward jet-like perturbations, alternating in spanwise direction. They are called streaks or Klebanoff disturbances. Streaks grow downstream both in length and amplitude and finally some streaks cause turbulent spots. Transition is then called by bypass type, which means that instability by Tollmien-Schlichting waves is bypassed. Breakdown is then earlier and much faster. Klebanoff modes are initiated by deep penetration into a laminar boundary layer of large-scale perturbations from the free stream. The strong damping of small-scale components is called shear sheltering. There are at least two instability mechanisms in a boundary layer perturbed by streaks. One is instability by inflection of the velocity profile in wall-normal direction between the boundary layer edge and a low-speed streak. The other is instability of the velocity profile in wall-normal direction in the overlap zone of the leading edge of a high-speed streak and the trailing edge of a low-speed streak. Both instabilities are triggered by small-scale perturbations, although these are damped in the boundary layer

Transition mechanisms in a separated laminar boundary layer are discussed by McAuliffe and Yaras [3]. Under low free-stream turbulence, transition is initiated by inviscid Kelvin-Helmholtz instability, with formation of spanwise vortices. They group at selective streamwise wavelengths, analogous to Tollmien-Schlichting waves in an attached boundary layer. The roll-up vortices

break down as they travel downstream. The breakdown process is rather slow with low free-stream turbulence, but, under high free-stream turbulence, bypass transition with formation of streaks in the attached boundary layer prior to separation can co-exist with the Kelvin-Helmholtz generated spanwise vortices in the separated layer. The breakdown of the vortex rolls is then strongly accelerated by perturbations due to the Klebanoff modes. For sufficiently strong free-stream turbulence, the Kelvin-Helmholtz instability may even be bypassed by the breakdown of the streaks. So, a bypass mechanism is possible in a separated shear layer, similar as in an attached boundary layer.

## 2 Model formulation

The transport equations for turbulent kinetic energy and specific dissipation read

$$\frac{Dk}{Dt} = \gamma P_k + (1 - \gamma)P_{sep} - \beta^* k\omega + Diff(k) \quad (1)$$

$$\frac{D\omega}{Dt} = \alpha \frac{\omega}{k} P_k - \beta\omega^2 + Diff(\omega) \quad (2)$$

The basic equations are the  $k-\omega$  equations of the turbulence model of Wilcox [4], but there are three modifications in the production terms. In the original model, production of turbulent kinetic energy by turbulent shear is  $P_k = \nu_T S^2$ , with  $\nu_T$  the full eddy viscosity and  $S = (2S_{ij}S_{ij})^{1/2}$  the magnitude of the shear rate tensor. Firstly, this production term is written as  $P_k = \nu_s S^2$ , where  $\nu_s$  is the small-scale eddy viscosity, which is part of the full eddy viscosity  $\nu_T$ . Secondly, the production term  $P_k$  is multiplied with an intermittency factor  $\gamma$  which is zero in laminar flow and unity in turbulent flow. Thirdly, the term  $(1 - \gamma)P_{sep}$  is added to the production term of the  $k$ -equation. This term models turbulence production by instability and breakdown of a laminar free shear layer in a low turbulence level background flow.

The turbulent kinetic energy  $k$  is split, based on the laminar-fluctuation kinetic energy transition model of Walters and Cokljat [5], into a small-scale part and a large-scale part:

$$k_s = f_{SS}k, \quad k_l = k - k_s \quad (3)$$

The splitting by the factor  $f_{SS}$  expresses the shear-sheltering effect in a pre-transitional boundary layer. Small-scale disturbances in the turbulent flow near to the

laminar part of the layer are damped. Only large-scale disturbances penetrate deeply into the laminar layer, but these do not contribute to turbulence production by shear but induce the streaks. The restriction of the turbulence production by turbulent shear to small-scale fluctuations is expressed by replacing the full eddy viscosity by a small-scale eddy viscosity in the production terms of the  $k$ - and  $\omega$ -equations (Eqs. 1 and 2).

Shear-sheltering depends on the ratio of two timescales in a laminar layer: the timescale of convection of disturbances relative to an observer inside the layer and the timescale of diffusion in the normal direction. Walters [6] estimates the convective time scale by the time scale of the strain,  $\tau_c = 1/\Omega$ , with  $\Omega$  the magnitude of the vorticity tensor. The diffusive time scale in a laminar layer is fundamentally  $l^2/\nu$ , with  $l$  the fluctuation length scale in normal direction and  $\nu$  the kinematic fluid viscosity. Walters [6] expresses damping of small-scale fluctuations in a pre-transitional boundary layer by stating that fluctuations in the border zone of the laminar and turbulent parts synchronise strongly with the mean velocity gradient in the laminar part. So, he assumes that fluctuations, both in streamwise and in wall-normal direction, after damping, scale with  $l\Omega$ . This means proportionality between  $\sqrt{k}$  and  $l\Omega$ , resulting in  $l \propto \sqrt{k}/\Omega$  and  $\tau_d \propto k/(\nu\Omega^2)$ . The ratio of the diffusive and convective timescales is the Reynolds number  $Re_\Omega = k/(\nu\Omega)$ .

With the supplementary assumption that in the laminar part of a pre-transitional boundary layer the wall-normal fluctuation length scale is proportional to the distance to the wall, denoted by  $y$ ,  $\Omega$  may be eliminated by replacing it by  $\sqrt{k}/y$ . This means that the characteristic Reynolds number for shear-sheltering may also be  $Re_y = \sqrt{ky}/\nu$ . We use the shear-sheltering factor of Walters and Cokljat [5], but replace  $Re_\Omega$  by  $Re_y$ , leading to

$$f_{SS} = \exp\left(-\left(\frac{C_{SS}\nu}{\sqrt{ky}}\right)^2\right) \quad (4)$$

$C_{SS} = C_S(1 + C_A f_W \Psi)$  is a flow-dependent coefficient.  $C_S$  and  $C_A$  are constants (Table 1).  $C_A$  is set to unity while  $C_S$  has been determined by simulations of T3C flat plate flows of ERCOFTAC (not disused here). The  $\Psi$  and  $f_W$  functions are:

$$\Psi = \tanh\left(\frac{-\Omega(S - \Omega)}{C_\Psi(\beta^*\omega)^2}\right), \quad f_W = 1 - \tanh\left(\frac{k}{C_W\nu\omega}\right) \quad (5)$$

The role of the flow-dependent term  $f_W\Psi$  is increasing  $C_{SS}$  (larger shear sheltering) in accelerating flow ( $f_W\Psi > 0$ ), and reducing  $C_{SS}$  (smaller shear sheltering) in decelerating flow ( $f_W\Psi < 0$ ), due to streamline curvature. The  $\Psi$  function is the curvature sensor from the non-linear eddy-viscosity turbulence model of Khodak and Hirsch [7]. The  $f_W$  function limits the correction to the border zone between laminar and turbulent parts in a pre-transitional boundary layer. The  $C_W$  and  $C_\Psi$  are positive constants, determined by simulations of flows through the N3-60 steam turbine cascade and the V103 compressor cascade. We discuss simulations of the N3-60 cascade later.

The eddy viscosity associated to small scales is calculated in the same way as the eddy viscosity of the original turbulence model [4] by replacing  $k$  by  $k_s$ :

$$\nu_s = \frac{k_s}{\tilde{\omega}}, \text{ with } \tilde{\omega} = \max\left[\omega, \frac{C_{lim}S}{a_s}\right] \quad (6)$$

The constant  $a_s$  is set to 0.3 and  $C_{lim} = 7/8$ , which are the standard values. The large-scale eddy viscosity, is,

similarly defined with  $k_l$ :

$$\nu_l = \frac{k_l}{\tilde{\omega}}, \text{ with } \tilde{\omega} = \max\left[\omega, \frac{C_{lim}S}{a_l}\right] \quad (7)$$

The constant  $a_l$  is set to 0.6, which is larger than the standard value 0.3. The resulting eddy viscosity, used in the Navier-Stokes equations, is  $\nu_T = \nu_s + \nu_l$ . The reason for the enlarged value of  $a_l$  with respect to  $a_s$  is earlier transition due to increased instability of a laminar flow perturbed by streaks under an adverse pressure gradient. The values of the  $a_l$  and  $C_W$  constants (Table 1) have been modified somewhat with respect to the values used in [1]. This change is the result of further model calibration on an extended number of cases.

The intermittency function  $\gamma$  determines when a flow region is laminar or turbulent. The free stream is turbulent. Thus  $\gamma$  is set to unity in the free stream. At a wall, the flow is laminar. Hence,  $\gamma$  is set to zero there.  $\gamma$  is prescribed algebraically as a function of the distance to the wall by

$$\gamma = \min\left(\max\left(\frac{\sqrt{ky}}{A_\gamma\nu} - 1, 0\right), 1\right) \quad (8)$$

where  $A_\gamma$  is a constant.

The motivation for  $Re_y = \sqrt{ky}/\nu$  as non-dimensional distance to the wall (Eq. 8) originates from the work of Wang et al. [11], who observed that breakdown occurs when, near to the wall, the ratio of turbulent shear stress to wall shear stress reaches a critical value. Near to a wall, the streamwise fluctuation  $u'$  in a pre-transitional boundary layer is caused by streaks. So, we may assume that near to a wall  $u'$  scales with  $y\Omega$ . Near to a wall, turbulent kinetic energy is strongly damped and with a turbulence model  $\sqrt{k}$  becomes representative for  $v'$ . So, the near-wall turbulent shear stress, obtained by multiplying  $u'$  by the wall-normal fluctuation  $v'$  and time-averaging, can be estimated by  $-\rho \langle u'v' \rangle \propto \rho y\Omega\sqrt{k}$ . The wall shear stress is  $\tau_w = \rho\nu\Omega_w$ . So, the ratio of both terms gives the characteristic Reynolds number  $Re_y = \sqrt{ky}/\nu$ .

The intermittency function is somewhat simplified with respect to the function of our previous work [8] by equalising the threshold value  $C_T$  and the growth rate  $A_T$  ( $C_T = A_T = A_\gamma$ ), but this is not a significant change. A more significant change concerns the shear-sheltering factor (Eq. 4). We used the factor from the model by [5] with  $Re_\Omega$  as input parameter in our previous work [8]. In [1] we replaced  $Re_\Omega$  by  $Re_y$ , such that  $f_{SS}$  is now also dependent on the distance to the wall, normalised in the same way as in the intermittency function. This change improves much the correspondence between predictions of the onset of transition by the model and empirical correlations (improved results are not shown here; consult Figs. 8 and 9 in [8] for previous results and Figs. 9 and 10 in [1] for new results).

The present model, in contrast to our previous version, includes turbulence production due to breakdown of a laminar separated boundary layer at low free-stream turbulence level using 2D RANS (or 2D/3D URANS). This is realised by the term  $(1 - \gamma)P_{sep}$  in the  $k$ -equation (Eq. 1). For,  $P_{sep}$  we adopt a term with the same purpose in the newest intermittency-transport transition model by Menter et al. [9]:

$$P_{sep} = C_{sep}F_{sep}\nu S^2 \quad (9)$$

$$F_{sep} = \min\left(\max\left(\frac{R_V}{2.2A_V} - 1, 0\right), 1\right) \quad (10)$$

Table 1: Transition model constants

$A_\gamma$	$C_S$	$C_A$	$C_\psi$	$C_W$	$C_{sep}$	$A_V$	$a_1$
12.0	21.0	1.0	10.0	10.0	2.0	550.0	0.6

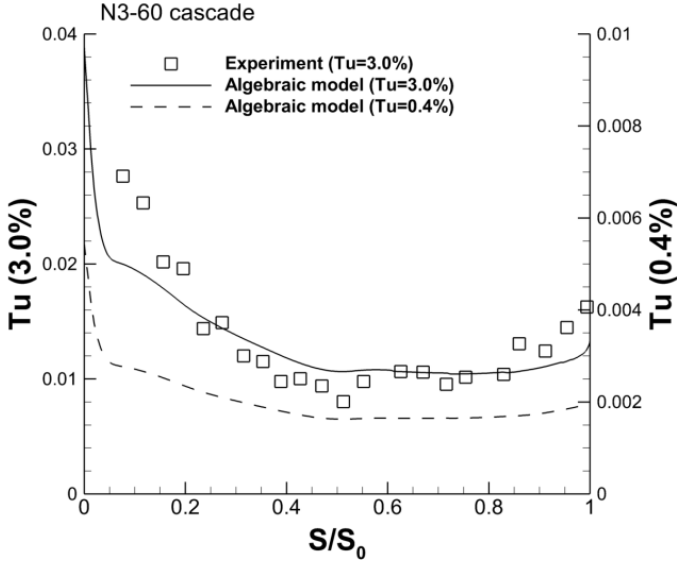


Figure 1: N3-60 cascade. Turbulence intensity along the suction side of the blade at distance 10 mm from the blade surface for  $Tu = 3\%$  and  $Tu = 0.4\%$ .  $S_0$  is the length of the suction side of the blade

with  $R_V = y^2 S / \nu$ . The constants  $C_{sep}$  and  $A_V$  have been calibrated for the T3C4 flat plate flow of ERCOFTAC, which is characterized by laminar boundary layer separation in the rear part of the plate (result are not shown). Table 1 lists the model constants.

### 3 Computational aspects

All simulations reported here are for the N3-60 steam turbine cascade using 2D RANS or 2D URANS. The 2D computational grids, with about  $1.1 \cdot 10^5$  cells, consist of a structured boundary layer part with quadrilateral cells near to walls and an unstructured part away from walls. The grid is refined near to walls. The  $y^+$  parameter varies between 0.1 and 0.8 along walls and about 40 cells are used across the boundary layer grid part.

### 4 N3-60 cascade with steady inflow

We discuss the model performance for transition in attached and in laminar separation states by 2D RANS for steady inflow of the N3-60 cascade, measured by Zarzycki and Elsner [10]. The N3-60 profile is the enlarged profile of a stator vane in the high-pressure part of a steam turbine. Geometric data are: blade chord 300 mm, axial blade chord 203.65 mm, blade pitch 240 mm. The exit Reynolds number is  $6 \cdot 10^5$ . Measurements are available for inflow turbulence  $Tu = 3\%$  and  $Tu = 0.4\%$  in the leading edge plane. Laminar separation occurs at the suction side for  $Tu = 0.4\%$

At the inlet to the computational domain, placed at 0.344 times the axial chord length upstream of the lead-

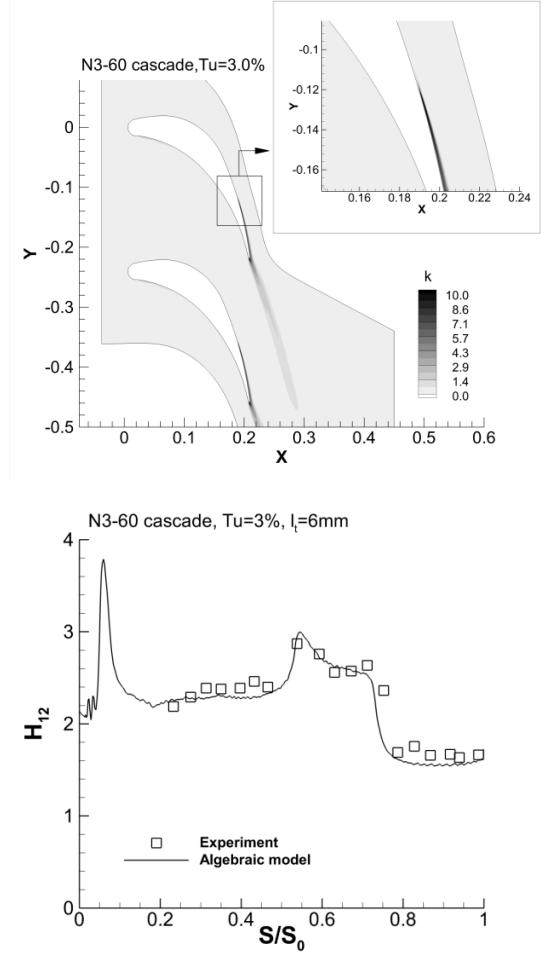


Figure 2: N3-60,  $Tu = 3\%$ . Turbulent kinetic energy (top) and shape factor along the suction side of the blade (bottom) using 2D RANS

ing edge, a uniform flow velocity in the axial direction was imposed. The inlet turbulence intensity in the leading edge plane was set according to the two sets of experimental data. The inlet turbulent length scale was not reported in the measurements. For  $Tu = 3\%$ , the inlet turbulent length scale was adjusted by matching the measured turbulence intensity at a distance of 10 mm from the blade surface (this is above the boundary layer edge). The obtained turbulent length scale is  $l_t = 6$  mm for  $Tu = 3\%$ . Fig. 1 shows that the agreement between prediction and measurement is reasonably good, which means that the inlet conditions for the modelled scalars have been set correctly. For low turbulence level at inlet ( $Tu = 0.4\%$ ), the evolution of the free-stream turbulence along the blade surface is not available in the database. We assume a smaller length scale ( $l_t = 2$  mm) at the entrance to the cascade than for high inlet turbulence level since no turbulence grid was installed in the reference experiment. The turbulent intensity reproduced at the leading edge of the blade corresponds with measurements,  $Tu = 0.5-0.4\%$  (Fig. 1).

Fig. 2 shows the contour plot of turbulent kinetic energy for  $Tu = 3\%$  and the comparison between computed and measured shape factor  $H_{12}$  along the suction side of the blade. The simulated transition comes from the bypass term  $\gamma P_k$  in Eq. 1. Transition onset, at  $S/S_0 = 0.75$ , and growth rate in the transition zone are reproduced correctly by the model.

Fig. 3 shows the contour plot of turbulent kinetic energy for  $Tu = 0.4\%$  and the comparison between com-

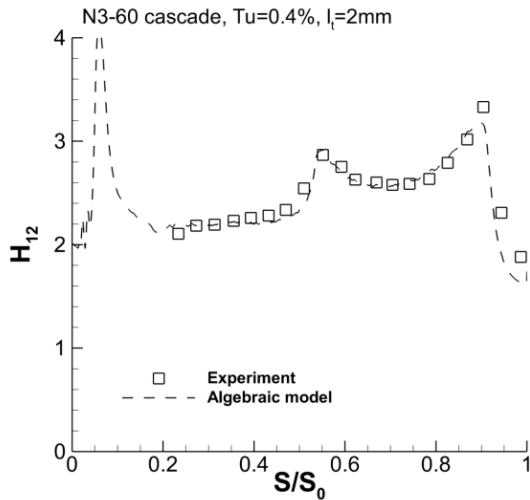
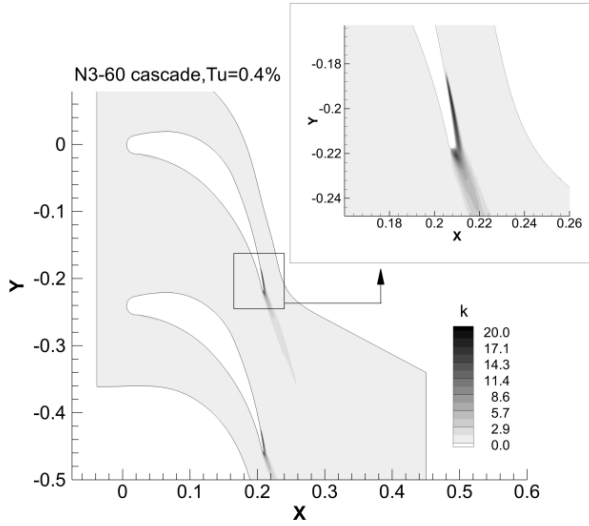


Figure 3: N3-60,  $Tu = 0.4\%$ . Turbulent kinetic energy (top) and shape factor along the suction side of the blade (bottom) using 2D RANS

puted and measured shape factor  $H_{12}$  along the suction side of the blade. The simulated transition comes here from the separation term  $(1 - \gamma)P_{sep}$  in Eq. 1. Start of transition is observed at  $S/S_0 = 0.9$ . The agreement between simulation and measurement is good. It means that the model calibration for separation-induced transition by the T3C4 case has been done well. We bring to the attention that in the previous model [8] the transition in a separated laminar boundary layer was not modelled, but was resolved using 3D URANS. This is no longer necessary, as transition in a separated boundary layer is fully modelled now [1].

## 5 N3-60 cascade with unsteady inflow

The final model validation is performed with wake-induced transition for flow through the N3-60 cascade using 2D URANS. Simulation results are compared with measurements by Zarzycki and Elsner [10]. In the experiments the wake generator was a wheel of pitch diameter  $D_p = 1950$  mm with cylindrical bars rotating in a plane perpendicular to the flow direction. The bars were spaced by  $b_s = 204$  mm on the pitch circle. The axial distance between the bars and the leading edge of the

blades was 0.344 of the axial blade chord. The frequency of the incoming wakes was  $f_d = 59$  Hz, with inflow velocity  $U_0 = 10$  m/s, resulting in the reduced frequency:  $St = f_d b_s / U_0 = 1.22$ . The exit Reynolds number was  $6 \cdot 10^5$ . The free-stream turbulence intensity  $Tu$  was controlled with a movable grid upstream of the cascade entrance. We use the data for bar diameters  $d=6$  and  $4$  mm with inflow turbulence levels  $Tu = 3$  and  $0.4\%$ , respectively. The inlet to the computational domain is placed at 0.17 times the axial chord length upstream of the leading edge. The effect of the moving bars was superimposed on the flow obtained from the steady calculation. The bar pitch has been increased to 240 mm to be equal to the blade pitch in the calculation. The bar velocity has been adjusted, so that the reduced frequency ( $St$ ) of the impacting wakes is unchanged. 800 time steps were used per wake period. Self-similar profiles for velocity and turbulent kinetic energy were imposed at the inlet:

$$U = U_\infty - (U_\infty - U_{center}) \exp \left[ -(\ln 2) \left( \frac{y}{y_{1/2}} \right)^2 \right],$$

$$k = k_\infty + (k_{center} - k_\infty) \exp \left[ -(\ln 2) \left( \frac{y}{y_{1/2}} \right)^2 \right] \quad (11)$$

In the above expressions,  $y$  is the distance perpendicular to the wake with  $y = 0$  the centre of the wake and  $y_{1/2}$  is the position where the defect of the velocity attains half of its maximum value. The parameters in the above expressions have been fitted to experimental data for wakes of stationary bars. The specific dissipation at the inlet was imposed following Wilcox [12]:

$$\omega = \omega_\infty + C_\mu^{1/4} \frac{\sqrt{k}}{l_{mix}}, l_{mix} = 0.18 y_{1/2} \quad (12)$$

The background dissipation  $\omega_\infty$  has been used to adjust the evolution of the fluctuating velocity component parallel to the blade,  $u' = (2k/3)^{1/2}$ , at distance 10 mm from the suction surface of the blade to the experimental one for moving bars (results are not shown).

Fig. 4 shows the perturbation velocity vectors in every 15 cells. The perturbation velocity field is obtained by subtracting the time-averaged velocity field from the instantaneous velocity field. Clearly, the  $1.1 \times 10^5$  mesh is sufficient to properly reproduce the negative jet effect caused by a moving wake.

Fig. 5 shows space-time diagrams of shape factor obtained in the experiment (a) and in the simulation (b) for wake-induced transition with background turbulence level  $Tu = 3\%$  ( $d = 6$ mm). The two straight lines mark the path of the moving wake. The wake position was determined from the free-stream velocity at the edge of the boundary layer. The bottom line is the path of the leading edge of the wake, determined as the position at which local flow acceleration starts in the rear part of the blade ( $S/S_0 > 0.6$ ). The upper line corresponds to the central part of the moving wake, determined as the start of local flow deceleration.

The agreement between simulation and measurement is very good under the wake impact ( $S/S_0 = 0.6$ ,  $\tau/T = 0.2$ ). The width of the turbulent zone is somewhat too large at  $S/S_0 = 0.7-0.8$  and the transition is reproduced somewhat too late in between wakes near to the trailing edge ( $S/S_0 = 0.9$ ,  $1.0 < \tau/T < 1.2$ ).

Fig. 6 shows space-time diagrams of shape factor for wake-induced transition with background turbulence

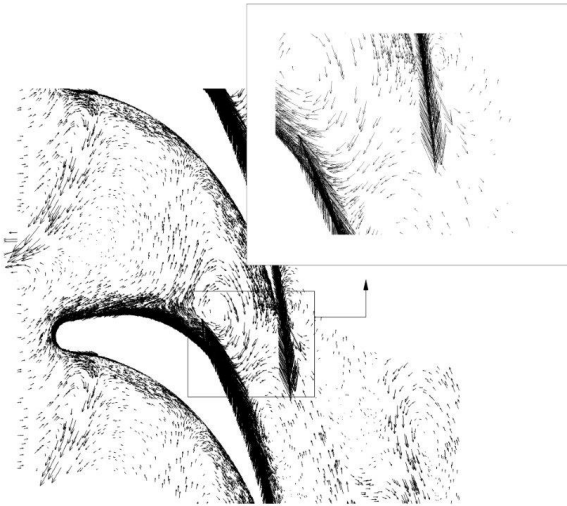


Figure 4: Negative jet visualised by perturbation velocity vectors in every 15 cells for 2D URANS

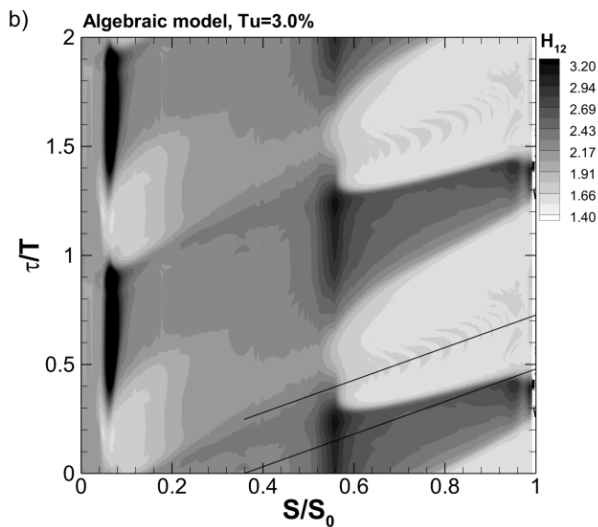
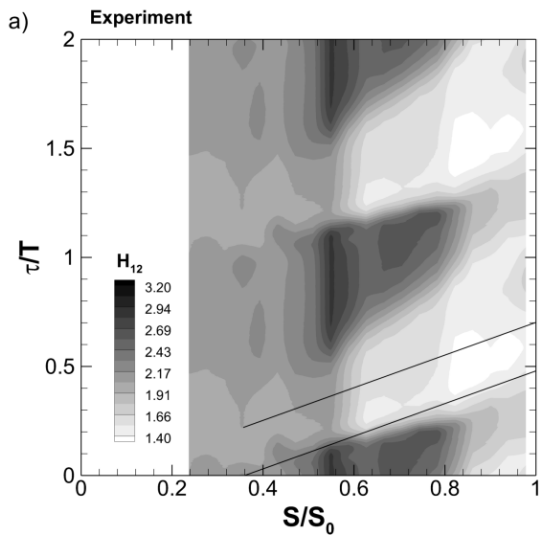


Figure 5: N3-60 cascade, bar diameter 6 mm and background turbulence level 3 %. Space-time diagrams of shape factor, a) experiment, b) simulation

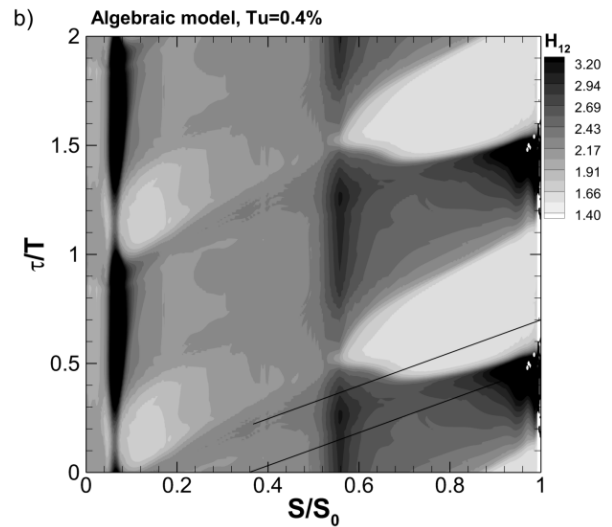
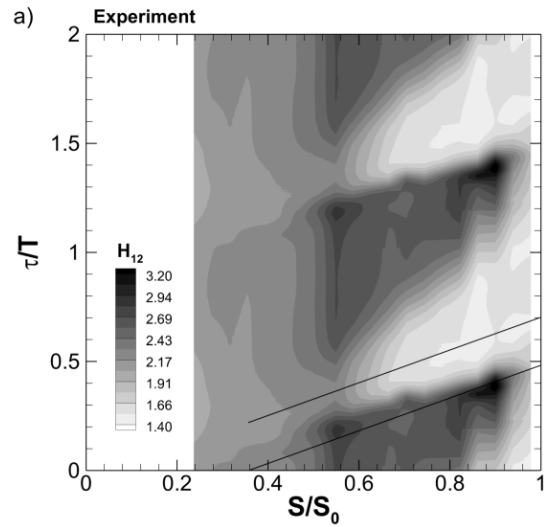


Figure 6: N3-60 cascade, bar diameter 4 mm and background turbulence level 0.4 %. Space-time diagrams of shape factor, a) experiment, b) simulation

level  $Tu = 0.4\%$  ( $d = 4\text{mm}$ ). The model is able to properly detect transition onset under the wake impact ( $S/S_0 = 0.7, \tau/T = 0.4$ ). The width of the turbulent zone, after wake impact, is comparable in both simulation and measurement. The quality of the model becomes less in between wakes ( $S/S_0 = 0.9, 1.1 < \tau/T < 1.5$ ) near to the trailing edge of the blade. The model predicts flow separation, which is not present in the experiment. The explanation is the somewhat too low free-stream turbulence level reproduced in the simulation in the rear part of the blade, which causes delayed transition there. In the experiment, interaction occurs near the suction side trailing edge between the wake of the adjacent blade and the moving wake through the blade passage. Vortices are shed from the blade wake, which break down, causing increased free-stream turbulence. This interaction is not detected in the 2D URANS simulation.

Overall, the simulation results of wake-induced transition both at high ( $Tu = 3\%$ ) and low ( $Tu = 0.4\%$ ) background turbulence levels are good using the present algebraic transition model.

## 6 Conclusions

Applications of an algebraic intermittency model have been presented. The model produces good results for bypass and separation-induced transition (2D RANS) and for wake-induced transition (2D URANS), for flow through the stream turbine vane cascade N3-60, at both high and low free-stream turbulence levels.

### Acknowledgement

The first and second author acknowledge support from the research project COOPERNIK financed partly by the Polish National Centre for Research and Development (INNOLOT/I/11/NCBR/2014) and partly by Avio Polska Sp. z o.o.

### References

- [1] Kubacki S., Dick E., An algebraic intermittency model for bypass, separation-induced and wake-induced transition. To appear in: *Int. J. Heat and Fluid Flow* (available online: doi: 10.1016/j.ijheatfluidflow.2016.09.013).
- [2] Hack M.J.P., Zaki T.A., Streak instabilities in boundary layers beneath free-stream turbulence, *J. Fluid Mech.* 741, 280-315, 2014.
- [3] McAuliffe B.R., Yaras M.I., Transition mechanisms in separation bubbles under low- and elevated freestream turbulence, *J. Turbomachinery* 132, 011004/1-10, 2010.
- [4] Wilcox D.C., Formulation of the  $k - \omega$  turbulence model revisited. *AIAA J.*, 46, 2823-2837, 2008.
- [5] Walters D.K., Cokljat D., A three-equation eddy-viscosity model for Reynolds-averaged Navier-Stokes simulations of transitional flow, *J. Fluids Engineering* 130, 2401/1-14, 2008.
- [6] Walters. K., Physical interpretation of transition-sensitive RANS models employing the laminar kinetic energy concept, *Ercoftac Bulletin* 80, 67-76, 2009.
- [7] Khodak A., Hirsch C., Second-order non-linear  $k - \omega$  models with explicit effect of curvature and rotation, in *Proceedings of Third ECCOMAS Computational Fluid Dynamics Conference*, Paris, France, Wiley, ISBN 0471958514, 690-696, 1996.
- [8] Kubacki S., Dick E., An algebraic model for bypass transition in turbomachinery boundary layer flows, *Int. J. Heat and Fluid Flow*, 58, 68-83, 2016.
- [9] Menter F.R., Smirnov P.E., Liu T., Avancha R., A one-equation local correlation-based transition model, *Flow Turbul. Combust.* 95, 583-619, 2015.
- [10] Zarzycki R., Elsner W., The effect of wake parameters on the transitional boundary layer on a turbine blade, *IMEchE Part A, J. Power and Energy*, 219, 471-480, 2005.
- [11] Wang T., Keller F.J., Zhou D., Flow and thermal structures in a transitional boundary layer. *Exp. Therm. Fluid Sci.* 12, 352-363, 1996.
- [12] Wilcox D.C., *Turbulence modelling for CFD*. DCW Industries, Inc, 1993.

# SKIN FRICTION REDUCTION IN FULLY DEVELOPED TURBULENT CHANNEL FLOW BASED ON DNS AND ADJOINT SHAPE OPTIMIZATION

T. Köthe<sup>1,2</sup> and C. Wagner<sup>1,2</sup>

<sup>1</sup>*Institute of Aerodynamics and Flow Technology,  
German Aerospace Center (DLR), Göttingen, Germany*

<sup>2</sup>*Institute of Thermodynamics and Fluid Mechanics,  
Technische Universität Ilmenau, Ilmenau, Germany*

thomas.koethe@dlr.de

## Abstract

Direct Numerical Simulations (DNS) of turbulent channel flow are performed with the aim to reduce the skin friction by controlling the near-wall transport processes based on surface modifications. To determine the latter the adjoint Navier-Stokes equations are solved. They provide surface sensitivities indicating an optimal wall shape. After a first surface modification the DNS is continued with the modified geometry. Time-averaging of the instantaneous wall shapes produced with this approach will hopefully lead to a steady wall shape which controls the flow according to a prescribed objective function.

Considering the objective function turbulent kinetic energy (TKE) it is shown that the approach leads to a new wall shape which reduces the mean pressure drop for a prescribed flow rate and therefore the associated wall shear stress.

## 1 Introduction

Passive flow control often relies on structural changes of the wall contours or on flow control devices which are installed on the wall. Although it is widely known that certain flow control devices like riblets or dimples have an effect on aerodynamic quantities like lift or drag, it is not fully understood, how they interact with near-wall flow structures and how the type and the size of these devices scale with the Reynolds number. According to Kim *et al.* (1987), the wall-normal momentum transport is organized in sweep and ejection events in the boundary layer which control skin friction. In a DNS study Bewley *et al.* (2001) actively controlled these streaks with a blowing and suction approach and reduced the skin friction. The final aim of this work is to rely on passive flow control and to identify surface modifications on the walls of a channel which influence the development of turbulent coherent flow structures and reduce the drag. To resolve all relevant flow structures in space and time, the unsteady Navier-Stokes equations are solved in the sense of a direct numerical simulation (DNS).

Additionally, an adjoint shape optimization method computes sensitivities  $S$  for every cell of a surface mesh defined by the volume mesh constructed to fulfill the requirements of a DNS in a minimal channel domain. The sensitivities reflect the impact of surface normal grid deformation with respect to one or more specified objective functions. In the adjoint optimization framework any point of the surface mesh serves as a design variable

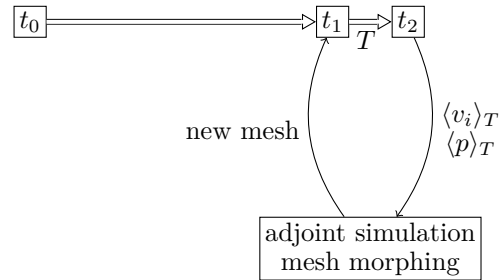


Figure 1: Timeline of the optimization framework, with the times  $t_0$  as the starting point,  $t_1$  as the time needed to reach a fully developed state and  $t_2$  as the time after the specific time interval  $T$

with respect to the Navier-Stokes and continuity equations and their continuous adjoint equivalents.

The fully developed turbulent channel flow is of unsteady nature, so the optimization problem is unsteady as well. To avoid a time dependency in the adjoint equations and the related problems, the solution of the DNS is averaged over a specific time interval  $T$ . One aim of the work is to identify appropriate time intervals to enhance the effectiveness of the optimization procedure in the limits of  $T$ .

The complete timeline of the optimization procedure is shown in figure 1.

## 2 Adjoint shape optimization

Since the flow problem is governed by the unsteady, incompressible Navier-Stokes equations

$$\begin{aligned} \frac{\partial v_i}{\partial t} + \frac{\partial}{\partial x_j} (v_i v_j) &= -\frac{\partial p}{\partial x_i} + \frac{\partial}{\partial x_j} \left[ \nu \left( \frac{\partial v_i}{\partial x_j} + \frac{\partial v_j}{\partial x_i} \right) \right] \\ -\frac{\partial v_j}{\partial x_j} &= 0, \end{aligned} \quad (1)$$

with the velocity vector  $v_i$ , the specific pressure  $p$  and the kinematic viscosity  $\nu$ , a finite volume method based on central differencing in space and suitable to deal with unstructured grids is used. The investigated domain is a minimal channel with periodic boundary conditions in streamwise and spanwise directions. Considering a prescribed bulk velocity of  $v_{bulk} = 1m/s$ , the mass flux is controlled to be constant and the pressure drop and the skin friction adjust to this requirement. The Reynolds number, based on the channel half height and the friction

velocity  $v_\tau = 0.063m/s$ , is  $Re_\tau = 180$ . After reaching a statistically steady state in the DNS of fully developed turbulent channel flow, instantaneous velocity fields are averaged over a time interval  $T$ , to obtain the turbulent kinetic energy ( $TKE$ ). The procedure is illustrated in figure 1. In Bewley *et al.* (2001) it is shown that minimizing the skin friction directly is not the most effective way if the above mentioned time-averaging is performed. Another measure for the intensity of the turbulent transport processes is the turbulent kinetic energy. Thus, the latter is selected as a possible objective function to identify modifications of the shape of the channel walls. The constraint  $\mathcal{R}$  is to fulfill the unsteady, incompressible Navier-Stokes equations (1). Then, the optimization problem

$$\min J_{TKE} = \frac{1}{2} \int_T \int_y \langle v'_i \rangle_T^2 dy dt \quad (2)$$

wrt.  $\mathcal{R} = 0$ .

is solved by the method of Lagrange multipliers. The latter is based on the Lagrange equation

$$L = J(\langle v_i \rangle_T, \langle p \rangle_T) + (u_i, q) \cdot R(\langle v_i \rangle_T, \langle p \rangle_T) \quad (3)$$

with the Lagrange multipliers  $u_i$  and  $q$ . Minimization of the Lagrange equation is formally achieved by considering the total variation  $\delta L = \delta_\beta L + \delta_{v_i} L + \delta_p L$ , where  $\beta$  denotes the design variables. Since any change of  $\beta$  changes the state variables as well, a new solution of (1) would be required. To obviate the latter, an adjoint method, introduced by Giles *et al.* (2000) and Jameson (2003), is used, where the Lagrange multipliers are chosen in a way, that the relation  $\delta_{v_i} L + \delta_p L = 0$  holds.

Because the solution of (1) is averaged over  $T$ , we assume a nearly steady flow in the specific time interval. Thereby we can neglect the time-dependency in the variation of the Lagrange equation. This leads to the time-averaged adjoint Navier-Stokes equations

$$\begin{aligned} \langle v_j \rangle_T \left( \frac{\partial u_i}{\partial x_j} + \frac{\partial u_j}{\partial x_i} \right) &= \quad (4) \\ -\nu \frac{\partial}{\partial x_j} \left( \frac{\partial u_i}{\partial x_j} + \frac{\partial u_j}{\partial x_i} \right) + \frac{\partial q}{\partial x_i} + \frac{\partial J}{\partial \langle v_i \rangle_T} \\ \frac{\partial u_i}{\partial x_i} &= \frac{\partial J}{\partial \langle p \rangle_T}. \end{aligned}$$

With this approach we can avoid an unsteady adjoint formulation, where the full history of the flow has to be considered by integrating backwards in time, as described by Griewank *et al.* (2000).

With the solution of (4), the total variation of  $L$  reduces to  $\delta L = \delta_\beta L$ . To perform the shape optimization, all points of the surface mesh must serve as design variables  $\beta$ . Therefore, a superposition of local surface normal displacements  $\beta$  was introduced by Pironneau *et al.* (1982) to obtain the shape deformation. Finally, one can compute the sensitivities in a post-processing step, following Soto *et al.* (2004), with the solutions of (1) and (4) via

$$S = \delta L = \delta_\beta L = -A\nu \left( n_i \frac{\partial u_{t,j}}{\partial x_i} \cdot n_i \frac{\partial \langle v_{t,j} \rangle_T}{\partial x_i} \right) \quad (5)$$

With these two solutions it is possible to compute sensitivities  $S$  for every cell of the boundary  $\Gamma = \partial\Omega$ , independently of the number of design variables. This reduces the computational costs extremely in comparison

to other gradient based optimization methods and maximizes the degrees of freedom in the optimization process.

Since, the computed sensitivities represent local surface normal displacements, they can be used to deform the mesh by interpolating the sensitivities to the mesh points with radial basis functions (RBF). In Köthe *et al.* (2014) a mesh deformation tool was developed, which conserves the mesh quality and avoids the need for remeshing.

In the deformation process, the centerline of the channel remains constant but the lower and upper half are deformed. To ensure a constant volume of the channel during the whole optimization process, the deformed channel halves are compressed or stretched to adjust the volume.

### 3 DNS of plain channel

For the present study, the Navier-Stokes equation are solved directly (DNS) using a second-order accurate central differencing scheme for spatial discretization and a second-order accurate explicit Leapfrog time integration scheme. The coupling of the velocity and the pressure fields is performed with Chorin's projection method (Chorin 1968).

The considered plain channel has periodic boundary conditions in stream- and spanwise directions, the bottom and the top are physical wall boundaries with no-slip conditions. The grid spacing in wall-normal direction is  $\Delta y_{wall}^+ = 0.41$  at the wall and  $\Delta y_{center}^+ = 4.00$  at the centerline, where  $+$  denotes wall units based on the friction velocity. In spanwise direction the spatial resolution is  $\Delta z^+ = 3.86$  and for the streamwise direction  $\Delta x^+ = 7.85$ . Thus, the resolution is finer than used for channel flow by Moser *et al.* (1999) and comparable to mesh widths used in recent DNS studies of turbulent pipe flow by Feldmann *et al.* (2012) and El Khoury *et al.* (2013).

A dimensionless time unit  $t^+ = \frac{t \cdot v_\tau}{L}$  is introduced for the time scaling, where  $L$  denotes the channel length. The first quantity of interest is the wall shear stress  $\tau_w = \mu \left( \frac{\partial v_i}{\partial y} \right)$ . To check if the flow is in a fully-developed state, the local wall shear stress integrated over the wall planes  $\int \tau_w dA$  are monitored. A resulting time series is plotted in figure 2.

Figure 2 reveals that the flow is in a fully developed state at time  $t_1 = 414t^+$  since the values of the drag force are fluctuating around a mean value of  $0.09412N$ . The latter is defined as the reference value for the converged solution.

Figure 3 reflects the resulting profiles of the mean axial velocity and the turbulent kinetic energy. The volume integrated value of the turbulent kinetic energy is  $k = 0.01367 \frac{m^2}{s^2}$ . Since the profiles shown in figure 3 are typical for a fully developed turbulent channel flow averaging over the specific time interval  $T$  (see fig. 1) starts after the state has been reached.

The fluctuating nature and the coherent structures of the turbulent flow in the considered channel are illustrated with the color contours of the magnitude of an instantaneous velocity field shown in figure 4. It is well known that the wall normal transport processes which are typical for a turbulent shear flow lead to the formation of elongated vortical structures and increases the drag. Since the selected objective function turbulent kinetic energy is an averaged quantity, the instantaneous

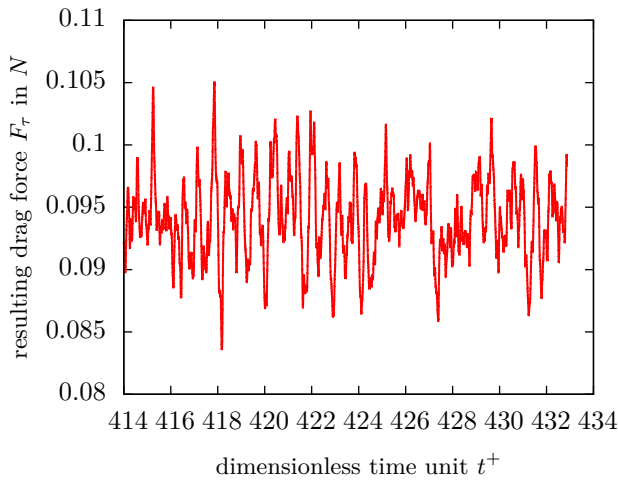


Figure 2: Integrated wall shear stress, plotted over the dimensionless time unit  $t^+$

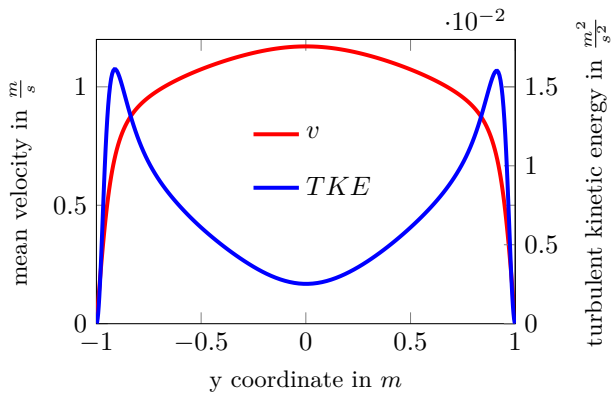


Figure 3: Mean velocity profile (red) and profile of the turbulent kinetic energy (green) in dependency, averaged in stream- and spanwise directions

flow fields are averaged over  $T$ , to obtain the mean velocity field needed in the adjoint Navier-Stokes equation.

To be able to deal with steady adjoint equations, an averaging of the flow fields is performed over the time interval  $T$  which is large enough to filter out high frequency fluctuations and small enough that footprints of the streaky structures survive in the averaged flow field. To select a suitable time interval  $T$  for the averaging procedure, we consider the mean velocity at the distance of the wall where the turbulent kinetic energy has its maximum. There, the mean velocity equals 11 times the friction velocity. As reference length, the half channel length is used to make sure, that the considered structures remain inside the channel domain during the time interval  $T$ . We assume, that averaging over 11 turnovers with the friction velocity and the half channel length, which corresponds to 5.5 turnovers in the full channel is a reasonable guess for the time interval  $T$ . The mean velocity obtained by averaging of  $T$  is illustrated in figure 5. It can be seen that a wavy pattern close to the wall is still visible. The color contours of the velocity magnitudes averaged over  $5t^+$  is shown in Figure 5. It demonstrates that small scale fluctuations are removed while large scale fluctuations remain close to the wall. The same averaging is applied to the instantaneous pressure fields and both are considered as steady to be able to use them as constraints for the optimization process.

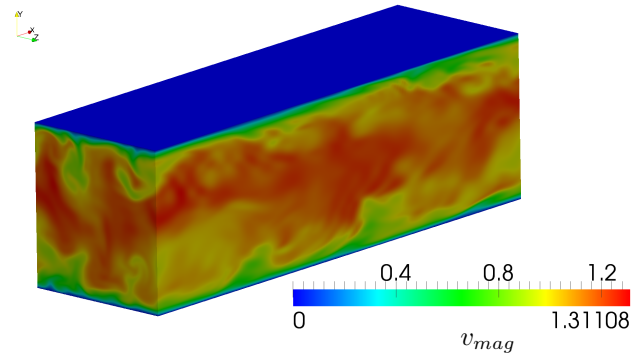


Figure 4: Magnitude of the instantaneous velocity field

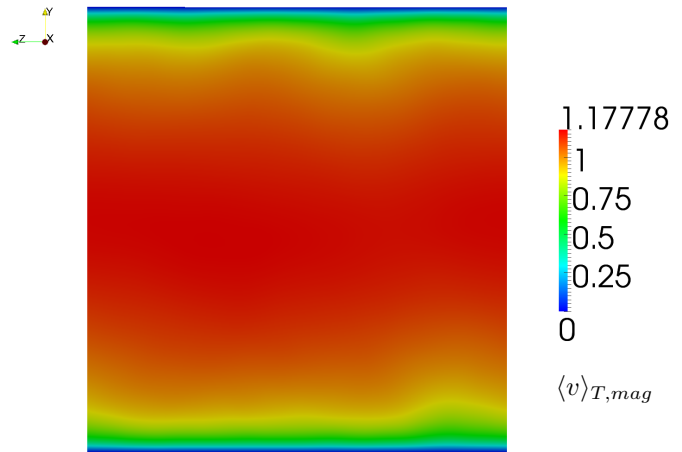


Figure 5: Magnitude of the velocity, averaged over  $5t^+$

## 4 Results

For the optimization process, the mean flow field obtained from the velocity fields of the DNS after time-averaging over the specific time interval  $T$  is needed to solve the adjoint equation (4). With both solutions the resulting surface sensitivity distribution in the channel walls can be computed in a post-processing step via (5). In order to avoid excessive mesh deformations, the values of the computed surface sensitivities are scaled to limit the deformations to a prescribed maximum value. A parameter study has shown, that a maximum deformation of 1% of the boundary layer thickness, which corresponds to  $1\text{cm}$ , leads to the best optimization results.

Based on the scaled surface sensitivities, the channels walls are deformed for different time intervals  $T = t^+, 2t^+, 3t^+, 5t^+$  and  $10t^+$ , to identify the most effective value for  $T$ . The deformation, resulting from the optimization with  $T = 5t^+$  is presented in figure 6, where the deformation is enlarged for a better visibility.

Then, the DNS is restarted from the time  $t_1$  with each deformed channel domain (see figure 1) and the solution is again averaged over  $T$ . The volume integrated values of the turbulent kinetic energy obtained with the dif-



Figure 6:  $TKE$ -optimized shape of the channel walls, with the bottom wall (left) and the top wall (right)

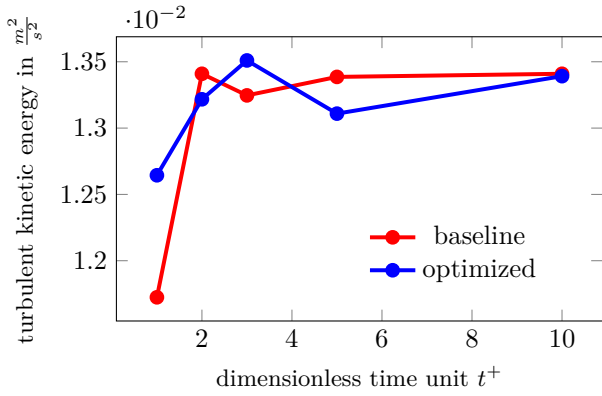


Figure 7: Turbulent kinetic energy  $TKE$ , averaged over different  $T$  for the plain channel (red) and for the different optimized geometries (blue)

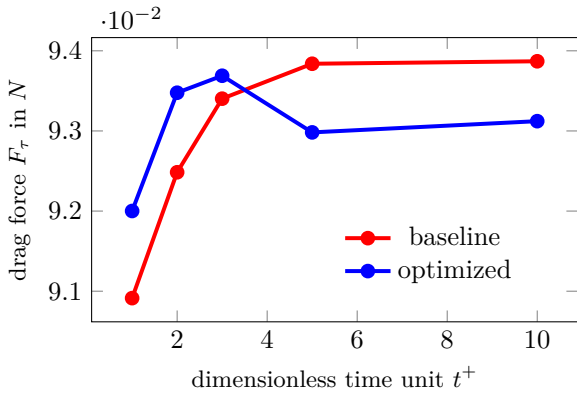


Figure 8: Resulting drag force, averaged over different  $T$  at the top and bottom walls of the plain channel (red) and for the different optimized geometries (blue)

ferent averaging intervals are plotted in figure 7. The comparison reveals that the turbulent kinetic energy obtained in the plane channel (baseline) is nearly converged after  $5t^+$ . For the same time averaging interval the reduction of  $TKE$  obtained in the deformed channel is the highest with 2%. It should be noted, that each value in the graph for the optimized channel configurations belongs to a different geometry. The corresponding drag force is plotted in figure 8. Figure 8 reveals, that  $T = 5t^+$  is associated with a reduction of the drag force of 0.9%. Thus, the trend of the drag force obtained for the different time-intervals is consistent with the corresponding  $TKE$ -values.

The wall shear stress in streamwise direction is plotted in figure 9. According to Jimenez *et al.* (1991), the flow is asymmetrical with respect to the center plane of the channel, which is an artifact of the minimal channel domain. This asymmetry is also visible in the distribution of the streamwise component of the wall shear stresses at the two walls presented in figure 9. The distribution of the streamwise component of the wall shear stress obtained in the modified geometry is shown in figure 10. The asymmetries in the flow can be observed here as well and this effect is reflected also in the optimization results. While a reduction of the drag force of 1.1% is obtained for the bottom wall, the resulting drag force at the top wall is only 0.7% lower. The comparison of the drag forces obtained in different channel geometries clearly demonstrates, that the objective function turbulent kinetic energy is suitable to produce a substantial reduction of the wall shear stress. For the modified geometry

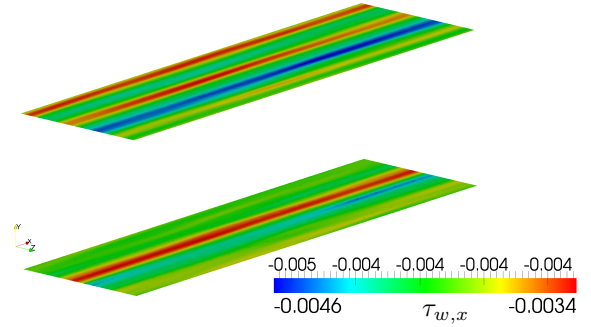


Figure 9: Streamwise component of the wall shear stress for the plain channel, averaged over  $5t^+$

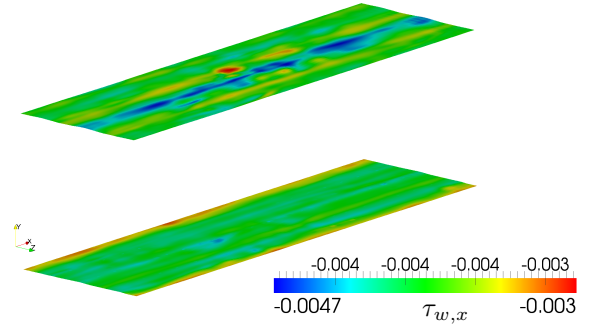


Figure 10: Streamwise component of the wall shear stress at the top and bottom wall of the modified channel, averaged over  $5t^+$

the distribution of the wall shear stress is more homogeneous, which is true especially at the bottom wall.

The DNS with the modified channel is continued, until the mean values are statistically converged. So far, the observed skin friction reduction is conserved.

## 5 Conclusions and outlook

An approach to identify wall modification which interact with the flow structures in a turbulent channel flow was presented. It relies on a DNS and adjoint shape optimization. Using the mean flow fields provided by the DNS, a steady state formulation of the adjoint Navier-Stokes equation results in surface sensitivities, which lead to a new, optimized surface. Considering different time intervals for the averaging procedure it turned out that the time interval which ensures that the characteristic streaky structures pass the half of the channel length leads to a reduction of the drag of 0.9% after a single iteration. More iterations will hopefully improve the skin friction reduction.

To further improve the optimization result, detailed investigations of alternative target functions are necessary.

## References

- Bewley, T. R. and Moin, P. and Temam, R. (2001), DNS-based predictive control of turbulence: an optimal benchmark for feedback algorithms, *J. Fluid Mech.*, Vol. 447, pp. 179-225.
- Chorin, A.J. (1968), Numerical solution of the Navier-Stokes equations, *Math. Comp.*, Vol. 22, pp. 745-762.
- El Khoury, G. K. and Schlatter, P. and Noorani, A. and Fischer P. F. and Brethouwer, G. and Johansson,

- A. V. (2013), Direct Numerical Simulation of Turbulent Pipe Flow at Moderately High Reynolds Numbers, *Flow, Turbulence and Combustion*, Vol. 91, pp. 475-495.
- Feldmann, D. and Wagner C. (2012), Direct numerical simulation of fully developed turbulent and oscillatory pipe flows at, *Journal of Turbulence*, Vol. 13, pp. 1-28.
- Giles, M. B. and Pierce, N. A. (2000), An introduction to the adjoint approach to design, *Flow, Turbulence and Combustion*, Vol. 65, pp. 193-415.
- Griewank A. and Walther A. (2000), Algorithm 799: revolve: an implementation of checkpointing for the reverse or adjoint mode of computational differentiation, *ACM Transactions on Mathematical Software (TOMS)*, Vol. 26, pp. 19-45.
- Jameson, A. (2003), Aerodynamic shape optimization using the adjoint method, *VKI Lecture Series 2003-02, Brussels*.
- Jimenez, J. and Moin, P. (1991), The minimal flow unit in near-wall turbulence, *J. Fluid Mech.*, Vol. 225, pp. 213-240.
- Kim, J. and Moin, P. and Moser, R. (1987), Turbulence statistics in fully developed channel flow at low Reynolds number, *J. Fluid Mech.*, Vol. 177, pp. 133-166.
- Köthe, T and Herzog, S. and Wagner, C., Shape optimization of aircraft cabin ventilation components using adjoint CFD, *Engineering Optimization 2014*, pp. 675-680.
- Moser, R. D. and Kim, J. and Mansour, N. N. (1999), Direct numerical simulation of turbulent channel flow up to  $Re_\tau=590$ , *Physics of Fluids*, Vol. 11, pp. 943-945.
- Pironneau, O. (1982), Optimal shape design for elliptic systems, *Lecture Notes in Control and Information Sciences*, Vol. 38, pp. 42-66.
- Soto, O. and Löhner, R., On the computation of flow sensitivities from boundary integrals, *Proceedings of the 42nd AIAA Aerospace Sciences Meeting and Exhibit, Reno NV*, Vol. 112

# A COMPARATIVE STUDY OF DES TYPE METHODS FOR MILD FLOW SEPARATION PREDICTION ON A NACA0015 AIRFOIL

L. Wang<sup>1</sup>, L. Li<sup>2</sup> and S. Fu<sup>1</sup>

<sup>1</sup>*Tsinghua University, Beijing, China, 100084*

<sup>2</sup>*AVIC Aerodynamics Research Institute, Harbin, China, 150001*

fs-dem@tsinghua.edu.cn

## Abstract

This study conducted Detached-Eddy Simulations (DES) of mildly separated flow over a 0.35 m chord NACA0015 airfoil at an incidence angle of  $11^\circ$  and a chord Reynolds number of 1 million. The unsteady flow phenomena were simulated by using Delayed DES (DDES) and Improved DDES (IDDES) methods. This work included a comparison of different choices of underlying RANS models as well as subgrid-scale stress models in LES mode. Results from these computations were compared with experimental observations, enabling their reliable assessment through the detailed investigation of the Reynolds stresses as well as the separation and reattachment. It was found that among all the DES type methods investigated in this article, only the Spalart-Allmaras-based IDDES captured the separation point as measured in the experiments. The classical vortex-shedding and the shear-layer flapping modes for airfoil flows with shallow separation were also analysed from the IDDES results by using Dynamic Mode Decomposition.

## 1 Introduction

The determination of flow separation regions is a key task in the design process of wings and turbines, which presents an ideal application for hybrid RANS-LES methods (HRLM), in part due to the challenge posed for standard CFD techniques in terms of solution fidelity and computational expense. The fundamental advantages of HRLM are manifest both in terms of computational costs and of accuracy in the prediction of complex wall bounded flows. Furthermore, the high performance of LES in the outer turbulent regions is maintained in HRLM.

The first hybrid RANS-LES method, known as Detached-Eddy Simulations (DES) proposed by Spalart et al (1997), is to combine the strengths of the RANS scheme near the solid wall boundaries and LES elsewhere. Following this, the approach was applied to other RANS models, e.g. based on the  $k-\omega$ -SST proposed by Travin et al (2002). Since then HRLM have found an ever increasing interest, which resulted in elimination of some problems found in the early applications of these methods through appropriate improvements, e.g. the Delayed DES (DDES) proposed by Spalart et.al (2006) or Improved Delayed DES (IDDES) proposed by Shur et.al(2008) and inspired a large variety of methods not restricted to DES-like approaches. The ability to capture separated flows with affordable computational cost has prompted their use over a wide range of application areas, especially for flows with massive separation. However, it is found that in mildly separated flows, the

so-called “Grey Area” problem arises. It is that part of the flow domain where the transition between RANS and LES takes place and where despite being in LES mode the flow field does not contain enough resolved turbulence as none is provided by the RANS part. Consequently, an overall turbulence deficit arises, as there is neither sufficient modelled turbulence nor sufficient resolved ones due to its slow development in LES mode, which in turn can compromise the whole simulation.

There were several attempts to address the “Grey Area” problem in DES. Shur et al (2011) used Implicit LES (ILES) for jet-noise cases, but ILES was not satisfactory for flows in which the turbulence again interacts with bodies. Kok et al (2010) proposed a temporal high-pass filter that effectively reduced eddy viscosity in the early shear layer, which was however incompatible with unsteady geometries. Mockett et al (2015) replaced the Smagorinsky model with the as the WALE (Wall-Adapting Local Eddy-viscosity) SGS (Subgrid-scale stress) model proposed by Nicoud et al (1999) in LES mode, which led to a significant acceleration of RANS to LES transition. Note that their method retained generality, as demonstrated for a plane shear layer, a backwards-facing step and a round jet.

Recently, Siau et al (2010) experimentally studied the actively controlled flow over a 0.35 m chord NACA0015 airfoil at an incidence angle of  $11^\circ$  and a chord Reynolds number of 1 million. It was then selected as a standard test case by the EU-China project MARS (Manipulation of Reynolds Stress for Separation Control and Drag Reduction). The researchers within this project tried to numerically validate the experimental findings using HRLM. However, Durrani et al (2011)’s results agree poorly with the experimental data for the unexcited case where the flow separation is mild.

Our objective is thus to numerically investigate the mildly separated flow phenomena on the NACA0015 airfoil, by using Delayed DES (DDES) and Improved DDES (IDDES) methods. This work includes a comparison of different choices of underlying RANS model as well as SGS model in LES mode.

## 2 Numerical methods and grid generation

### A. Flow solver

An implicit pressure-based solver with a fully conservative approximation of the governing equations is employed in the flow simulation. The code is based on curvilinear coordinates and uses cell-centered collocated storage arrangement on semi-block structured grids for all quantities. The one-equation SA model proposed by Spalart et al (1992) and  $k-\omega$  SST model proposed

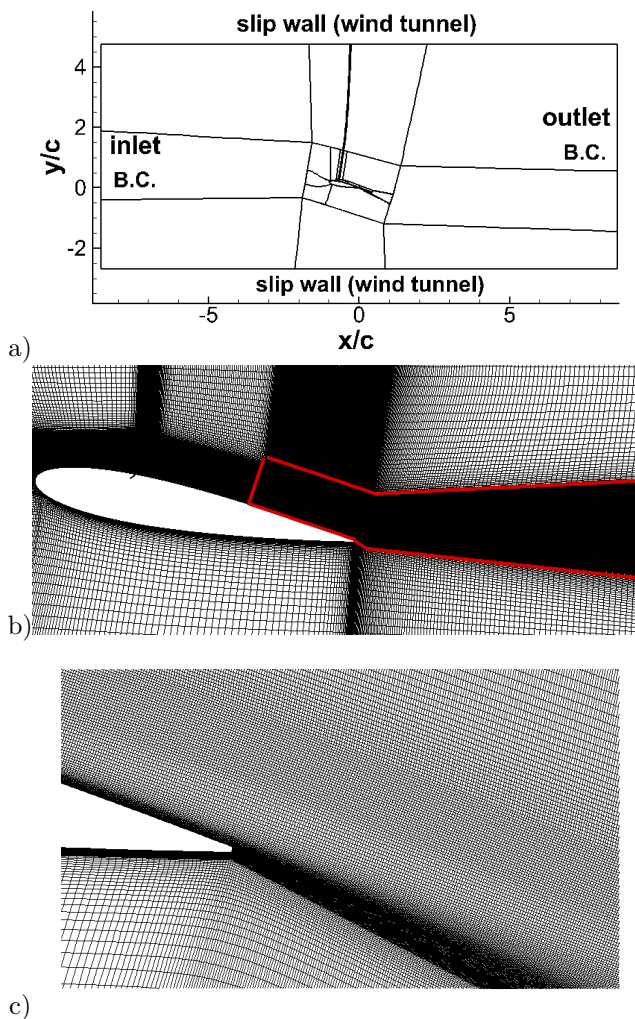


Figure 1: Topology of computational mesh

by Menter (1994) are used as the underlying models for the DDES and IDDES presented here. The CDES parameter is set to 0.628 for the SA model and to 0.550 for the SST model, as calibrated against the decay of isotropic turbulence by Mockett (2009). In order to best address the inconsistency in the demands posed by RANS and LES on the numerical scheme for the convective fluxes, the blending function of Travin et al (2002) is employed to assure an appropriate switch between a higher-order TVD scheme and central differencing. The diffusive fluxes are approximated using a second order central scheme and for time discretization second order backward differencing is applied. The continuity equation is conserved by the SIMPLE algorithm whereby the decoupling of pressure and velocity is prevented through a modified Rhie & Chow interpolation. According to Knacke (2013)'s work, this modification ensures retention of functionality at small time steps and reduces spurious noise. The code is parallelized via domain decomposition and the data interchange between processors is realized through the standardized MPI-library. RANS solutions obtained with the SA or SST models are used as initial condition for the DDES and the IDDES.

## B. Computational Mesh

In the previous work by Wang et al (2014), two 2-D grids of 0.10 million (see Fig. 1b) and 0.14 million nodes, respectively, were generated to test the grid inde-

pendence. The 3-D grid is based on an expansion of the 2-D mesh slice into the spanwise direction. 101 layers of the 2-D mesh are combined. As a result of refining the grid, the turbulent viscosity is slightly lowered in the free shear layer. This indicates a more LES-like simulation than with baseline grid. However, it already provides a good representation of the turbulent structures on the baseline grid. It is also proven that the use of periodic boundaries is valid in case of an adequate spanwise domain size.

The computational domain adopted is of size  $LC \times LN \times LZ = 17.1c \times 7.4c \times 0.18c$  and the total number of grid is 13.5 million nodes. According to Spalart et al (2001), both the focus region (above the airfoil while downstream the separation point at  $x/c = 0.7$ ) and the departure region (wake), shown in Fig. 2b in red, need to be resolved sufficiently to be in LES mode. The grid has a very fine resolution in the streamwise and spanwise directions to meet the DES criterion of a Courant-Friedrichs-Lewy (CFL) number less than 1. The non-dimensional wall distance of the first cell center remains below  $y^+ = 1$  on the entire surface.

**C. Numerical setup and parameters** RANS simulations are performed prior to the unsteady simulation using the same turbulence model as used for the DESs. All the DESs have been run for more than 20 convective time units,  $\tau = tU_\infty/c$ , before the evaluation of averages and the storage of the surface data was initiated. The sampling times are at least 30 convective time units for the DESs. A separate study of the influence of time step size indicated that a typical time step of  $\Delta t = 2.5 \times 10^{-2} c \sin \alpha / U_\infty$  is sufficient to obtain results independent of the temporal resolution. The time step gives fair accuracy up to  $St = 2$ . The spectra will be displayed up to 1/3 of the Nyquist frequency, which is  $St = 20$ . Roughly 2 orders of magnitude residual reduction are reached within 10 outer iterations per time step.

## 3 Results and discussions

The various results reported herein correspond to the five different models employed during the study. Results of the DDES and IDDES computations are labeled DDES and IDDES, respectively. Then, results labeled SA and SST respectively correspond to those predictions in which the one-equation SA model and  $k-\omega$  SST model are used as the underlying RANS models. Finally, the results labeled by SMG have been obtained using the standard SGS model (Smagorinsky model) while by WALE using WALE SGS model in LES mode. For instance, DDES-SA-WALE represents the DDES computations with the SA RANS model as well as the WALE SGS model.

Fig. 2 compares the instantaneous turbulence structures (iso-surface of the second invariant of velocity gradient). It is seen that the grid resolution remains sufficiently fine enough to resolve the intrinsic small-scale turbulent structures in the shear layer for all five models. The calculated separation locations from the five models are given in Table 1. The measured separation location,  $x_{sep}$ , at 70% of the chord length is very well predicted by both IDDES-SA and DDES-SA-WALE, whereas both DDES-SA-SMG and DDES-SST-SMG models predict a delayed separation compared to experimental results, and therefore there is little turbulence generation and flow structures shown in Fig. 2a and Fig. 2c. On the contrary, IDDES-SST gives an over-prediction in the bubble length (see Fig. 3d) as well as in the turbulence structures (see Fig. 2d).

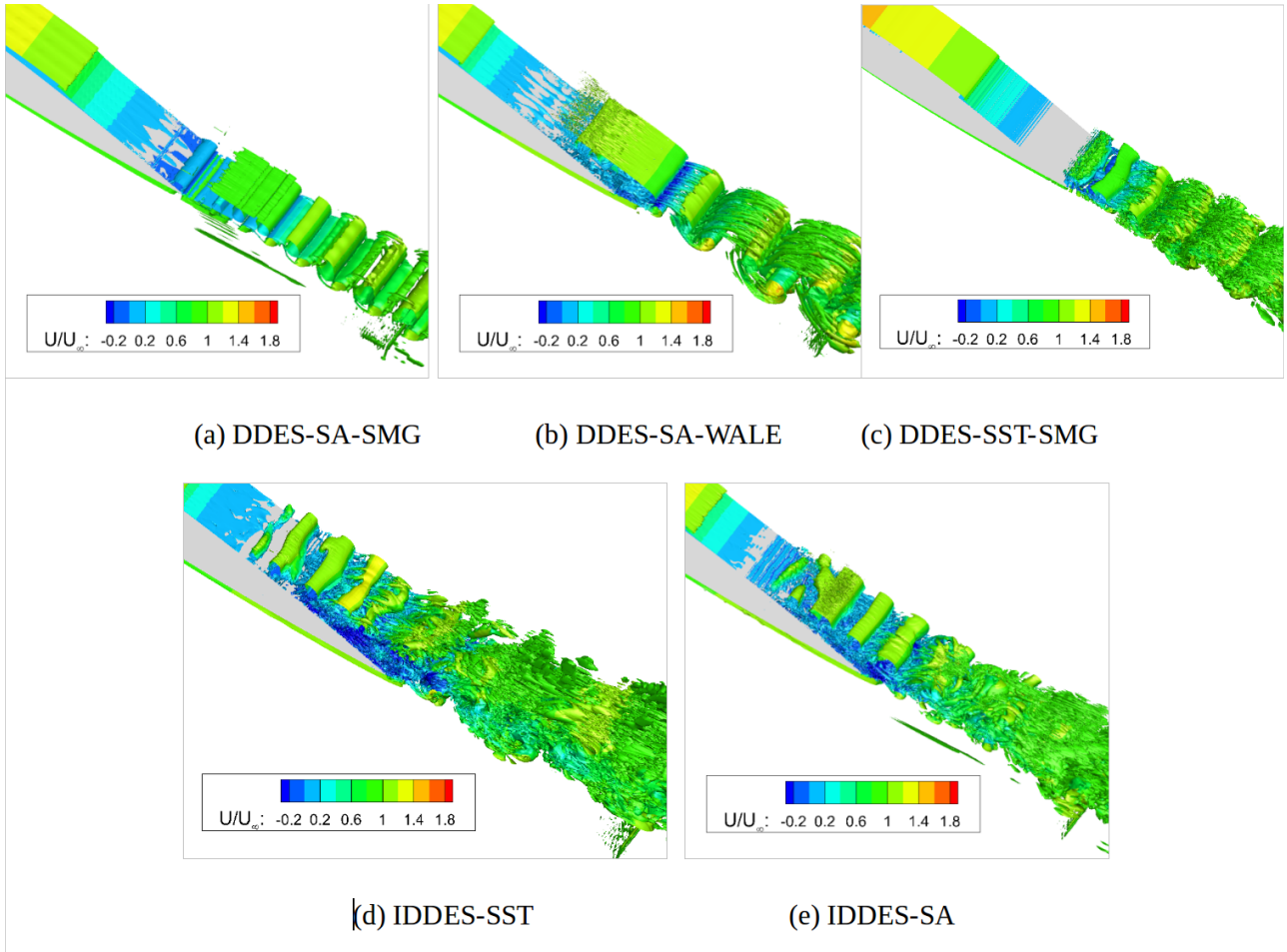


Figure 2: Instantaneous flow using the  $\lambda_2$  vortex core criterion at  $\lambda_2 = -500s^{-2}$ , shaded by dimensionless velocity

Table 1: Comparisons of separation location between computations and measurements

Methods	DDES-SA-SMG	DDES-SA-WALE	DDES-SST-SMG	IDDES-SST	IDDES-SA	Measurements
Separation location	0.851c	0.677c	0.906c	0.562c	0.690c	0.700c

The pressure distribution contributes the most to the lift enhancement. The time-averaged surface pressure plot  $C_p$  in Fig. 3, including zoomed views near the trailing edge, indicates that IDDES-SA gives accurate prediction in the trailing-edge separated-flow region that is simulated with LES. The overshoot of both DDES-SA-SMG and DDES-SST-SMG in  $C_p$  at trailing edge can be attributed to their over-prediction in  $x_{sep}$  and vice-versa for the IDDES-SST results. Moreover, the initial dip in all DES results in the leading-edge section shows an early switching from LES to RANS there.

Fig. 4 and Fig. 5 compare the time-averaged streamwise velocity profiles and streamwise normal stress  $\langle u'u' \rangle$ , respectively, along the wall-normal direction at  $x/c = 0.84$  and  $0.97$  with the available experimental results. Note that the two profiles are located across the separation bubble. It is observed that the measured profiles are in errors, where the velocity does not show negative sign for the reverse flow in the separation bubble. Due to capturing incorrect separation location, IDDES-SST gives too much negative velocity intensity and overshoot in Reynolds stresses, while both DDES-SA-SMG and DDES-SST-SMG show no negative sign in velocity profiles and pretty weak turbulence intensity. IDDES-

SA and DDES-SA-WALE give similar velocity profiles, whereas their discrepancy is huge in Reynolds stresses. Although there are some gaps between the results by IDDES-SA and measurements, the consistent distribu-

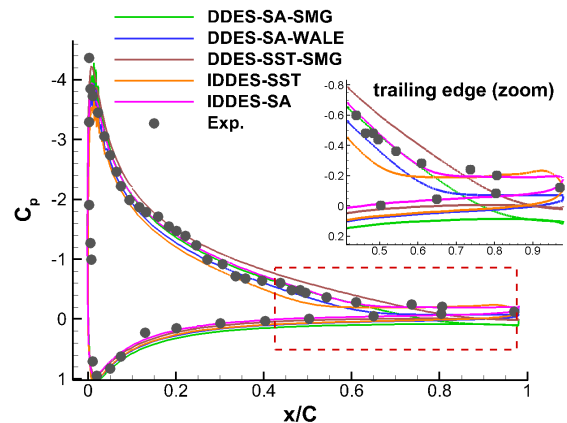


Figure 3: Time-averaged surface pressure distribution along the airfoil

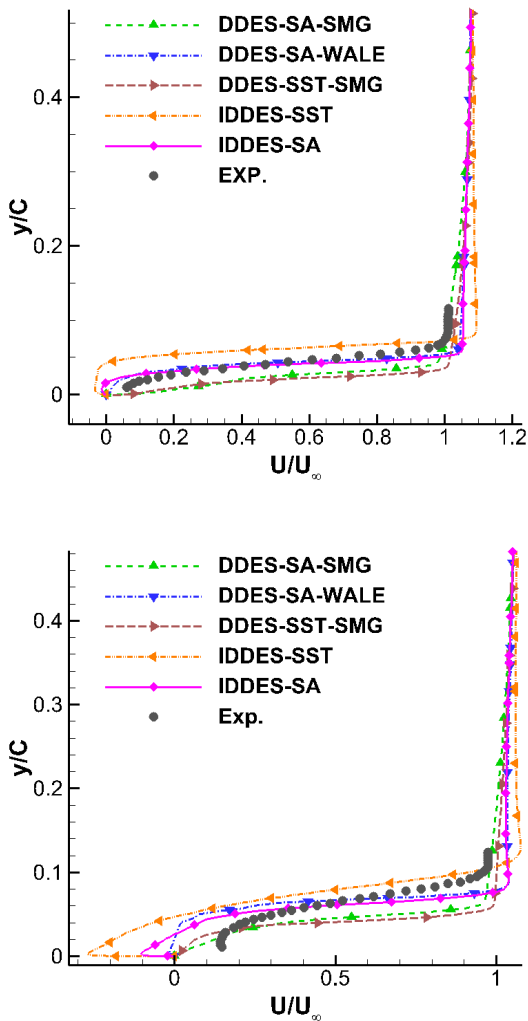


Figure 4: Streamwise velocity profiles at  $x/c=0.84$  (top) and  $0.97$  (bottom)

tion trends is obtained. On the contrary, turbulence intensity predicted by DDES-SA-WALE is close to zero.

Fig. 6 displays the time-averaged streamwise velocity and shear stress  $\langle u'v' \rangle$  profiles one chord length downstream the trailing edge. Only IDDES-SA predicts agreeable velocity and Reynolds stress distributions. Considering the larger separation provided by IDDES-SST, it over-predicts the wake width compared with the experiments. It is vice-versa for both DDES-SA-SMG and DDES-SST-SMG results. However, DDES-SA-WALE also gives an under-prediction in wake width, though it predicts the accurate separation location upstream.

To further compare the results of IDDES-SA and of DDES-SA-WALE, spectra analyses on the unsteady flow quantities are carried out by using Discrete Fourier Transform (DFT). Fig. 8 presents the power spectra density of the global lift coefficient as a function of the Strouhal number,  $St = fc \sin \alpha / U_\infty$ , based on the projected airfoil height  $c \sin \alpha$ . It should be noted that the smallest frequency (or the St number in Fig. 8) is related to the total time of the sampling (see Fig. 7), and the largest frequency is determined by the sampling frequency, which equals to  $1/\Delta t = 40U_\infty / (c \sin \alpha)$ . It is observed from Fig. 7 that the R.M.S. value of global lift coefficient sharply decreases from 0.042 for IDDES-SA to 0.0063 for DDES-SA-WALE results, and from Fig. 8 that the peak value in the DDES-SA-WALE spectra is

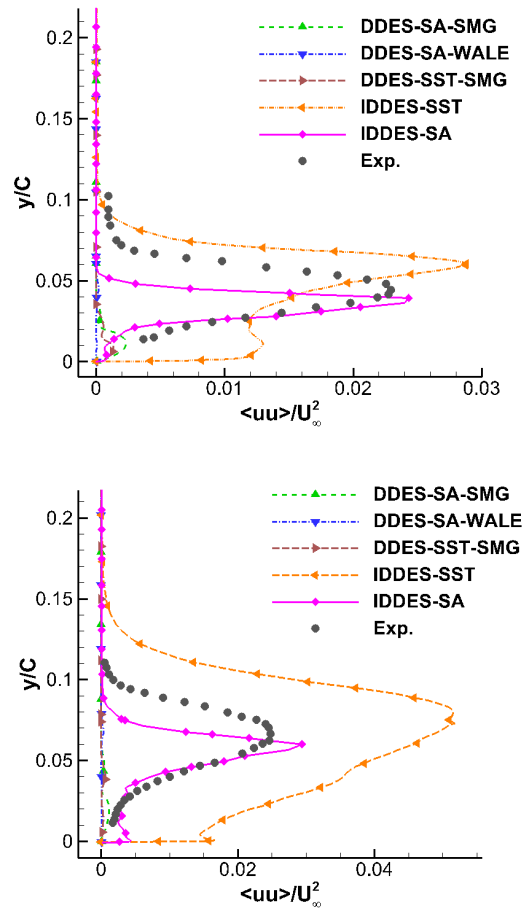


Figure 5: Streamwise normal stress  $\langle u'u' \rangle$  profiles at  $x/c=0.84$  (top) and  $0.97$  (bottom)

extraordinarily intensive compared to that in IDDES-SA results. Moreover, recall that DDES-SA-WALE predicts accurate separation location however near-zero Reynolds stress in the separation bubble (see Fig. 5). We can conclude that the separated flow simulated by DDES-SA-WALE is actually laminar.

Moreover, the Mean-Subtracted Dynamic Mode Decomposition (MSDMD) is applied to link a spatial structure (a dynamic mode) to a given frequency and to compare with the spectral analysis performed above. The MSDMD results are based on a sequence of 600 spanwise-averaged pressure snapshots (SA-IDDES results) in the focus region (see Fig.1b), with a constant sampling period  $\Delta t = 0.075c \sin \alpha / U_\infty$ . The non-dimensional frequency resolution of MSDMD is thus around St of 0.012. Fig. 10a shows the most energy-containing mode at St of 0.60, which is characteristic of the vortex shedding, also called as regular mode in Sigurdson (1995)'s results. It is due to the Kelvin-Helmholtz instability, in which the difference between the velocity within the separation bubble and the external flow causes a rollup of vortices in the shear layer proposed by Kiya et al (1997). It is noted that the frequency of this mode agrees pretty well with the peak frequency shown in Fig. 8. Besides, the second mode in energy rank at St of 0.034 (see Fig. 9), can be recognized as the shear-layer flapping mode associated with Strouhal numbers on the order of 0.02.

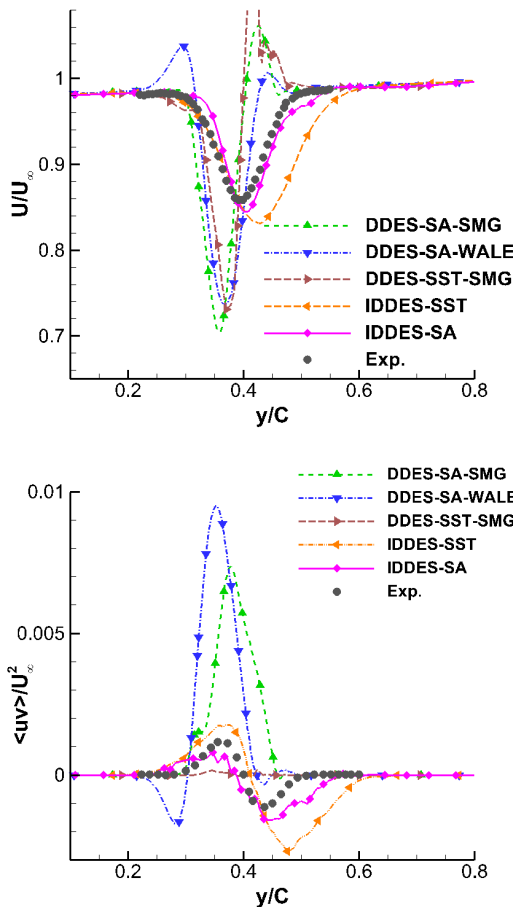


Figure 6: Comparison of streamwise velocity (top) and shear stress  $\langle u'v' \rangle$  (bottom) profiles at  $x/c=1.98$  downstream the trailing edge

## 4 Conclusions

With the use of an in-house finite-volume based flow solver, a numerical study of mildly separated flows on a NACA0015 airfoil has been conducted in this work. The flow features a relatively thick boundary layer with a mild trailing-edge separation. The value of this article lies in the assessment of five different DES-type models through the detailed investigation of the Reynolds stresses as well as the separation and reattachment. It is found that with the same mesh resolution, only the Spalart-Allmaras- based IDDES predicts flow separation and turbulent structures as demonstrated experimentally.

The comparison between IDDES-SA and IDDES-SST results indicates that the underlying turbulence model is the determining factor for the prediction of the separation and the shear layer, because SST model provides less eddy viscosity in the attached flows, in consistent with the conclusion made by Mockett (2009) for several flow cases. Both DDES methods with Smagorinsky SGS model (DDES-SA- SMG and DDES-SST-SMG) encounter the "Grey Area" problem that results in a delayed separation prediction, which was also reported by Durrani and Qin (2011) for the case of an A-airfoil with shallow flow separation.

Moreover, the application of WALE SGS model in LES mode for DDES proves to be inappropriate for such a mildly separated flow case, in which the free shear layer is close to the wall. It is noted that this approach is

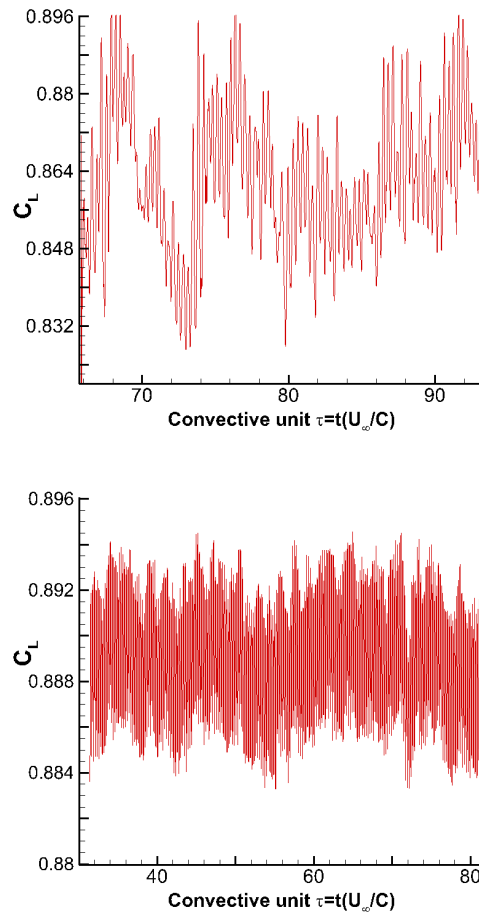


Figure 7: Sampling time series of the global lift coefficient for (top) IDDES-SA and (bottom) DDES-SA-WALE

designed to counteract excess eddy viscosity in free shear layer, which has addressed the "Grey Area" problem in cases that the free shear layer is away from the wall. However, it also eliminates the eddy viscosity at the near-wall region in this shallow-separation case, resulting in no turbulence appearances downstream the separation point.

Based on the IDDES-SA results, spectra analyses are carried out by using Discrete Fourier Transform. Dynamic Mode Decomposition is then used to identify spatial structures to the different Strouhal frequencies. The classical vortex-shedding and the shear-layer flapping modes are observed, demonstrating the correctness of the IDDES-SA computations.

## References

- [1] Durrani N., Qin N.(2011), Behavior of Detached-Eddy Simulations for mild airfoil trailing-edge separation, Journal of Aircraft, Vol.48, pp.193-202.
- [2] Kiya M. S., Shimizu M., Mochizuki O.(1997), Sinusoidal forcing of a turbulent separation bubble, Journal of Fluid Mechanics, Vol.342, pp.119-139.
- [3] Knacke T.(2013), Potential effects of Rhie & Chow type interpolations in airframe noise simulations. Accurate and efficient aeroacoustic prediction approaches for airframe noise, VKI lecture notes, Von Kármán Institute for Fluid Dynamics, Rhode-Saint-Genese, Belgium.

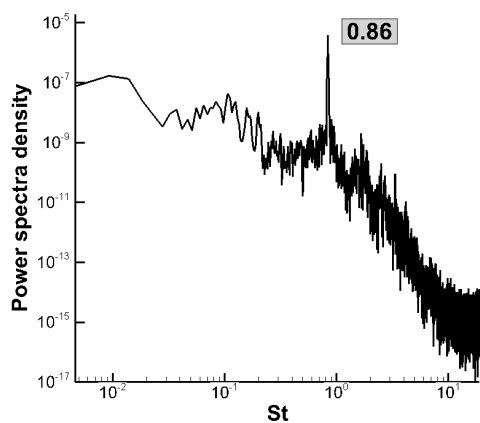
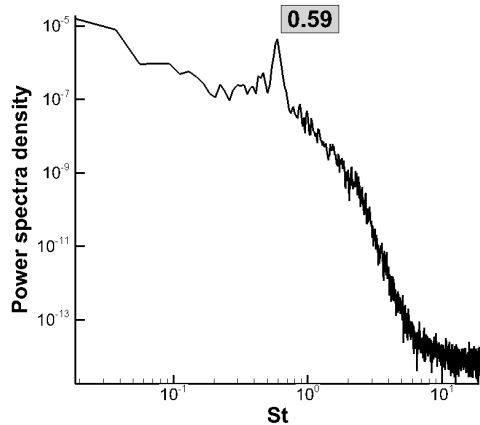


Figure 8: Spectrum of the global lift coefficient for IDDES-SA (top) and DDES-SA-WALE (bottom)

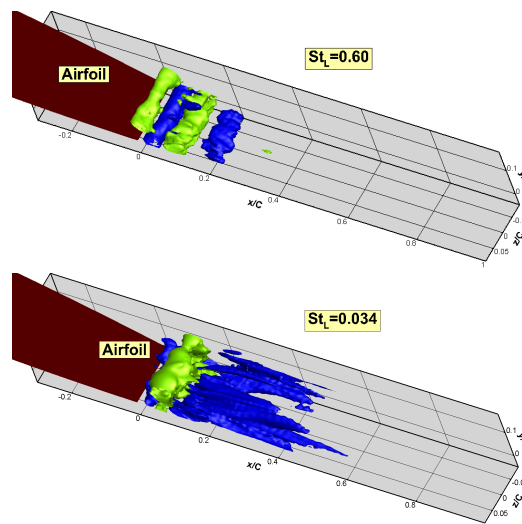


Figure 9: SA-IDDES computations: iso-contours of spanwise-averaged pressure for the regular mode (top) and the shear-layer flapping mode (bottom)

[4] Kok J. C., et al.(2010), Destabilizing free shear layers in X-LES using a stochastic subgrid-scale model, *Progress in Hybrid RANS-LES Modelling*, Springer Berlin Heidelberg, pp.179-189.

[5] Menter F. R.(1994), Two-equation eddy-viscosity turbulence models for engineering applications, *AIAA journal*, Vol. 32(8), pp.1598-1605.

[6] Mockett C.(2009), A comprehensive study of detached-eddy simulation, Ph.D. thesis, Berlin University of Technology.

[7] Mockett C., Fuchs M., Garbaruk A., et al.(2015), Two non-zonal approaches to accelerate RANS to LES transition of free shear layers in DES, *Progress in Hybrid RANS-LES Modelling*, Springer International Publishing, 187-201.

[8] Nicoud F., Ducros F.(1999), Subgrid-scale stress modelling based on the square of the velocity gradient tensor, *Flow, Turbulence and Combustion*, Vol. 62(3) pp. 183-200.

[9] Shur M. L., Spalart P. R., Strelets M. K., Travin A. K.(2008), A hybrid RANS-LES approach with delayed-DES and wall-modelled LES capabilities, *International Journal of Heat and Fluid Flow*, Vol. 29(6), pp.1638-1649.

[10] Shur M. L., Spalart P. R., Strelets M. K.(2011), LES-based evaluation of a microjet noise reduction concept in static and flight conditions, *Journal of Sound and Vibration*, Vol.330(17), pp. 4083-4097.

[11] Siau W. L., Bonnet J. P., Tensi J., Noack B. R., Cattafesta L.(2010), Transient dynamics of the flow around a NACA 0015 airfoil using fluidic vortex generators, *International Journal of Heat and Fluid Flow*, Vol.31(3), pp. 450-459.

[12] Sigurdson L. W.(1995), The structure and control of a turbulent reattaching flow, *Journal of Fluid Mechanics*, Vol.298, pp.139-165.

[13] Spalart P. R., Allmaras S.(1992), A one-equation turbulence model for aerodynamic flows, *Proc. 30th AIAA Aerospace Sciences Meeting and Exhibit*, Reno, Nevada, USA.

[14] Spalart P. R., Deck S., Shur M. L., Squires, K. D., Strelets M. K., Travin A.(2006), A new version of detached-eddy simulation, resistant to ambiguous grid densities, *Theoretical and computational fluid dynamics*, Vol.20(3), pp.181-195.

[15] Spalart P. R., Jou W. H. et al.(1997), Comments on the feasibility of LES for wings, and on a hybrid RANS/ LES approach *Advances in DNS/LES*, Vol.1, pp.4-8.

[16] Spalart P. R., Streitt C.(2001), *Young Person's Guide to Detached-Eddy Simulation Grids*, NASA CR 2001-2110321.

[17] Travin A., Shur M., Strelets M. M., Spalart P. R.(2002), Physical and numerical upgrades in the detached-eddy simulation of complex turbulent flows, *Advances in LES of complex flows*. Springer Netherlands, pp. 239-254.

[18] Wang L., Li L. Y., Fu S.(2014), Numerical investigation of active flow control on a pitching NACA 0015 airfoil using Detached-Eddy Simulation, *52nd AIAA Aerospace Sciences Meeting*, Washington, USA.

---

## ***ERCOFTAC Programme of Events 2017***

---

Organiser: Dr. Richard E. Seoud

### ***Winter-Spring 2017***

- Oil , Gas and Petroleum Modelling and Simulation, III  
Best practice and Technology Trends  
Venue: Fraser Nash Consulting, Date:15-16 March 2017
- Wind Loads on Structures - Modelling and Simulation  
Best Practice and Technology Trends  
Venue: Danish Institute of Technology, Copenhagen, Denmark, Date: 4-5 April 2017
- Hybrid RANS-LES Methods for Industrial Applications, VII  
Overview, Guidance, and Examples  
Venue: U. Manchester, UK, Date: 22-23 May 2017
- Design Optimization IV  
June 2017, Italy

### ***Summer-Autumn 2017***

- CFD for Dispersed Multiphase Flows  
VIII, October 2017, U. de Lorraine, Nancy, France
- Computational Aeroacoustics III  
Venue: ONERA, Paris, France, Date: 2-3 November 2017
- Best Practices Combustion CFD, III,  
Location: EU, Date: November 2017
- Best Practice for Eng Meshing  
Summer - Autumn 2017, EU

For further enquiries and registrations on any of the above events, or matters pertaining to FTAC, please contact: [richard.seoud-ieo@ercoftac.org](mailto:richard.seoud-ieo@ercoftac.org)

## *ERCOFTAC Workshops and Summer Schools*

### ERCOFTAC Workshops, Conferences – 2017

Title	Location	Date	Coordinators	Organiser
Montestigliano Workshop - A Workshop Series in Fluid Dynamics for Doctoral students	Montestigliano, Italy		Bagheri, Sh.	ERCOFTAC SIG 33
European Drag Reduction and Flow Control Meeting 2017 – EDRFCM2017	Monte Porzio Catone, Italy	03-06/04/2017	Quadrio, M., Lucini, P. Choi, K-S.	SIG 20
12th ERCOFTAC SIG 33 Workshop Progress in Transition Modeling and Control	Fisciano (SA), Italy	17-19/05/2017	Hanifi, A.	SIG 33
Workshop on Direct and Large Eddy Simulation (DLES) 11	Pisa, Italy	29-31/05/2017	Salvetti, M.V Armenio, V. Geurts, B.	SIG 1
A System Approach to Turbulence and Interactions Towards High Reynolds Number	Marseille, France	?/05/2017	Sagaut, P. Cambon, C.	SIG 35, 14, 24, 33
12th International SPHERIC Workshop	Ourense, Spain	13-15/06/2017	Crespo, A. J. C	SIG 40
Synthetic Flow for Heat and Mass Transfer	Nanterre, France	03-04/07/2017	Nicolleau, F.	SIG 42, 35, 14
6th Int. Workshop on Turbulent Combustion of Sprays	Napels, Italy	17/09/2017	Roekaerts, D. Sadiki, A. Gutheil, E.	SIG 28
Turbulence Cascade II	Lyon, France	?/12/2017	Gorokhovskii, M. Cambon, C.	SIG 35, 4

### ERCOFTAC Summer Schools, Courses – 2017

Title	Location	Date	Coordinators	Organiser
Summer School on Nonlinear Dynamics in Thermoacoustic Combustion Instabilities	Garching, Germany	?/06/2017	Polifke, W. Roekaerts, D.	SIG 28

**34<sup>th</sup> Short Courses**  
**on Modelling and Computation of Multiphase Flows**  
**Part I: Bases**  
**Part IIA: New Reactor Systems and Methods**  
**or**  
**Part IIB: Computational Multi-Fluid Dynamics (CMFD)**  
**Part III: CMFD with Commercial Codes**

*Zurich, Switzerland, 13-17 February 2017*  
*Hosted by the Swiss Federal Institute of Technology (ETH)*  
*in Zurich, Switzerland.*

The courses are organised in a modular form as intensive introductory courses for persons having basic knowledge of fluid mechanics, heat transfer, and numerical techniques, but also serve as advanced courses for specialists wishing to obtain the latest information.

Course language: English

**Lecturers:** S. Banerjee, D. Bestion, J. Buongiorno, M.L. Corradini, G.F. Hewitt, D. Lakehal, SimonLo, B. Niceno, H.-M. Prasser, G. Tryggvason, S.A. Vasquez, G. Yadigaroglu and S. Zaleski.

For further information contact by e-mail:

shortcourse@lke.mavt.ethz.ch

Internet: <http://www.lke.mavt.ethz.ch/shortcourse>

[ ETH ML K 14, Sonneggstrasse 3, CH-8092 Zurich, Switzerland. Tel. +41-44 632.88 21 ]

---

**ERCOFTAC/SIG 42**  
**12<sup>th</sup> Workshop on Synthetic Turbulence Models**  
**Synthetic flows for heat and mass transfer**  
**3<sup>rd</sup>-4<sup>th</sup> July 2017, Université Paris-Ouest, Nanterre La Défense, France**  
*Hosted by the Swiss Federal Institute of Technology (ETH)*  
*in Zurich, Switzerland.*

This conference on synthetic turbulence co-organised by ERCOFTAC/SIG 42, SIG14 and SIG35 is open to anyone interested in flow, heat and mass transfer modelling and/or “synthetic turbulence” including (but not restricted to) Kinematic Simulation.

**Organizers:**

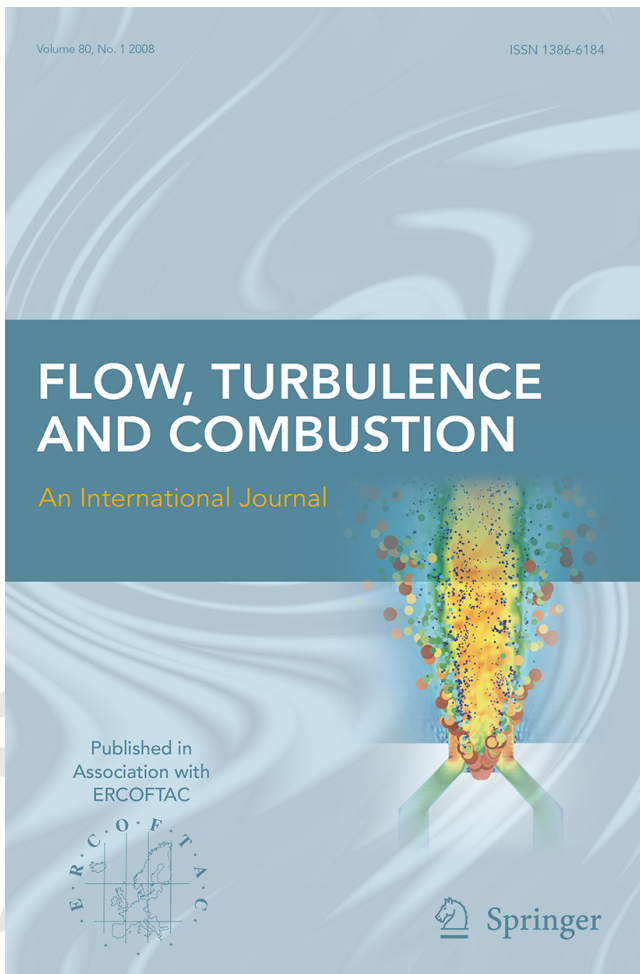
Pr D. Queiros Conde, Université Paris-Ouest, Nanterre La Défense, France, [diogo.queiros-conde@u-paris10.fr](mailto:diogo.queiros-conde@u-paris10.fr)

Dr F. Nicolleau, University of Sheffield, United Kingdom, [F.Nicolleau@sheffield.ac.uk](mailto:F.Nicolleau@sheffield.ac.uk)

Dr T. Michelitsch, Université Pierre et Marie Curie (Paris 6), Paris, France, [michel@lmm.jussieu.fr](mailto:michel@lmm.jussieu.fr)

Dr A. Nowakowski, University of Sheffield, United Kingdom, [A.F.Nowakowski@sheffield.ac.uk](mailto:A.F.Nowakowski@sheffield.ac.uk)

<http://www.sig42.group.shef.ac.uk/SIG42-12.htm>



<http://link.springer.com/journal/10494>

**Impact Factor in 2016: 1.86**

### Editor-in-Chief

Michael Leschziner,  
Imperial College London, UK,  
E-mail: [mike.leschziner@imperial.ac.uk](mailto:mike.leschziner@imperial.ac.uk)

### Editors

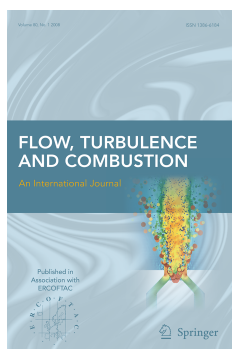
**Andreas Dreizler**, Technical University of Darmstadt, Germany  
**Koji Fukagata**, Keio University, Japan  
**Ephraim Gutmark**, University of Cincinnati, USA  
**Kemo Hanjalic**, Delft University of Technology, Netherlands  
**Andreas Kempf**, University of Duisburg-Essen, Germany  
**Suresh Menon**, Georgia Institute of Technology, USA  
**Mike Reeks**, Newcastle University, UK  
**Wolfgang Rodi**, Karlsruhe Institute of Technology, Germany

As stated on its cover, **Flow, Turbulence and Combustion (FTaC)** is *published in association with ERCOFTAC*. The expectation is, therefore, that FTaC would be a primary medium for disseminating the most innovative and highest-quality scientific output of ERCOFTAC-supported technical events.

In addition to contributed articles constituting the large majority of FTaCs published output FTaC publishes **special issues** arising from major ERCOFTAC conferences, notably **ETMM** and (in 2017) **DLES**. However, there are many other opportunities that are, arguably, not sufficiently exploited in particular, in respect of original contributions to theme issues of the Bulletin and papers arising from SIG events, such as workshops and summer schools.

Both the Editor-in-Chief of FTaC and the Scientific Programme Committee of ERCOFTAC wish to see more contributions channelled from ERCOFTAC sources to FTaC. Such contributions in the form of high-quality technical papers within the scope of FTaC are most welcome. They will be subjected to the same rigorous review process as any other contributed manuscript.

FTaC provides a forum with global reach for the publication of original and innovative research results that contribute to the solution of fundamental and applied problems encountered in single-phase, multi-phase and reacting flows, both in idealized and real systems. This includes topics in fluid dynamics, scalar transport, multi-physics interactions and flow/turbulence control. Contributions may report research that falls within the broad spectrum of analytical, computational and experimental methods, including research pursued in academia, industry and the variety of environmental and geophysical sectors. The emphasis is on originality, timeliness, quality and thematic fit, as identified by the title of the journal and the above qualifications. Relevance to real-world problems and industrial applications will be regarded as strengths. Contributions may be full-length research and review manuscripts or short communications (of no more than 6 printed pages). The latter may report new results, address contentious topics or contain discussions of full-length papers previously published in the journal. Short communications will benefit from rapid publication. All contributed manuscripts, as well as any invited contributions to Special or Theme Issues, will undergo rigorous peer review by three expert reviewers prior to decisions on acceptance or rejection.



RECENT TABLE OF CONTENTS OF FLOW TURBULENCE AND COMBUSTION

AN INTERNATIONAL JOURNAL PUBLISHED BY SPRINGER

IN ASSOCIATION WITH ERCOFTAC

EDITOR-IN-CHIEF: M. A. LESCHZINER

EDITORS: A. DREIZLER, K. FUKAGATA, E. GUTMARK, K. HANJALIC, A. M. KEMPE, S.

MENON, M. REEKS, W. RODI

FOUNDING EDITOR: F. NIEUWSTADT

**VOLUME 97, NUMBER 1, JULY 2016**

**Effects of Compressibility and Shock-Wave Interactions on Turbulent Shear Flows**

*N.D. Sandham*

**Investigation on Secondary Flow Characteristics in a Curved Annular Duct with Struts**

*H.X. Bu, H.J. Tan, H. Chen, X.M. He*

**Simulation of the Flow in a Ribbed Rotating Duct with a Hybrid  $k - \omega$  RANS/LES Model**

*S. Kubacki, J. Rokicki, E. Dick*

**Experimental Investigation and Large-Eddy Simulation of the Turbulent Flow past a Smooth and Rigid Hemisphere**

*J.N. Wood, G. De Nayer, S. Schmidt, M. Breuer*

**A Gas-Kinetic Scheme for Turbulent Flow**

*M. Righi*

**Detection of Passive Scalar Interface Directly from PIV Particle Images in Inhomogeneous Turbulent Flows**

*L. Gan*

**Towards a Thermal Optimization of a Methane/Steam Reforming Reactor**

*M. Mozdierz, G. Brus, A. Sciazko, Y. Komatsu, S. Kimijima, J.S. Szmyd*

**Large Eddy Simulation of an Internal Combustion Engine Using an Efficient Immersed Boundary Technique**

*T.M. Nguyen, F. Proch, I. Wlokas, A.M. Kempf*

**A Combined Experimental and Numerical Study of Laminar and Turbulent Non-piloted Oxy-fuel Jet Flames Using a Direct Comparison of the Rayleigh Signal**

*F. Hunger, M.F. Zulkifli, B.A.O. Williams, F. Beyrau, C. Hasse*

**Combined Influence of Strain and Heat Loss on Turbulent Premixed Flame Stabilization**

*L. Tay-Wo-Chong, M. Zellhuber, T. Komarek, H.G. Im, W. Polifke*

**Experimental Characterization of Gelled Jet A1 Spray Flames**

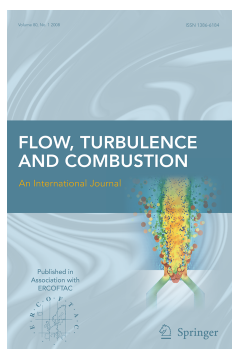
*M.B. Padwal, D.P. Mishra*

**Heat Transfer Effects on a Fully Premixed Methane Impinging Flame**

*D. Mira, M. Zavala-Ake, M. Avila, H. Owen, J.C. Cajas, M. Vazquez, G. Houzeaux*

**Eulerian Scalar Projection in Lagrangian Point Source Context: An Approximate Inverse Filtering Approach**

*C. Locci, L. Vervisch*



RECENT TABLE OF CONTENTS OF FLOW TURBULENCE AND COMBUSTION

AN INTERNATIONAL JOURNAL PUBLISHED BY SPRINGER

IN ASSOCIATION WITH ERCOFTAC

EDITOR-IN-CHIEF: M. A. LESCHZINER

EDITORS: A. DREIZLER, K. FUKAGATA, E. GUTMARK, K. HANJALIC, A. M. KEMPE, S.

MENON, M. REEKS, W. RODI

FOUNDING EDITOR: F. NIEUWSTADT

**VOLUME 97, NUMBER 2, SEPTEMBER 2016**

**Statistical Models of Large Scale Turbulent Flow**

*J.J.H. Brouwers*

**Application of the  $\gamma - Re_\theta$  Transition Model to Simulations of the Flow Past a Circular Cylinder**

*Z. Zheng, J. Lei*

**A Collaboration-based Approach to CFD Model Validation and Uncertainty Quantification (VUQ) Using Data from a Laminar Helium Plume**

*W.M. Eldredge, P. Tóth, L. Centauri, E.G. Eddings, K.E. Kelly, T.A. Ring, A. Schönbacher J.N. Thornock, P.J. Smith*

**Scour Hole Influence on Turbulent Flow Field around Complex Bridge Piers**

*A.A. Beheshti, B. Ataie-Ashtiani*

**On the Influence of Polynomial De-aliasing on Subgrid Scale Models**

*A.D. Beck, D.G. Flad, C. Tonhuser, G. Gassner, C.-D. Munz*

**Large-Eddy Simulation of Turbulent Flow Around a Finite-Height Wall-Mounted Square Cylinder Within a Thin Boundary Layer**

*M. Saeedi, B.-C. Wang*

**Application of the Lattice-Boltzmann Method for Particle-laden Flows: Point-particles and Fully Resolved Particles**

*M. Dietzel, M. Ernst, M. Sommerfeld*

**Numerical Simulation of Two Phase Turbulent Flow of Nanofluids in Confined Slot Impinging Jet**

*B. Yousefi-Lafouraki, A. Ramiar, A.A. Ranjbar*

**Investigation of Particle Deposition Characteristics in Vicinity of Laidback Fan-shaped Film Cooling Holes**

*C. Wang, J. Zhang, J. Zhou*

**Effects of Spray and Turbulence Modelling on the Mixing and Combustion Characteristics of an *n*-heptane Spray Flame Simulated with Dynamic Adaptive Chemistry**

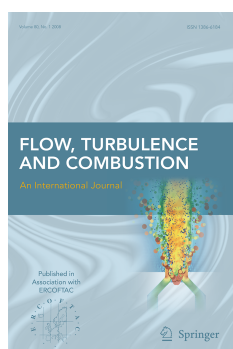
*Z. Lu, L. Zhou, Z. Ren, T. Lu, C.K. Law*

**A Two-Dimensional Tabulated Flamelet Combustion Model for Furnace Applications**

*O. Colin, J.-B. Michel*

**Generation of Adverse Pressure Gradient in the Circumferential Flashback of a Premixed Flame**

*N. Karimi, S. McGrath, P. Brown, J. Weinkauff, A. Dreizler*



RECENT TABLE OF CONTENTS OF FLOW TURBULENCE AND COMBUSTION

AN INTERNATIONAL JOURNAL PUBLISHED BY SPRINGER

IN ASSOCIATION WITH ERCOFTAC

EDITOR-IN-CHIEF: M. A. LESCHZINER

EDITORS: A. DREIZLER, K. FUKAGATA, E. GUTMARK, K. HANJALIC, A. M. KEMPE, S.

MENON, M. REEKS, W. RODI

FOUNDING EDITOR: F. NIEUWSTADT

**VOLUME 97, NUMBER 3, OCTOBER 2016**

**Point-Particle DNS and LES of Particle-Laden Turbulent flow - a state-of-the-art review**

*J.G.M. Kuerten*

**Study of the Turbulent Velocity Field in the Near Wake of a Bluff Body**

*J.J. Cruz Villanueva, L.F. Figueira da Silva*

**Effects of Synthetic jets on a D-Shaped Cylinder wake at a Subcritical Reynolds Number**

*N. Gao, Y.Q. Li, H.L. Bai, C.J. Wu*

**Hydrodynamics During the Transient Evolution of Open Jet Flows from/to Wall Attached Jets**

*A. Valera-Medina, H. Baej*

**A Bayesian Calibration/Prediction Method for Reducing Model-Form Uncertainties with Application in RANS Simulations**

*J.-L. Wu, J.-X. Wang, H. Xiao*

**Kovaszny Mode Decomposition of Velocity-Temperature Correlation in Canonical Shock-Turbulence Interaction**

*R. Quadros, K. Sinha, J. Larsson*

**On Large-Scale Friction Control in Turbulent Wall Flow in Low Reynolds Number Channels**

*J. Canton, R. Örlü, C. Chin, N. Hutchins, J. Monty, P. Schlatter*

**Wind Impact on Single Vortices and Counterrotating Vortex Pairs in Ground Proximity**

*F. Holzäpfel, N. Tchipev, A. Stephan*

**Numerical Simulation of Diesel Particulate Filter Regeneration Considering Ash Deposit**

*T. Chen, Z. Wu, J. Gong, J.-q. E*

**Experimental and Numerical Investigation of Effects of Charge Density on the Bubble Characteristics Originating from the Combustion of Pyrotechnic Mixtures**

*D.-h. Ouyang, Q.-t. Zhang, F. Wang*

**Damköhler-Shelkin Paradox in the Theory of Turbulent Flame Propagation, and a Concept of the Premixed Flame at the Intermediate Asymptotic Stage**

*V.L. Zimont*

**One-Dimensional Modeling of Turbulent Premixed Jet Flames - Comparison to DNS**

*N. Punati, H. Wang, E.R. Hawkes, J.C. Sutherland*

**Influence of Co-flow on Flickering Diffusion Flame**

*N. Fujisawa, Y. Matsumoto, T. Yamagata*

**DNS Analysis of Wall Heat Transfer and Combustion Regimes in a Turbulent Non-premixed Wall-jet Flame**

*Z. Pouransari, L. Vervisch, L. Fuchs, A.V. Johansson*

---

## ERCOFTAC Special Interest Groups

---

### 1. Large Eddy Simulation

Salveti, M.V.  
University of Pisa, Italy.  
Tel: +39 050 221 7262  
Fax: +39 050 221 7244  
mv.salveti@ing.unipi.it

### 4. Turbulence in Compressible Flows

Dussauge, Jean-Paul  
IUSTI, Marseille  
jean-paul.dussauge  
@polytech.univmrs.fr

### 5. Environmental Fluid Mechanics

Armenio, V.  
Universit di Trieste, Italy.  
Tel: +39 040 558 3472  
Fax: +39 040 572 082  
armenio@dica.units.it

### 10. Transition Modelling

Dick, E.,  
University of Ghent, Belgium.  
Tel: +32 926 433 01  
Fax: +32 926 435 86  
erik.dick@ugent.be

### 12. Dispersed Turbulent Two Phase Flows

Sommerfeld, M.  
Martin-Luther University, Germany.  
Tel: +49 346 146 2879  
Fax: +49 346 146 2878  
martin.sommerfeld@iw.uni-halle.de

### 14. Stably Stratified and Rotating Flows

Redondo, J.M.  
UPC, Spain.  
Tel: +34 934 017 984  
Fax: +34 934 016 090  
redondo@fa.upc.edu

### 15. Turbulence Modelling

Jakirlic, S.  
Darmstadt University of Technology,  
Germany.  
Tel: +49 615 116 3554  
Fax: +49 615 116 4754  
s.jakirlic@sla.tu-darmstadt.de

### 20. Drag Reduction and Flow Control

Choi, K-S.  
University of Nottingham, England.  
Tel: +44 115 951 3792  
Fax: +44 115 951 3800  
kwing-so.choi@nottingham.ac.uk

### 48. Aerosol Engineering

Geurts, B.  
University of Twente  
Tel: +31 53 489 4125  
b.j.geurts@utwente.nl

### 24. Variable Density Turbulent Flows

Anselmet, F.  
IMST, France.  
Tel: +33 491 505 439  
Fax: +33 491 081 637  
anselmet@irphe.univ-mrs.fr

### 28. Reactive Flows

Roekaerts, D.  
Delft University of Technology,  
The Netherlands.  
Tel: +31 152 782 470  
D.J.E.M.Roekaerts@tudelft.nl

### 32. Particle Image Velocimetry

Stanislas, M.  
Ecole Centrale de Lille, France.  
Tel: +33 320 337 170  
Fax: +33 320 337 169  
Michel.Stanislas@ec-lille.fr

### 33. Transition Mechanisms, Prediction and Control

Hanifi, A.  
FOI, Sweden.  
Tel: +46 855 503 197  
Fax: +46 855 503 397  
ardeshir.hanifi@foi.se

### 34. Design Optimisation

Giannakoglou, K.  
NTUA, Greece.  
Tel: +30 210 772 1636  
Fax: +30 210 772 3789  
kgianna@central.ntua.gr

### 35. Multipoint Turbulence Structure and Modelling

Cambon, C.  
ECL Ecully, France.  
Tel: +33 472 186 161  
Fax: +33 478 647 145  
claudc.cambon@ec-lyon.fr

### 36. Swirling Flows

Braza, M.  
IMFT, France.  
Tel: +33 534 322 839  
Fax: +33 534 322 992  
braza@imft.fr

### 37. Bio-Fluid Mechanics

Poelma, C.  
Delft University of Technology, Holland.  
Tel: +31 152 782 620  
Fax: +31 152 782 947  
c.poelma@tudelft.nl

### 49. 3D Wakes

Morrison, J.F.  
Imperial College, London  
Tel: +44 (0)20 7594 5067

### 38. Micro-thermofluidics

Seoud, R.E (interim)  
ERCOFTAC  
Tel: +44 203 602 8984  
richard.seoud-ieo@ercoftac.org

### 39. Aeroacoustics

Bailly, C.  
Ecole Centrale de Lyon, France.  
Tel: +33 472 186 014  
Fax: +33 472 189 143  
christophe.bailly@ec-lyon.fr

### 40. Smoothed Particle Hydrodynamics

Le Touze, D.  
Ecole Centrale de Nantes, France  
Tel: +33 240 371 512  
Fax: +33 240 372 523  
David.LeTouze@ec-nantes.fr

### 41. Fluid Structure Interaction

Longatte, E.  
EDF, France.  
Tel: +33 130 878 087  
Fax: +33 130 877 727  
elisabeth.longatte@edf.fr

### 42. Synthetic Models in Turbulence

Nicolleau, F.  
University of Sheffield, England.  
Tel: +44 114 222 7867  
Fax: +44 114 222 7890  
f.nicolleau@sheffield.ac.uk

### 43. Fibre Suspension Flows

Lundell, F.  
The Royal Institute of Technology,  
Sweden.  
Tel: +46 87 906 875  
fredrik@mech.kth.se

### 44. Fundamentals and Applications of Fractal Turbulence

Fortune, V.  
Université Pierre et Marie Curie, France.  
Tel: +33 549 454 044  
Fax: +33 549 453 663  
veronique.fortune@lea.univ-poitiers.fr

### 45. Uncertainty Quantification in Industrial Analysis and Design

Lucor, D.  
d'Alembert Institute, France.  
Tel: +33 (0) 144 275 472  
didier.lucor@upmc.fr

## ERCOFTAC Pilot Centres

### Alpe - Danube - Adria

*Steiner, H.*  
Inst. Strömungslehre and  
Wärmeübertragung  
TU Graz, Austria  
kristof@ara.bme.hu

### France West

*Danaila, L.*  
CORIA, University of Rouen,  
Avenue de l'Université BP12,  
76801 Saint Etienne du Rouvray  
France.  
Tel: +33 232 953 702  
luminita.danaila@coria.fr

### Netherlands

*Van Heijst, G.J.*  
J.M. Burgerscentrum,  
National Research School for Fluid  
Mechanics, Mekelweg 2,  
NL-2628 CD Delft, Netherlands.  
Tel: +31 15 278 1176  
Fax: +31 15 278 2979  
g.j.f.vanheijst@tudelft.nl

### Belgium

*Geuzaine, P.*  
Cenaero,  
CFD Multi-physics Group,  
Rue des Frères Wright 29,  
B-6041 Gosselies,  
Belgium.  
Tel: +32 71 919 334  
philippe.geuzaine@cenaero.be

### Germany North

*Sommerfeld, M.*  
Martin-Luther University  
Germany  
Tel: +49 346 146 2879  
Fax: +49 346 146 2878  
martin.sommerfeld@iw.uni-halle.de

### Nordic

*Wallin, S.*  
Swedish Defence Research Agency FOI,  
Information and Aeronautical Systems,  
S-16490 Stockholm,  
Sweden.  
Tel: +46 8 5550 3184  
Fax: +46 8 5550 3062  
stefan.wallin@foi.se

### Brasil

*Rodriguez, O.*  
Department of Mechanical Engineering,  
Sao Carlos School of Mechanical  
Engineering,  
Universidade de Sao Paulo,  
Brasil.  
oscarmhr@sc.usp.br

### Germany South

*Becker, S.*  
Universität Erlangen, IPAT  
Cauerstr. 4  
91058 Erlangen  
Germany  
Tel: +49 9131 85 29451  
Fax: +49 9131 85 29449  
sb@ipat.uni-erlangen.de

### Poland

*Rokicki, J.*  
Warsaw University of Technology,  
Inst. of Aero. & App. Mechanics,  
ul. Nowowiejska 24,  
PL-00665 Warsaw, Poland.  
Tel: +48 22 234 7444  
Fax: +48 22 622 0901  
jack@meil.pw.edu.pl

### Czech Republic

*Bodnar, T.*  
Institute of Thermomechanics AS CR,  
5 Dolejskova,  
CZ-18200 Praha 8,  
Czech Republic.  
Tel: +420 224 357 548  
Fax: +420 224 920 677  
bodnar@marian.fsik.cvut.cz

### Greece

*M. Founti.*  
National Tech. University Of Athens,  
School of Mechanical Engineering,  
Lab. of Steam Boilers and  
Thermal Plants,  
Heron Polytechniou 9,  
15780 Zografou, Athens, Greece  
Tel: +30 210 772 3605  
Fax: +30 210 772 3663  
mfou@central.ntua.gr

### France - Henri Bénard

*Godefert, F.S.*  
Ecole Centrale de Lyon.  
Fluid Mechanics and Acoustics Lab.,  
F-69134 Ecully Cedex,  
France.  
Tel: +33 4 72 18 6155  
Fax: +33 4 78 64 7145  
fabien.godefert@ec-lyon.fr

### Spain

*Onate, E.*  
Universitat Politècnica de Catalunya,  
*Theofilis, V.*  
Universidad Politécnica de Madrid, Spain  
Spain.  
onate@cimne.upc.edu  
vassilis@aero.upm.es

### Switzerland

*Gallaire, F.*  
EPFL-STI-LTCM  
Station 9,  
CH-1015 Lausanne,  
Switzerland.  
francois.gallaire@epfl.ch

### Portugal

*da Silva, C. B.*  
Instituto Superior Técnico,  
University of Lisbon  
Av. Rovisco Pais, 1049-001 Lisboa  
Portugal  
carlos.silva@ist.utl.pt

### France South

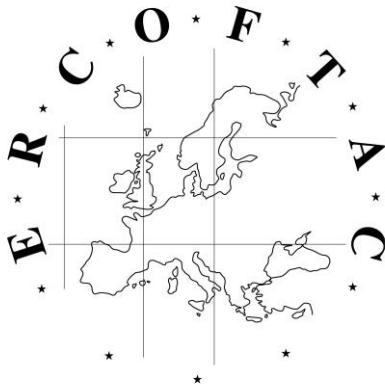
*Braza, M.*  
IMF Toulouse,  
CNRS UMR - 5502,  
Allée du Prof. Camille Soula 1,  
F-31400 Toulouse Cedex, France.  
Tel: +33 534 322 839  
Fax: +33 534 322 992  
Braza@imft.fr

### Italy

*Rispoli, F.*  
Tel: +39 064 458 5233  
franco.rispoli@uniroma1.it  
*Borello, D.*  
Tel: +39 064 458 5263  
domenico.borello@uniroma1.it  
Sapienza University of Rome,  
Via Eudossiana, 18  
00184 Roma, Italy

### United Kingdom

*Standingford, D.*  
Zenotech Ltd.  
University Gate East, Park Row,  
Bristol, BS1 5UB  
England.  
Tel: +44 117 302 8251  
Fax: +44 117 302 8007  
david.standingford@zenotech.com



# Best Practice Guidelines for Computational Fluid Dynamics of Dispersed Multi-Phase Flows

## Editors

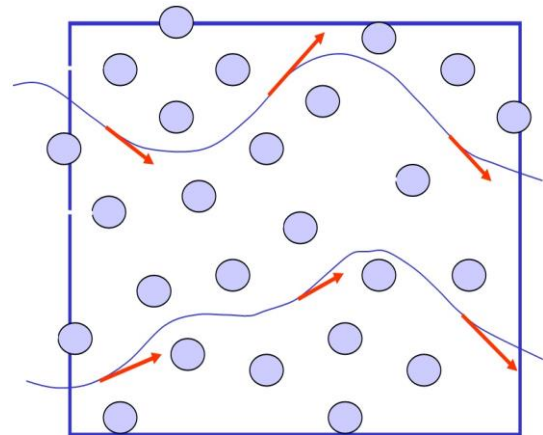
Martin Sommerfeld, Berend van Wachem  
&  
René Oliemans

The simultaneous presence of several different phases in external or internal flows such as gas, liquid and solid is found in daily life, environment and numerous industrial processes. These types of flows are termed multiphase flows, which may exist in different forms depending on the phase distribution. Examples are gas-liquid transportation, crude oil recovery, circulating fluidized beds, sediment transport in rivers, pollutant transport in the atmosphere, cloud formation, fuel injection in engines, bubble column reactors and spray driers for food processing, to name only a few. As a result of the interaction between the different phases such flows are rather complicated and very difficult to describe theoretically. For the design and optimisation of such multiphase systems a detailed understanding of the interfacial transport phenomena is essential. For single-phase flows Computational Fluid Dynamics (CFD) has already a long history and it is nowadays standard in the development of air-planes and cars using different commercially available CFD-tools.

Due to the complex physics involved in multiphase flow the application of CFD in this area is rather young. These guidelines give a survey of the different methods being used for the numerical calculation of turbulent dispersed multiphase flows. The Best Practice Guideline (BPG) on Computational Dispersed Multiphase Flows is a follow-up of the previous ERCOFTAC BPG for Industrial CFD and should be used in combination with it. The potential users are researchers and engineers involved in projects requiring CFD of (wall-bounded) turbulent dispersed multiphase flows with bubbles, drops or particles.

## Table of Contents

1. Introduction
2. Fundamentals
3. Forces acting on particles, droplets and bubbles
4. Computational multiphase fluid dynamics of dispersed flows
5. Specific phenomena and modelling approaches
6. Sources of errors
7. Industrial examples for multiphase flows
8. Checklist of 'Best Practice Advice'
9. Suggestions for future developments



Copies of the Best Practice Guidelines can be acquired electronically from the ERCOFTAC website:

[www.ercoftac.org](http://www.ercoftac.org)

Or from:

ERCOFTAC (CADO)  
PO Box 53877  
London, SE27 7BR  
United Kingdom

Tel: +44 203 602 8984

Email: [magdalena.jakubczak@ercoftac.org](mailto:magdalena.jakubczak@ercoftac.org)

The price per copy (not including postage) is:

ERCOFTAC members

First copy	Free
Subsequent copies	75 Euros
Students	75 Euros

Non-ERCOFTAC academics	140 Euros
Non-ERCOFTAC industrial	230 Euros
EU/Non EU postage fee	10/17 Euros